

Aus der Klinik für Strahlentherapie und Radioonkologie, Institut für Experimentelle
Strahlentherapie der Medizinischen Fakultät Mannheim
(Direktor: Prof. Dr. med. Frederik Wenz)

Modeling the SIGMA-Eye Applicator for Hyperthermia via Multiple
Infinitesimal Dipoles

Inauguraldissertation
zur Erlangung des Doctor scientiarum humanarum (Dr. sc. hum.)
der
Medizinischen Fakultät Mannheim
der Ruprecht-Karls-Universität
zu
Heidelberg

vorgelegt von
Wanji He

aus
Hubei, China
2018

Dekan: Prof. Dr. med. Sergij Goerd
Referent: Prof. Dr. rer. nat. Jürgen Hesser

INHALTSVERZEICHNIS

Seite

ABBREVIATIONS.....	1
1 INTRODUCTION	2
1.1 Hyperthermia Treatment.....	2
1.1.1 Hyperthermia Types	2
1.1.2 Hyperthermia Treatment Clinical Trials.....	3
1.1.3 Hyperthermia Treatment Systems	4
1.2 Hyperthermia Treatment Planning.....	5
1.3 State of the Art.....	7
1.3.1 Hyperthermia Planning Software Packages	7
1.3.2 Electromagnetic Simulation	8
1.4 Objectives of the Thesis	10
1.5 Thesis Outline.....	10
2 MATERIAL AND METHODS	11
2.1 Theory	11
2.1.1 Fundamentals of Electromagnetism	11
2.1.2 Numerical Method.....	12
2.1.3 Modified Infinitesimal Dipole Model	16
2.1.4 Applicators with Strong Mutual Coupling	18
2.1.5 A Complete Solution of the Applicator	19
2.1.6 Global Optimization Algorithm	19
2.2 Implementation	20
2.2.1 Development Setup	20
2.2.2 Applicator and Phantom Setup	20
2.2.3 COMSOL Multiphysics.....	22
2.2.4 Optimization Using OQNLP	22
2.2.5 SIGMA-Eye Applicator Modeling	23

3	RESULTS.....	25
3.1	Parameter Determination in Meep.....	25
3.1.1	PML Thickness Determination.....	25
3.1.2	Spatial Resolution Determination.....	26
3.2	Equivalent Dipole Models.....	26
3.2.1	Equivalent Dipole Models of the Blocks.....	26
3.2.2	Equivalent Dipole Models of the Single Isolated Antenna.....	27
3.3	Comparison with the Measurement.....	27
3.3.1	The IDM with Mutual Coupling.....	28
3.3.2	The IDM of the Single Isolated AUT.....	32
3.4	Frequency Analysis of the Basic-Building-Block-Based IDM.....	35
3.5	Permittivity-Dependence Analysis of the Basic-Building-Block-Based IDM.....	37
3.6	Conductivity-Dependence Analysis of the Basic-Building-Block-Based IDM.....	39
4	DISCUSSION.....	41
5	CONCLUSION.....	44
6	REFERENCES.....	45
7	TABLE AND FIGURE APPENDIX.....	51
8	CV.....	78
9	ACKNOWLEDGEMENT.....	79

ABBREVIATIONS

Radiofrequency (RF), Hyperthermia Treatment Planning (HTP), Electromagnetic simulation (EM simulation), Electromagnetic Hyperthermia Treatment Planning (EM-HTP), Infinitesimal Dipole Model (IDM), OQNLP (OptQuest Nonlinear Programming), Antenna under Test (AUT), Specific Absorption Rate (SAR), Perfectly Matched Layer (PML), FDTD (Finite Difference Time Domain), FDFD (Finite Difference Frequency Domain)

1 INTRODUCTION

1.1 Hyperthermia Treatment

Over the past several decades, cancer is still one of the leading causes of human deaths. According to the American Cancer Society annual report, in 2014, nearly 600 000 Americans were expected to die of cancer, more than 1500 persons per day.^[1] Chemotherapy, radiation therapy and surgery have been the three kinds of basic methods of cancer treatment. Hyperthermia treatment, which is mostly performed in clinic as an assistant therapy method combined with chemotherapy or radiation therapy, has been also playing a more and more important role in tumor therapy. It is a kind of cancer treatment in which the tumor tissue is exposed to elevated temperatures (approximately 45°C) thus to damage and kill tumor cells.^[2] It has been proven that high temperatures can damage and kill tumor cells with minimal injury to normal tissues. Thus in this sense hyperthermia therapy can help shrink tumors.^[3]

1.1.1 Hyperthermia Types

There are different types of hyperthermia treatments classified based on treatment regions and methods of heat generation.

Typical heat-generation methods include radiofrequency^[4], microwave^[5], laser^[6], and high-intensity focused ultrasound^[7]. Concerning the use of electromagnetic energy to cause heating of biological tissues, one of the fundamental aspects is the electromagnetic spectrum, as shown in Fig.1. For hyperthermia treatment, the relevant part is the nonionizing electromagnetic fields of which the photon energy, given by the product of the frequency and Planck's constant, is insufficient to cause ionization. Therefore, heating sources employed in electromagnetic hyperthermia therapy relates to microwaves (MW) and radiofrequency (RF) fields. The term RF often refers to the range from 3 kHz to 300 GHz, and microwave ranges from 300 MHz and 300 GHz ^[8].

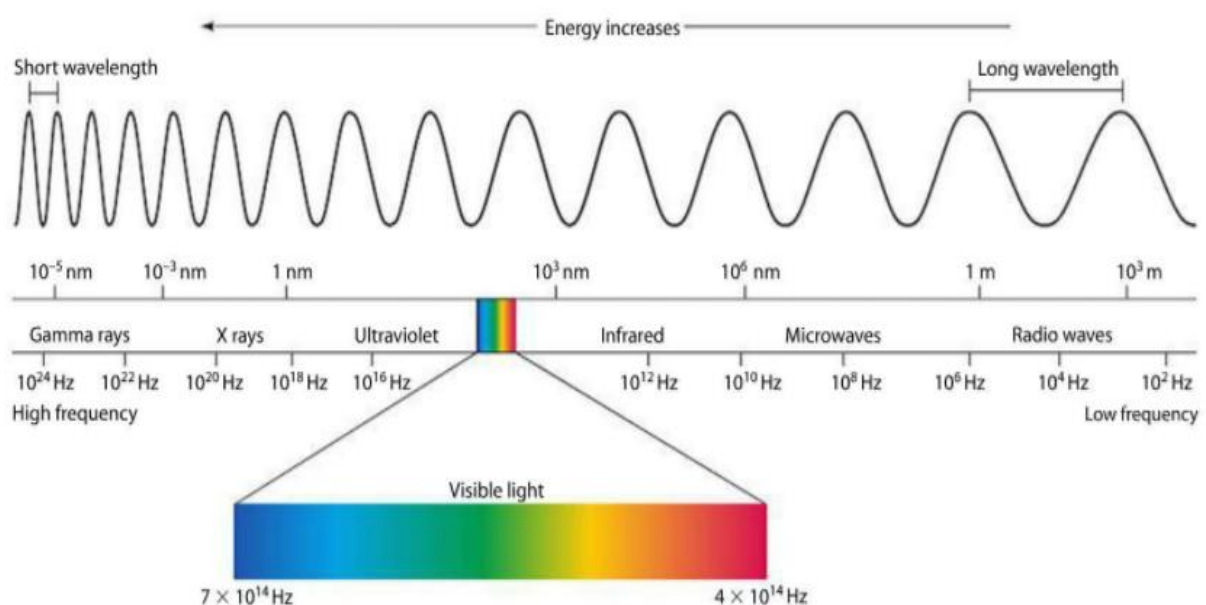


Fig.1: The electromagnetic spectrum

Depending on the target region, hyperthermia therapy is classified into interstitial and endo-cavitary hyperthermia, local hyperthermia, regional hyperthermia, and whole body hyperthermia^[9].

For interstitial and endocavitary hyperthermia, antennas or applicators are implanted within the tumor or inserted in natural openings of hollow organs such as the urethra, rectum, vagina, cervix, and esophagus. In most cases, such a hyperthermia treatment is combined with brachytherapy by afterloading methods in close connection to the target.

Local hyperthermia mainly aims at superficial tumors, and is implemented by means of antennas or applicators emitting mostly microwaves or radiofrequency waves placed on human surfaces with a contacting medium. There are several kinds of clinically used applicators, such as waveguide applicators, horn, spiral, current sheet, and compact applicators. Comparably, regional hyperthermia is aimed at deep-seated tumors, e.g. of the pelvis or abdomen.

Whole-body hyperthermia is performed in the form of a special bath, where a patient is under general anesthesia, and immersing his or her body and extremities in warmed water warmed up to 44.0 – 47.0°C except for the head. To be effective, a high level of body temperature of 43°C is necessary in whole body hyperthermia. It is still controversial whether whole body hyperthermia at 43.5-44°C is a dream or reality.^[10]

1.1.2 Hyperthermia Treatment Clinical Trials

In clinic, hyperthermia is predominantly used in combination with other forms of cancer therapies, such as radiation therapy and chemotherapy, and such a combination is the so-called multimodal treatment, such as thermoradiotherapy, thermochemotherapy.^[11] As demonstrated by many preclinical and clinical trials for advanced and intractable tumor types, hyperthermia can increase tumor sensitivity to chemotherapeutic drugs and to radiation.^[12, 13] Thus, thermal combination therapy can serve as an effective adjuvant to radiotherapy and chemotherapy.^[14]

Moreover, various multimodal treatment types provide multiple choices not only for local solid tumors such as colorectal cancer, prostate cancer, but also for advanced metastatic cancers such as melanomas and head and neck cancers. For a combination treatment, especially a tri-modality combination, the time interval between the two or three kinds of methods in the combination and operation sequence must be taken into account in order to achieve the most effective treatment efficiency. Generally speaking, thermal enhancement of radiation response and chemotherapeutic-drug response of tumor cells reaches the maximum when the radiation or chemotherapy and heating treatments are performed simultaneously. However, in clinical practice, it is difficult to achieve simultaneous implementation of the combined therapy. An effective solution to this problem is to shorten the interval between the two therapies of the combination. Whether hyperthermia is to be applied prior to or after radiotherapy and chemotherapy is still a controversial issue. Many studies support to perform the hyperthermia after radiation or chemotherapy.^[15] Besides the two factors of time interval and sequences, the dose-response relationship is also of great importance in combined treatment.^[16, 17]

No matter what kind of hyperthermia therapy or combination is going to be used, temperature monitoring during treatment is indispensable for thermal therapy. In addition, the tissue physical parameter, perfusion, performs a very important role in heat transfer. It always counteracts the temperature rise. On the other side, increased perfusion in the tumor region leads to a higher drug delivery and re-

oxygenation, thus increasing the efficacy of radiotherapy.^[18] Therefore, an imaging tool which can characterize both temperature and perfusion of tissues in real time would be of great help for treatment monitoring. At present, magnetic resonance imaging (MRI) is the most widely used tool to measure both temperature and perfusion noninvasively and in real time.^[19, 20] Dynamic contrast enhanced MRI was also proved to be a good predictor of clinical outcome in canine spontaneous soft tissue sarcomas treated with thermoradiotherapy.^[21]

With the emerging of nanoparticle technology, the method magnetic nanoparticle hyperthermia has also been explored as a cancer therapy approach. It is based on the principle that magnetic nanoparticles introduced into a tumor produce heat when subjected to an alternating magnetic field.^[22] Various types of superparamagnetic and ferromagnetic particles, with different coatings and targeting agents, allow for tumor site and type specificity. Anyway, with the use of magnetic nanoparticle, hyperthermia is being developed to be a targeted tumor therapy.

1.1.3 Hyperthermia Treatment Systems

As mentioned before, hyperthermia is classified into whole body, regional, superficial and interstitial treatments. Various treatment systems have been designed and developed for specific treatment purposes.

1.1.3.1 Hyperthermia Treatment Systems for Deep-Seated Tumors

To delivery energy to deep-seated tumors from external non-invasive systems, electromagnetic fields in the range of 10-120MHz are generally used, which have long wavelengths compared to body dimensions and, thus, are capable of depositing energy over a sizeable region in deep depth.

In the early hyperthermia trials, single aperture devices which had no ability to steer or focus energy other than by shifting patient position relative to the applicator, were utilized, such as the 27MHz Ridged Waveguide^[23], 82MHz Helix^[24], the 70MHz Coaxial TEM applicator^[25-27] and so on.

In order to have more control over power deposition, phased array applicators have been developed. One of the first is the Annular Phased Array (APAS) system which uses a cylindered shaped plastic shell to support 8 radiating dipoles of the equal power and the equal phase, and works in 60-120MHz.^[28] However, these early annular phased array systems are limited in 3D adjustability and cannot localize heat within an entire tumor volume at deep depth.^[29-31]

Improvement of SAR adjustment was later achieved, such as, the SIGMA-60 applicator^[32] and the SIGMA-Ellipse applicator^[32], which support four independent phase and amplitude controls for each two-antenna channel. Compared to the SIGMA-60 applicator, the SIGMA-Ellipse applicator provides improved comfort for smaller size patients. The next generation of applicators, the SIGMA-Eye applicator was developed. The applicator operates at the same frequencies as the predecessor SIGMA-60 applicator, but include three rings of eight dipoles each and 12 independent phase and amplitude adjustments to shape and steer power deposition peaks axially and radially around the body interior to achieve 3D conformal treatments. Both the SIGMA-60 applicator and the SIGMA-Eye applicator are still used in clinic currently.

1.1.3.2 Hyperthermia Treatment Systems for Superficial Tumors

In general, higher frequency EM techniques are used to treat superficial tumors less than 2 cm to the surface. Similar to the development of applicators of hyperthermia for deep-seated tumors, the treatment systems of superficial hyperthermia has also gone through the development process from the single microwave waveguide antenna^[33-35], to custom-sized arrays, e.g. 433 MHz Current Sheet Applicators^[36], Lucite Cone Applicators (LCA)^[37], to the Conformal Microwave Array (CMA) applicator^[38].

1.1.3.3 Hyperthermia Treatment Systems for Interstitial Treatments

Speaking of interstitial and intracavitary heating technology, there are at least nine distinct technologies for applying energy from miniature implantable heat sources and countless implementations of that technology in both university prototypes and commercial forms.^[39] In order to achieve sufficient uniformity, interstitially implanted sources are placed in arrays with <1–2 cm spacing. Thus, there has been considerable use of hot source techniques like needle- or catheter-based Hot Water Perfusion (HWP)^[40], DC Resistance Wires (RW)^[41] and so on.

Real-time adjustment of SAR along the implant length is also possible.^[42] One of the most adjustable patterns of the current interstitial systems is the MECS electrodes^[43].

All in all, over the past 30 years, hyperthermia treatment systems have progressed from single source applicators to multiple source approaches, and from mono-phase and mono-amplitude controls to multi-element phase and amplitude adjustable arrays. The development provides possibilities for more sophisticated and accurate treatment styles and better 3D conformity of target regions.

1.2 Hyperthermia Treatment Planning

Driven by the developments of computing power and computational techniques, personalized hyperthermia treatment planning (HTP) is becoming possible and essential for clinical practice, aimed at achieving maximum treatment effects for tumor targets and minimal side effects for the surrounding tissues simultaneously.

In the context of hyperthermia therapy driven by phased-antenna-array applicators, personalized treatment planning is to acquire optimal parameters of the applicator, e.g. amplitude and phase of each antenna, which maximize treatment efficacy and avoid hotspots, before treatment. It is of great importance for various reasons. Firstly, the commonly used phased-array applicators often give rise to a complex energy deposition pattern which is not easily controlled. Therefore pre-treatment planning shows great importance to predict and optimize energy deposition patterns. In addition, the use of HTP is very influential in the evaluation and development of new EM applicators^[44]. Moreover, HTP has been used to study the impact of various physical and physiological parameters in hyperthermia treatment.

Unfortunately, pre-treatment planning often cannot avoid treatment-limiting hotspots completely. Therefore, electromagnetic hyperthermia treatment planning (EM-HTP) is beginning to be used in applications like preplanning-assisted real-time treatment guidance. The idea is to convert information such as real-time non-invasive temperatures into adjusted settings based on HTP optimization during the treatment process. Besides, subjective information, such as complaints from the patient, has been taken as a feedback for real-time adjustment of pre-planning settings.^[44, 45]

A scheme of HTP is shown in Fig.2^[46].

- i) Patient image acquiring. As shown in Fig.2, at present the image data is mostly acquired using Computer Tomography (CT) or Magnetic Resonance Imaging (MRI).
- ii) Image segmentation. Image segmentation is to distinguish different tissues, thus to assign physical parameters to tissues.
- iii) Treatment modeling. This step is to import the patient geometrical data and the applicator data into computer, thus to create the 3D model of the treatment environment, including a virtual patient, and a virtual applicator, as shown in Fig.3 (b).
- iv) Electromagnetic simulation. In regional electromagnetic hyperthermia, two different physical processes need to be considered, electromagnetic field propagation and heating transfer. The first one is theoretically described by Maxwell's Equations, which is a series of partial differential equations, and quantitatively describes the relationship between electromagnetic fields and electric properties of the mediums and energy sources. Therefore, using the patient model and the applicator model created in the last step, electromagnetic fields are acquired by solving Maxwell's Equation. Based on the electromagnetic field, the corresponding power absorption pattern, also called Specific Absorption Rate (SAR) is calculated.
- v) Thermal Simulation. Based on SAR distribution, the second physical process, heat transfer is modeled to calculate temperature distribution in human body. Because of individualities and uncertainties of the thermal properties of tissues, which vary between patients, within the patient and over time, it is challenging to accurately modeling the time-dependent temperature distribution. The most commonly used method to model heat transfer in living tissues is the PBHE^[47], which models the impact of perfusion as an isotropic heat sink.
- vi) Optimization. The optimization process is to adjust the applicator setting, thus to focus the temperature rise on tumors to achieve better treatment efficacy. In principle, the optimization could be based on SAR field or temperature distribution. However, from the therapeutic point of view the power absorption is less important than the resulting temperature increase. Thus, in clinic, mostly temperature distribution is used as the import of optimization.

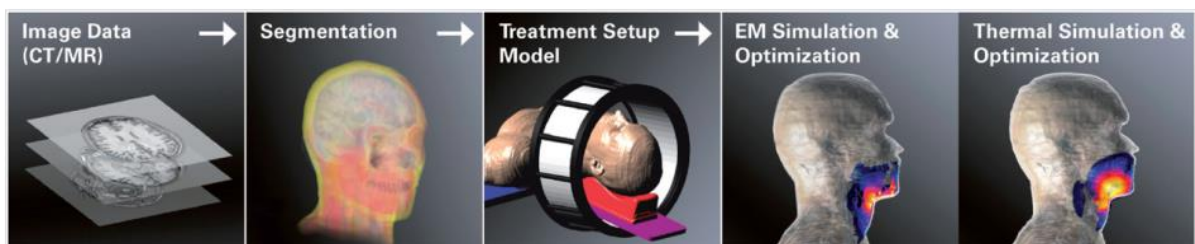


Fig.2: Schematic workflow for EM-HTP, using head and neck

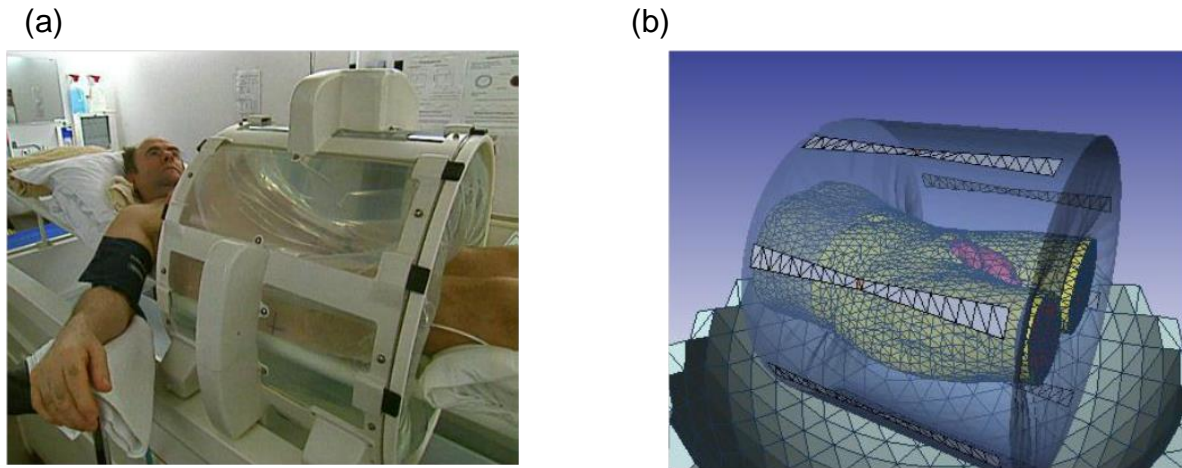


Fig.3: Hyperthermia treatment planning. (a) real patient in hospital; (b) virtual patient in the lab

1.3 State of the Art

1.3.1 Hyperthermia Planning Software Packages

At present, most of the existing codes for HTP have been developed and used for research purposes. They are usually developed for the variant of hyperthermia used at the specific institute and specific treatment site, and are difficult to be generalized.

The most widely used commercial HTP software system is SigmaHyperPlan^[48]. It was developed by the Zuse Institute Berlin (ZIB) in cooperation with the Charite Berlin, Campus Virchow-Klinikum for performing 3D-simulations and treatment planning in regional hyperthermia, mostly in pelvis and abdomen regions. It is built on top of the modular, object-oriented visualization system AMIRA, which already contains powerful algorithms for image processing, geometric modeling and 3D graphics display. Based on AMIRA, SigmaHyperPlan provides a complete HTP module chain, including segmentation of medical image data, generating a patient model, electric field simulation, temperature simulation and temperature optimization. Also, SigmaHyperPlan is specified for the BSD RF wave applicators, SIGMA-60, SIGMA-Eye and SIGMA-2000.

Another commercial HTP package was developed based on SEMCAD X for superficial hyperthermia treatment^[49] and for deep hyperthermia treatment^[50]. SEMCAD X is a software tool originally designed for high-resolution EM simulations. Combined with the segmentation tool iSEG, multiple thermal solvers (PBHE, keff, DIVA), and several SAR and temperature optimization approaches as well as post-processing routines for dose and effect quantification, SEMCAD X has been elevated to a flexible HTP framework.

Recently, the software ALBA HTPS^[51] is being developed for superficial and deep hyperthermia treatment planning. It is consisted of three main modules, ALBA 3Dseg, ALBA 3Dvox and ALBA 3DSAR T.

Besides, although not integrated HTP platforms, some engineering simulation tools, e.g. COMSOL Multiphysics^[52] and HFSS^[53] provide most of the necessary functionality for the HTP, like electromagnetic simulation, thermal simulation. When combined with separate programs for tissue segmentation, those tools can be developed into complete HTP packages.

1.3.2 Electromagnetic Simulation

As mentioned before, electromagnetic simulation as heating source is an essential step of HTP to simulate the interaction between electromagnetic fields radiated by EM sources and physical objects. Of great importance are (1) the accuracy of the numerical modeling of the physical objects, (2) the numerical modeling of the EM sources and (3) electromagnetic field analysis.

1.3.2.1 Modeling of Physical Objects

In theory, there are two aspects about creating an accurate numerical model of the physical objects which are related to the EM propagation. Firstly it is necessary to create a computational grid model of the physical objects (including the patient and the treatment device) for computational modeling. With current medical imaging modalities, geometries of patients and treatment devices are relatively easy to be obtained. Based on anatomical images, computational grids need to be generated for computational modeling applications. Computational grids are generally classified into two categories, structured grids and unstructured grids.^[54] Structured grids have better convergence and higher resolution over unstructured grids. Unstructured grids are generally more flexible to adapt to different scales of physical objects, but require more computational memory and cost. However, in practice, uncertainties of grid models are unavoidable, e.g. the shape of water bolus between treatment fractions is changing. The other aspect is to assign electric properties, which are involved in Maxwell's Equations, such as permittivity and electrical conductivity, to the computational grid model. The currently used electric properties in clinical practice are mostly average values of healthy population. Such assumptions will cause uncertainties because of biological variation and individualities of patients, especially by diseases.^[55] Therefore, in order to create accurate patient models, obtaining patient-specific tissue properties may be as important as obtaining anatomical geometries. In addition, like any other scientific research, electromagnetic simulation is also a step-by-step process. It is better to validate the simulation firstly in homogeneous phantoms before proceeding to complex heterogeneous tissue anatomies. Thus, the accuracy and stability of the patient phantom is also of great importance.

1.3.2.2 Modeling of EM Sources

The second challenge to perform EM simulations is the modeling of EM sources. In general, approaches of creating models of EM sources are divided into two classes. One is the so-called full-wave analysis, which creates a geometrical model of the EM source combined with proper boundary conditions, and then use numerical algorithms to solve Maxwell's Equations^[56]. For example in^[56], the bow-tie antenna was modeled with two flat, quasi-conical copper strips, and the metallic boundary conditions were enforced on the grid points representing the antenna surfaces. And then FDTD and FEM were used for electric field computation. This full-wave analysis has the advantages of high-accuracy, completeness taking into account the effects of surface waves, space wave radiation, and external coupling, and versatility for arbitrary source geometries and environment. However, the computational cost is high. The other class refers to source models that introduce one or more significant but reasonable approximations to simplify the problem. The cavity model which was reported in 1978^[57] uses a magnetic wall boundary condition approximation for the periphery of the patch of microstrip antennas. The approach of the transmission line

model^[58] models thin wire configurations as a transmission line section with lumped loads. In^[59] a planar leaky-wave antenna (LWA) was represented by a transverse equivalent network where the guiding surface of the antenna was characterized as a scalar transfer impedance such that the structure is represented by its transverse equivalent network in the spectral domain. Another approach is to create a virtual model of the source, e.g. the Infinitesimal Dipole Model (IDM)^[60]. The idea of the IDM is to replace the antenna with a series of infinitesimal dipoles which radiates the same field as the antenna does. T.S. Sijher et al. proved the applicability of the IDM to simulate different kinds of antennas, like dipole, loop, waveguide, and dielectric resonator antenna. Shaya Karimkashi et al. presented their work of using the IDM to design compact antenna arrays preserving the maximum channel capacity of multi-input-multi-output systems in 2011.^[61] In^[62] the IDM was used to analyze focusing properties of time-domain ultra-wide band focusing array antennas.

Moreover, since antenna arrays have been broadly used as EM sources, it is essential to take mutual coupling between antenna elements into account. Various methods have been developed to approximate mutual coupling effects. For example, one of the well-known methods of mutual coupling calculation is to use the reaction theorem to develop a closed expression for coupling effects.^[60, 61, 63, 64] Another method of induced electromotive force is based on the estimation of the current distribution along the wire dipole or the effective current in the radiating aperture and then to find the electric field generated by an adjacent antenna element. It has a long history starting from the first formulation^[65, 66] to the modern theory of the mutual coupling compensation in antenna arrays^[67-69]. In^[70] a concept of 'basic building block' to contain mutual coupling effects in the IDM was proposed. Orest G.Vendik et al. proposed an algorithm based on the calculation of real and imaginary parts of the antenna mutual impedance using the Kramers-Kronig relations.^[71]

1.3.2.3 Electromagnetic Field Analysis

Based on the numerical models of EM sources and physical objects, there exist a number of numerical algorithms for the analysis of electromagnetic fields. Over the last three decades, various algorithms for solving partial differential equations have been developed for biomedical applications. In^[72], the method of the Weak Form of the Conjugate Gradient FFT was applied to the numerical simulation of the AMC-4 waveguide phased array. Samaras et al. verified the ability of FDTD to predict SAR distributions for the conventional waveguide applicator, the Lucite applicator and the Lucite cone applicator.^[73] Jacobsen et al. investigated FDTD for the simulation of microstrip muscle-loaded single-arm Archimedean spiral antennas.^[74] Wu et al. compared electric field (E-field) measurements with FEM predictions for a phased array designed for hyperthermia treatments in the intact breast.^[75] Gellermann et al. compared FDTD calculations with 3D SAR patterns derived from MR-thermographic measurements.^[76] B. Vrbová et al. implemented the simulation of the matrix of stripline applicators using the FDTD method.^[77] In 2014, a compact microwave patch applicator was designed and developed using the EM simulation software, Ansys HFSS.^[78]

Moreover, there exist many publically available EM simulation libraries, such as the open-source software NEC^[79], and the commercial software Ansys HFSS^[53], which are used for new applicator simulation and design. For example, in 2014, a compact microwave patch applicator was designed and developed using Ansys HFSS.^[78]

1.4 Objectives of the Thesis

Generally, this thesis is aimed at performing the electromagnetic simulation of EM-HTP for regional hyperthermia energized by the SIGMA-Eye applicator. The research has been concentrated on the following issues.

- i) The applicability of the conventional IDM combined with the global optimization algorithm OQNLP (OptQuest Nonlinear Programming) for a single isolated antenna of the applicator was explored.
- ii) To decrease the computational cost of the conventional IDM, the modified IDM, in which number and position of dipoles were predefined, was proposed and developed.
- iii) Since the SIGMA-Eye applicator consists of multiple antennas, the mutual coupling between antennas was taken into consideration by the basic-building-block-based IDM.
- iv) The frequency dependence of the block-based modified IDM was analyzed to lay the foundation for the future work on the wideband applicator.
- v) The permittivity and conductivity dependence of the block-based IDM were analyzed to explore the adaptability of the approach to the changing of the environment.

1.5 Thesis Outline

The thesis is basically composed of the three sections, theory, implementation, and experiments and results.

i) Theory.

This section starts with the related electromagnetic fundamentals, including Maxwell's Equations and Specific Absorption Rates. Then, the numerical algorithm used to solve Maxwell's Equations, Finite Difference Time Domain (FDTD) is introduced, and also some implementation details, e.g. resolution and boundary conditions. The third part of the theory section is dedicated to the IDM, including the conventional IDM theory, the modified IDM, mutual coupling calculation, and the global optimization algorithm OQNLP.

ii) Implementation.

This section gives a detailed description of the implementation of the electromagnetic simulation of the SIGMA-Eye applicator, including applicator and phantom setup, reference electric field data generated by COMSOL, and the applicator modeling using the block-based modified IDM.

iii) Experiments and Results.

In order to guarantee the convergence of the numerical simulation with Meep, the PML thickness and the spatial resolution used in Meep were explored to determine a proper value for the simulation in this work. Then, this section shows the applicability of the blocked-based modified IDM for the simulation of the Sigma-Eye applicator through comparison between the simulated electric field by the block-based modified IDM and the measurement data. Moreover, the experiments exploring the frequency dependence, permittivity and conductivity dependence of the block-based modified IDM are displayed.

2 MATERIAL AND METHODS

2.1 Theory

2.1.1 Fundamentals of Electromagnetism

2.1.1.1 Maxwell's Equations

Maxwell's Equations are a set of equations which describes how electric and magnetic fields are generated by charges, currents and changes of each other.^[8] In another way, that is to say that Maxwell's Equations describes the propagation of electric field and magnetic field in different mediums analytically. There are two forms of Maxwell's Equations: the integral form and the differential form. Here is the differential form.

$$\nabla \times \mathbf{E} = - \frac{\partial \mathbf{B}}{\partial t} \quad (2.1-1)$$

$$\nabla \times \mathbf{H} = \mathbf{J} + \frac{\partial \mathbf{D}}{\partial t} \quad (2.1-2)$$

$$\nabla \cdot \mathbf{B} = 0 \quad (2.1-3)$$

$$\nabla \cdot \mathbf{D} = \rho_v \quad (2.1-4)$$

where \mathbf{E} is the electric field (V/m), \mathbf{H} the magnetic field (A/m), \mathbf{D} the electric displacement field (C/m^2), \mathbf{B} the magnetic flux density (T), \mathbf{J} the electric current density vector (A/m^2), ρ_v the free electric charge density, and t the time variable (s). Besides, $\nabla \times$ is the curl operator, and $\nabla \cdot$ the divergence operator.

The constitutive relations establish the physical properties of materials since they associate field vectors, which are the electric field \mathbf{E} and magnetic field \mathbf{H} , with the electric displacement field \mathbf{D} , magnetic flux density \mathbf{B} and electric current density vector \mathbf{J} .

For the magnetic field,

$$\mathbf{B} = \mu \mathbf{H},$$

where μ is the magnetic permeability of the medium measured in the International System as (H/m). In the vacuum the value of magnetic permeability is $\mu_0 = 4\pi \times 10^{-7} H/m$. This is a very low magnetic permeability, which shows a difficulty in establishing a magnetic field in the vacuum. Usually the magnetic permeability of a medium is expressed as the relative permeability μ_r , which is the ratio between the permeability of the medium and the permeability of the vacuum.

Similarly, the relation between the electric field and the electric displacement field is expressed as

$$\mathbf{D} = \varepsilon \mathbf{E},$$

where ε is the electric permittivity of the medium measured in F/m. In the vacuum the electric permittivity value is $\varepsilon_0 = 8.854 \times 10^{-12} F/m$.

Likewise, the relative electric permittivity of the medium is defined by the relation

$$\varepsilon_r = \varepsilon / \varepsilon_0.$$

Finally, the constitutive relation relating the current density vector \mathbf{J} with the electric field vector \mathbf{E} is given by

$$\mathbf{J} = \sigma \mathbf{E},$$

where σ is the conductivity of the medium measured in S/m.

The first equation of Maxwell's Equations is called Faraday's Law. It shows that a changing magnetic field within a loop gives rise to an induced current, which is due to a force or voltage within that circuit. In another way, a magnetic changing in time gives rise to an electric field circulating around it. Likewise, the second equation, Ampere's Law, expresses that a flowing electric current leads to a magnetic field that circles the current, and also a time-changing electric flux density gives rise to a magnetic field that circles the \mathbf{D} field.

The third equation, Gauss's Law for Magnetism, highlights that magnetic charge doesn't exist, so that the divergence of \mathbf{B} and \mathbf{H} Fields is always zero through any volume. Comparably, the fourth equation, Gauss's Law means that the divergence of the \mathbf{D} field over any volume of space is exactly equal to the net amount of charge in the volume, which is to say that \mathbf{D} and \mathbf{E} field lines start and end on electric charges.

These equations describe any electromagnetic phenomenon and in their essence, summarize the spatial relations between both electrical and magnetic fields. Over the last several decades, the investment of electromagnetic scientific research has been largely devoted into developing mathematical techniques for the solution of Maxwell's Equations to solve practical problems.

2.1.1.2 Specific Absorption Rates

Specific Absorption Rate (SAR) is a measure of the rate at which electromagnetic energy is absorbed by human tissues when exposed to a RF electromagnetic field. The mathematical definition is the time derivative of the incremental energy (dW) absorbed by or dissipated in an incremental mass (dm) contained in a volume (dV) element of a medium of density (ρ).^[8] The unit is W/kg

$$SAR = \frac{d}{dt} \left(\frac{dW}{dm} \right) = \frac{d}{dt} \left(\frac{dW}{\rho dV} \right)$$

For steady-state sinusoidal fields, the local SAR at a given location is

$$SAR_{local} = \frac{\sigma |\mathbf{E}_0|^2}{2\rho}$$

where σ is the electric conductivity of the local tissue, and \mathbf{E}_0 is the amplitude of the electric field.

In the sense of EM-HTP, SAR is the output of the step of the EM simulation, and the input of heat transfer simulation.

2.1.2 Numerical Method

As described before, Maxwell's Equations is a set of partial differential equations. Various numerical algorithms have been developed to solve partial differential equations, e.g. Finite Element Method (FEM)^[80], Finite Difference Time Domain (FDTD)^[81], Method of Moments (MOM)^[82] and so on. In this work, an existing open-source code, Meep, which implements the EM simulation using FDTD, was used.

2.1.2.1 Finite Difference Time Domain

The Finite-Difference Time-Domain (FDTD) method is ideally suited for highly inhomogeneous meshes because of its ability of scaling with the mesh size. Moreover, it provides the possibility of simple parallelization and hardware acceleration. Therefore FDTD is the selected numerical method for solving Maxwell's Equations in this work. Here are the implementation details of the FDTD method.

2.1.2.1.1 Ampere's Law and Faraday's Law

Ampere's Law and Faraday's Law are the relevant governing equations in constructing the FDTD algorithm. As electric and magnetic fields are vectors, then mathematically the two laws are expressed as the following:

$$-\sigma_m \mathbf{H} - \mu \frac{\partial \mathbf{H}}{\partial t} = \nabla \times \mathbf{E} = \begin{vmatrix} \mathbf{a}_x & \mathbf{a}_y & \mathbf{a}_z \\ \frac{\partial}{\partial x} & \frac{\partial}{\partial y} & \frac{\partial}{\partial z} \\ E_x & E_y & E_z \end{vmatrix} \quad (2.2-1)$$

$$\sigma \mathbf{E} + \epsilon \frac{\partial \mathbf{E}}{\partial t} = \nabla \times \mathbf{H} = \begin{vmatrix} \mathbf{a}_x & \mathbf{a}_y & \mathbf{a}_z \\ \frac{\partial}{\partial x} & \frac{\partial}{\partial y} & \frac{\partial}{\partial z} \\ H_x & H_y & H_z \end{vmatrix} \quad (2.2-2)$$

Expand equations (2.2-1) and (2.2-2), then we get

$$-\sigma_m H_x - \mu \frac{\partial H_x}{\partial t} = \frac{\partial E_z}{\partial y} - \frac{\partial E_y}{\partial z} \quad (2.2-3)$$

$$-\sigma_m H_y - \mu \frac{\partial H_y}{\partial t} = \frac{\partial E_x}{\partial z} - \frac{\partial E_z}{\partial x} \quad (2.2-4)$$

$$-\sigma_m H_z - \mu \frac{\partial H_z}{\partial t} = \frac{\partial E_y}{\partial x} - \frac{\partial E_x}{\partial y} \quad (2.2-5)$$

$$\sigma E_x + \epsilon \frac{\partial E_x}{\partial t} = \frac{\partial H_z}{\partial y} - \frac{\partial H_y}{\partial z} \quad (2.2-6)$$

$$\sigma E_y + \epsilon \frac{\partial E_y}{\partial t} = \frac{\partial H_x}{\partial z} - \frac{\partial H_z}{\partial x} \quad (2.2-7)$$

$$\sigma E_z + \epsilon \frac{\partial E_z}{\partial t} = \frac{\partial H_y}{\partial x} - \frac{\partial H_x}{\partial y} \quad (2.2-8)$$

2.1.2.1.2 Yee Grid

FDTD is to replace the partial differentials with finite differences in both the time domain and the spatial domain. Thus, finite difference and discretization of both the spatial grid and the time grid are the two key points of the method FDTD.

A grid is imposed over the volume of interest such that the grid coordinates (i, j, k) are expressed as (i Δx, j Δy, k Δz) where Δx, Δy and Δz are the spatial increments in x, y, and z within the grid. A function F, which is a function of space and time, is expressed as:

$$F(i \Delta x, j \Delta y, k \Delta z, n \Delta t) = F^n(i, j, k)$$

$$\Delta x = \Delta y = \Delta z = \delta$$

where δ denotes the space increment, Δt the time increment and n an integral time index.

Central finite-difference approximations that are second-order accurate in space and time to represent spatial and temporal derivatives of \vec{F} are used:

$$\frac{\partial F^n(i,j,k)}{\partial x} = \frac{F^n(i+\frac{1}{2},j,k) - F^n(i-\frac{1}{2},j,k)}{\delta} \quad (2.2-9)$$

$$\frac{\partial F^n(i,j,k)}{\partial t} = \frac{F^{n+1/2}(i,j,k) - F^{n-1/2}(i,j,k)}{\Delta t} \quad (2.2-10)$$

Yee grid, presented in [83], was to implement staggered grids in space and time for each electric and magnetic vector field component in Maxwell's curl equations, as shown in Fig.4. The electric components are in the middle of the edges and the magnetic components are in the centre of the faces.

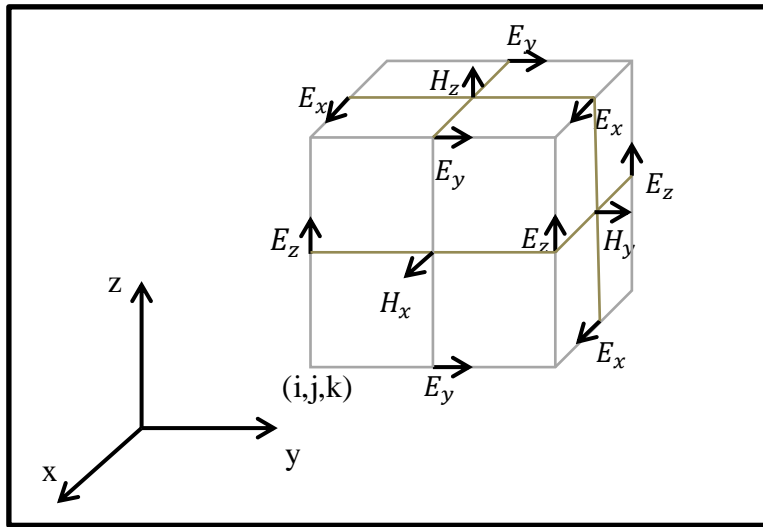


Fig.4 Electric and magnetic field components on unit cell used in the Yee Grid

By using the Yee grid, components of \mathbf{E} and \mathbf{H} are interleaved by the spatial interval of $\delta/2$, where δ is the spatial increment, and the temporal interval of $\Delta t/2$, where Δt is the temporal increment, to implement finite differences. Applying equations (2.2-9) and (2.2-10) to the scalar equations (2.2-3) to (2.2-8) results in the following explicit finite-difference equations:

$$H_x^{q+\frac{1}{2}} \left[m, n + \frac{1}{2}, p + \frac{1}{2} \right] = \frac{1 - \frac{\sigma_m \Delta t}{2\mu}}{1 + \frac{\sigma_m \Delta t}{2\mu}} H_x^{q-\frac{1}{2}} \left[m, n + \frac{1}{2}, p + \frac{1}{2} \right] + \frac{1}{1 + \frac{\sigma_m \Delta t}{2\mu}} \left(\frac{\Delta t}{\mu \Delta z} \left\{ E_y^q \left[m, n + \frac{1}{2}, p + 1 \right] - E_y^q \left[m, n + \frac{1}{2}, p \right] \right\} - \frac{\Delta t}{\mu \Delta y} \left\{ E_z^q \left[m, n + 1, p + 1/2 \right] - E_z^q \left[m, n, p + \frac{1}{2} \right] \right\} \right) \quad (2.2-11)$$

$$H_y^{q+\frac{1}{2}} \left[m + \frac{1}{2}, n, p + \frac{1}{2} \right] = \frac{1 - \frac{\sigma_m \Delta t}{2\mu}}{1 + \frac{\sigma_m \Delta t}{2\mu}} H_y^{q-\frac{1}{2}} \left[m + \frac{1}{2}, n, p + \frac{1}{2} \right] + \frac{1}{1 + \frac{\sigma_m \Delta t}{2\mu}} \left(\frac{\Delta t}{\mu \Delta x} \left\{ E_z^q \left[m + 1, n, p + \frac{1}{2} \right] - E_z^q \left[m, n, p + \frac{1}{2} \right] \right\} - \frac{\Delta t}{\mu \Delta z} \left\{ E_x^q \left[m + 1/2, n, p + 1 \right] - E_x^q \left[m + \frac{1}{2}, n, p \right] \right\} \right) \quad (2.2-12)$$

$$H_z^{q+\frac{1}{2}} \left[m + \frac{1}{2}, n + \frac{1}{2}, p \right] = \frac{1 - \frac{\sigma_m \Delta t}{2\mu}}{1 + \frac{\sigma_m \Delta t}{2\mu}} H_z^{q-\frac{1}{2}} \left[m + \frac{1}{2}, n + \frac{1}{2}, p \right] + \frac{1}{1 + \frac{\sigma_m \Delta t}{2\mu}} \left(\frac{\Delta t}{\mu \Delta y} \left\{ E_x^q \left[m + \frac{1}{2}, n + 1, p \right] - E_x^q \left[m + \frac{1}{2}, n, p \right] \right\} - \frac{\Delta t}{\mu \Delta x} \left\{ E_y^q \left[m + 1, n + 1/2, p \right] - E_y^q \left[m, n + \frac{1}{2}, p \right] \right\} \right) \quad (2.2-13)$$

$$E_x^{q+1} \left[m + \frac{1}{2}, n, p \right] = \frac{1 - \frac{\sigma \Delta t}{2\varepsilon}}{1 + \frac{\sigma \Delta t}{2\varepsilon}} E_x^q \left[m + \frac{1}{2}, n, p \right] + \frac{1}{1 + \frac{\sigma \Delta t}{2\varepsilon}} \left(\frac{\Delta t}{\varepsilon \Delta y} \left\{ H_z^{q+1/2} \left[m + \frac{1}{2}, n + 1/2, p \right] - H_z^{q+1/2} \left[m + \frac{1}{2}, n - 1/2, p \right] \right\} - \frac{\Delta t}{\varepsilon \Delta z} \left\{ H_y^{q+1/2} \left[m + 1/2, n, p + 1/2 \right] - H_y^{q+1/2} \left[m + \frac{1}{2}, n, p - 1/2 \right] \right\} \right) \quad (2.2-14)$$

$$E_y^{q+1} \left[m, n + \frac{1}{2}, p \right] = \frac{1 - \frac{\sigma \Delta t}{2\varepsilon}}{1 + \frac{\sigma \Delta t}{2\varepsilon}} E_y^q \left[m, n + \frac{1}{2}, p \right] + \frac{1}{1 + \frac{\sigma \Delta t}{2\varepsilon}} \left(\frac{\Delta t}{\varepsilon \Delta z} \left\{ H_x^{q+1/2} \left[m, n + \frac{1}{2}, p + \frac{1}{2} \right] - H_x^{q+1/2} \left[m, n + \frac{1}{2}, p - \frac{1}{2} \right] \right\} - \frac{\Delta t}{\varepsilon \Delta x} \left\{ H_z^{q+1/2} \left[m + 1/2, n + 1/2, p \right] - H_z^{q+1/2} \left[m - 1/2, n + 1/2, p \right] \right\} \right) \quad (2.2-15)$$

$$E_z^{q+1} \left[m, n, p + \frac{1}{2} \right] = \frac{1 - \frac{\sigma \Delta t}{2\varepsilon}}{1 + \frac{\sigma \Delta t}{2\varepsilon}} E_z^q \left[m, n, p + \frac{1}{2} \right] + \frac{1}{1 + \frac{\sigma \Delta t}{2\varepsilon}} \left(\frac{\Delta t}{\varepsilon \Delta x} \left\{ H_y^{q+1/2} \left[m + 1/2, n, p + \frac{1}{2} \right] - H_y^{q+1/2} \left[m - \frac{1}{2}, n, p + \frac{1}{2} \right] \right\} - \frac{\Delta t}{\varepsilon \Delta y} \left\{ H_x^{q+1/2} \left[m, n + 1/2, p + 1/2 \right] - H_x^{q+1/2} \left[m, n - 1/2, p + 1/2 \right] \right\} \right) \quad (2.2-16)$$

2.1.2.2 Spatial and Time Resolution

In numerical algorithms, spatial and time resolutions are of great importance for convergent solutions.

The spatial grid increment must be such that over one increment the electromagnetic field does not change significantly. This means that to have meaningful results, the linear dimension of the grid must be only a fraction of the wavelength. It has been verified that at least 10 cells per wavelength are necessary to ensure a meaningful result. The wavelength here considered is the smallest wavelength in the simulation.

Once the spatial grid increment has been determined, the time step is chosen considering computational stability conditions. For stability, a field component cannot propagate more than one spatial cell in the time step Δt . Assuming $\Delta_x = \Delta_y = \Delta_z = \Delta$, then the stability condition can be expressed as

$$\Delta t \leq \frac{\Delta}{C_0 \sqrt{d}}$$

where C_0 is the speed of light in vacuum, and $d = 1, 2$ or 3 for one-, two-, three-dimensional simulations, respectively.

2.1.2.3 Boundary Condition

According to the updating equations of electric and magnetic fields, to calculate electric fields, it is necessary to know the surrounding magnetic field values. And vice versa, the surrounding electric field values needs to be known in order to calculate magnetic fields. However, the size of the volume that can be simulated using FDTD is limited by computer resources, and it is not an infinite space as the real electromagnetic propagating space. Then at the edge of the simulated volume, the corresponding values of one side will not be known. Thus, boundary conditions which do not disturb the electromagnetic field need to be assumed and used. To be simple, a boundary condition is a rule to properly truncate the simulation volume.

The two most commonly used such boundary conditions are Absorbing Boundary Condition (ABC) and Perfectly Matched Layer (PML).

The ABC technique was first formulated by B. Engquist and E. Majda in 1977^[84]. ABC works like other boundaries conditions, like Dirichlet or Neumann boundary conditions, to set proper boundary values for the unknowns of partial differential equations by extrapolation from the interior grid points to the edge grid points so that only a small reflection coefficient is yielded on the truncation boundary. However, ABC can only be accurately implemented in one-dimension cases. For 2D or 3D cases, existing ABCs restrict themselves to absorbing waves exactly only at a few angles, especially normal-incident incidence. Another restriction of ABC is that many standard ABCs are formulated only for homogeneous materials at the boundaries, and may even become numerically unstable with inhomogeneous boundaries.

The PML concept was introduced by J.-P. Berenger in 1994^[85]. Although PML is also classified into boundary conditions, it is actually an absorbing region adjacent to the actual computer volume rather than a conventional boundary condition, and can provide orders-of-magnitude lower reflections. In PML, a coordinate transformation is performed in which the coordinate normal to the artificial boundary is mapped to complex numbers, so that an analytic continuation of the wave equation is transformed into complex coordinates and the complex-material region, and thus propagating waves are replaced by exponentially decaying waves. Therefore as long as the complex-material region is truncated after a long enough distance, the decaying waves will only yield few reflections at the border no matter what boundary conditions are used.

2.1.3 Modified Infinitesimal Dipole Model

The basic idea of the conventional IDM is the substitution of the AUT by an equivalent series of infinitesimal dipoles which distributions in the physical region of the AUT and radiates the same near field as the AUT.^[60] The equivalent series of infinitesimal dipoles is searched by optimization algorithms. In this work, in order to simplify the optimization objective function and to reduce computational cost, a modified IDM in which elemental dipoles are pre-defined is proposed.

2.1.3.1 Dipole Definition

An infinitesimal dipole placed at $\mathbf{r}_i = (x_i, y_i, z_i)$, with orientation described by angles α_i , β_i and γ_i defined with respect to the x -, y - and z -axis, and excited by a finite oscillating current proportional to $e^{j(\omega t + \theta)}$ can be represented by nine-component vector

$$\mathbf{d}_i = (I_i, \omega, \theta_i, \alpha_i, \beta_i, \gamma_i, x_i, y_i, z_i) . \quad (2.3-1)$$

where the variable I_i is the magnitude of the current of the dipole, ω and θ denote the frequency and the initial phase of the oscillating current respectively. Only electric dipoles were considered in this work. Mathematically the third directional cosine is obtained from the following equation:

$$(\cos(\gamma_i))^2 = 1 - (\cos(\alpha_i))^2 - (\cos(\beta_i))^2. \quad (2.3-2)$$

Current magnitude components of dipole \mathbf{d}_i in Cartesian coordinates are then given as

$$I_{i_x} = I_i \cos(\alpha_i), I_{i_y} = I_i \cos(\beta_i), I_{i_z} = I_i \cos(\gamma_i). \quad (2.3-3)$$

where subscripts x, y, z denote the three orthogonal components in Cartesian coordinates, respectively.

Therefore, vector \mathbf{d}_i is reformulated into vector $\tilde{\mathbf{d}}_i$:

$$\tilde{\mathbf{d}}_i = (I_{i_x}, I_{i_y}, I_{i_z}, \omega, \theta_i, x_i, y_i, z_i). \quad (2.3-4)$$

The frequency of the IDM is identical to the excitation frequency of the AUT. In order to reduce the complexity of the optimization problem, a fixed number of infinitesimal dipoles with fixed positions, distributed within the physical volume of the AUT were used. Thus, the three position parameters x_i, y_i, z_i were bypassed.

All in all, a dipole is characterized by four variables:

$$\bar{\mathbf{d}}_i = (I_{i_x}, I_{i_y}, I_{i_z}, \theta_i). \quad (2.3-5)$$

A series of N dipoles is represented by an IDM weighting vector, a $4N$ -component vector,

$$\mathbf{C} = (\bar{\mathbf{d}}_1, \bar{\mathbf{d}}_2, \dots, \bar{\mathbf{d}}_N). \quad (2.3-6)$$

2.1.3.2 Electric Field Computation

Based on the electromagnetic theory, for time-harmonic electromagnetic waves, the electric field of dipole $\bar{\mathbf{d}}_i$ is derived from the electric field of elemental dipole $\tilde{\mathbf{d}}_{oi}$, which has the same location and frequency as dipole $\bar{\mathbf{d}}_i$, and is defined using the elemental vector:

$$\tilde{\mathbf{d}}_{oi} = (x_i, y_i, z_i, \omega, I_{o_x}, I_{o_y}, I_{o_z}, \theta_{oi} = 0) \quad (2.3-7)$$

where $I_{o_x}, I_{o_y}, I_{o_z}$ are determined to be constant values of the same order of the problem, e.g. 1 [A] here.

Therefore, it is derived that

$$\mathbf{E}_{i_x} = \left(\frac{I_{i_x}}{I_{o_x}} \right) * \mathbf{E}_{oi_x} * e^{i\omega(\theta_i - \theta_{oi})} \quad (2.3-8-1)$$

$$\mathbf{E}_{i_y} = \left(\frac{I_{i_y}}{I_{o_y}} \right) * \mathbf{E}_{oi_y} * e^{i\omega(\theta_i - \theta_{oi})} \quad (2.3-8-2)$$

$$\mathbf{E}_{i_z} = \left(\frac{I_{i_z}}{I_{o_z}} \right) * \mathbf{E}_{oi_z} * e^{i\omega(\theta_i - \theta_{oi})} \quad (2.3-8-3)$$

where $\mathbf{E}_{i_x}, \mathbf{E}_{i_y},$ and \mathbf{E}_{i_z} denote electric fields respectively contributed by I_{i_x}, I_{i_y} and I_{i_z} . Similarly, $\mathbf{E}_{oi_x}, \mathbf{E}_{oi_y},$ and \mathbf{E}_{oi_z} are elemental electric fields respectively contributed by I_{oi_x}, I_{oi_y} and I_{oi_z} .

Then the electric field of the dipole $\tilde{\mathbf{d}}_{oi}$ is calculated based on the field of the corresponding elemental dipole $\tilde{\mathbf{d}}_{oi}$ using equations (2.3-9-1), (2.3-9-2) and (2.3-9-3).

$$Re(\mathbf{E}_{i_x}) = (I_{i_x}/I_{o_x}) * (Re(\mathbf{E}_{oi_x}) * \cos(\theta_i) - Im(\mathbf{E}_{oi_x}) * \sin(\theta_i)) \quad (2.3-9-1)$$

$$Re(\mathbf{E}_{i_y}) = (I_{i_y}/I_{o_y}) * (Re(\mathbf{E}_{oi_y}) * \cos(\theta_i) - Im(\mathbf{E}_{oi_y}) * \sin(\theta_i)) \quad (2.3-9-2)$$

$$Re(\mathbf{E}_{i_z}) = (I_{i_z}/I_{o_z}) * (Re(\mathbf{E}_{oi_z}) * \cos(\theta_i) - Im(\mathbf{E}_{oi_z}) * \sin(\theta_i)) \quad (2.3-9-3)$$

The total electric field radiated by a series of infinitesimal dipoles is a function of the IDM weighting vector, and can be easily calculated using equations (2.3-9-1)-(2.3-9-3) based on the beforehand calculated fields of the elemental dipoles.

$$\mathbf{E}(\mathbf{C}) = \mathbf{E}(\bar{\mathbf{d}}_1, \bar{\mathbf{d}}_2, \dots, \bar{\mathbf{d}}_N) = \sum_{i=1}^N \mathbf{E}(\bar{\mathbf{d}}_i) = \sum_{i=1}^N (\bar{\mathbf{d}}_i, \mathbf{E}_{0i}(\mathbf{r}_i)) \quad (2.3-10)$$

where \mathbf{E} is the total electric field from the N dipoles, \mathbf{E}_i the electric field from dipole $\bar{\mathbf{d}}_i$, and \mathbf{E}_{0i} is the elemental electric field radiated by elemental dipole $\bar{\mathbf{d}}_{0i}$ located at a predefined position \mathbf{r}_i .

2.1.3.3 Objective Function

In order to minimize the difference between the actual electrical field of the AUT and the simulated electrical field radiated by the series of infinitesimal dipoles, the following objective function has been introduced:

$$F(\mathbf{C}) = \sqrt{\left(\frac{\sum_{m=1}^M (|Ea_x(\mathbf{r}_m) - E_x(\mathbf{r}_m, \mathbf{C})|^2 + |Ea_y(\mathbf{r}_m) - E_y(\mathbf{r}_m, \mathbf{C})|^2 + |Ea_z(\mathbf{r}_m) - E_z(\mathbf{r}_m, \mathbf{C})|^2)}{\sum_{m=1}^M (|Ea_x(\mathbf{r}_m)|^2 + |Ea_y(\mathbf{r}_m)|^2 + |Ea_z(\mathbf{r}_m)|^2)} \right)} \quad (2.3-11)$$

$$\mathbf{Ea}(\mathbf{r}_m) = \{Ea_x(\mathbf{r}_m), Ea_y(\mathbf{r}_m), Ea_z(\mathbf{r}_m)\} \quad (2.3-12-1)$$

$$\mathbf{E}(\mathbf{r}_m, \mathbf{C}) = \{E_x(\mathbf{r}_m, \mathbf{C}), E_y(\mathbf{r}_m, \mathbf{C}), E_z(\mathbf{r}_m, \mathbf{C})\} \quad (2.3-12-2)$$

where M is the total number of observation points over the near field, \mathbf{r}_m is the position vector of the observation point m , $\mathbf{Ea}(\mathbf{r}_m)$ is the actual electric field of the AUT, and $\mathbf{E}(\mathbf{r}_m, \mathbf{C})$ is the simulated electric field of the series of infinitesimal dipoles.

2.1.3.4 Optimization

Before optimization, the electric fields of all the elemental dipoles are simulated and calculated. Then the optimization process, during which the simulated electric field of the AUT is updated using equations (2.3-9-1), (2.3-9-2), (2.3-9-3) and (2.3-10), is to search for an optimal IDM weighting factor to minimize the objective function. Equation (2.3-11) defines a multimodal objective function $F(\mathbf{C})$ with many local minima. Hence, local optimization would not be sufficient. We opted for OQNLP^[86] as heuristic for global optimization. OQNLP is designed to find global optima for nonlinear problems with many constraints and variables, where all objective functions are differentiable with respect to the continuous variables. Internally this method is based on OptQuest, a commercial implementation of scatter search developed by OptTek Systems, Inc., to provide starting points for any gradient-based local solver for nonlinear programming (NLP) problems.

2.1.4 Applicators with Strong Mutual Coupling

When the mutual coupling between antenna elements of an applicator is weak, it is reasonable and possible to replace each antenna by the dipole model that was obtained from a single isolated antenna and then to superimpose as many dipole models as the applicator has. However, when the distance between antenna elements is below to a certain critical distance, the mutual coupling begins to significantly influence the radiated fields.^[87] In the SIGMA-Eye applicator, each antenna element has several antenna neighbors, which are less than half of the wavelength of 100 MHz waves in water (27 cm) away. Thus, to simulate the

applicator, it is essential to take into account the mutual interactions between antenna neighbors.

The basic-building-block-based Infinitesimal Dipole Model proposed by Said M.Mikki etc.^[70] was employed in this paper. According to ^[70], the mutual coupling between antenna elements is treated as a multiple scattering effect where the field radiated by antenna A will hit antenna B and scatters back as E_B , to the location of antenna A. This scattered field E_B will be in turn scattered by antenna A back to antenna B, and this process will go on indefinitely. Thus, the objective of this work now is to search for an equivalent dipole model of the AUT which contains multiple scattering effects of neighboring antennas.

The idea is to create a basic building block for AUT, which contains the AUT and the neighboring antennas, as shown in Fig.5. The antenna in the middle is the AUT and excited as an active antenna, and the other two antennas are passive, that is to say that they will not be excited by energy sources, but the source impedance is left in the block ^[70]. Then, the near field data of the block is obtained by high-resolution near field measurement setup or an accurate numerical full-wave solution. Afterwards, as described in Section 2.1.3, the modified IDM, combined with the OQNLP algorithm, is employed to find an equivalent dipole model for the AUT, taking the near field data of the block as reference. Of importance is that the dipoles are allowed to only stay in the small dotted box enclosing the active antenna. In this way, the dipole model contains the effect of mutual coupling between neighboring antennas.

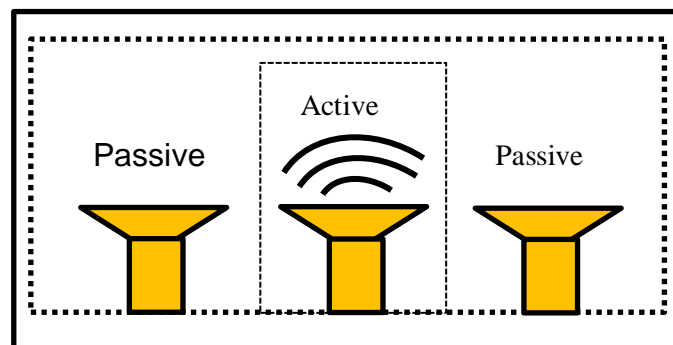


Fig.5: Basic building block for an equivalent model that takes into account the interaction between closely packed array elements

2.1.5 A Complete Solution of the Applicator

The electric field of the SIGMA-Eye applicator was represented by the superposition of fields radiated by the modified equivalent dipole models of each basic building block of each antenna.

2.1.6 Global Optimization Algorithm

Since the objective function of the IDM is highly nonlinear and full of local minima, global optimization algorithms are necessary to find the equivalent dipole set.

Over the last three decades, various global optimization algorithms have been developed specified for different kinds of mathematical problems, e.g. nonconvex, mixed-integer, differential-algebraic, bilevel, and non-factorable problems. Here the OptQuest Nonlinear Programming (OQNLP) algorithm was employed to search for equivalent dipole sets. OQNLP is designed to find global optima for nonlinear problems with many constraints and variables, where all objective functions are

differentiable with respect to the continuous variables.^[86] Internally OQNLP combines the scatter search method and a gradient-based local optimization solver for nonlinear programming problems. The scatter search method provides starting points to the local optimization solver, and thus can improve the reliability of any local optimization solver by calling the solver with many starting points.

Scatter search was firstly proposed by Fred Glover^[88], and the basic idea is to maintain a small subset of the reference set, and create new combined solutions. The basic scatter search procedure is as follows:

- i) A diversification generation method is used to generate a large collection of diverse trial solutions.
- ii) An improvement method is to transform the trial solution from the last method into one or more enhanced trial solutions.
- iii) Based on the diversity and quality of those trial solutions produced by the improvement method, a reference set update method is to build and maintain a reference set.
- iv) A subset generation method is to produce a subset of its solutions as a basis for creating combined solutions based on the reference set from the third method.
- v) A solution combination method is to generate new solutions by combination of the elements of the subset from the fourth method.
- vi) The combinations from Step 5 are used as starting points for a new application of the previous 5 steps. Repeat these steps until reaching a specified iteration limit.

The scatter search method is flexible to be combined with any gradient-based optimization solvers, and in this work the barrier interior point method^[89] was used. As the same as many other constrained optimization methods, it introduces penalty functions to transform a constrained optimization problem to an unconstrained optimization, and then iterate to converge the optimal. The central idea is to build a 'barrier', i.e. a logarithmic barrier function, on the boundary of the feasibility domain of the problem, so that each time when the iteration point is close to the barrier, the objective function would increase a lot as a penalty, to prevent the iteration point goes outside the feasibility domain. Therefore, the optimal will stay in the feasibility domain.

2.2 Implementation

2.2.1 Development Setup

As this work is actually a software project, here the computer configuration is listed.

- i) Operating system: Windows 7 64-bit.
- ii) Processor: Intel(R) Core(TM) i7-5820K CPU @ 3.30GHz
- iii) Installed memory (RAM): 32.00 GB.
- iv) Programming environments: Visual Studio 2010, Matlab R2017a.

In this paper, elemental electric fields of dipoles were calculated by the free FDTD simulation software package, Meep^[90]. COMSOL Mutliphysics^[52], a commercial software package, providing multi-physics simulations including Antenna Simulation, was utilized to generate near field of the basic building blocks as references of the IDM.

2.2.2 Applicator and Phantom Setup

A specific system that was modeled via the proposed approach is the SIGMA-Eye applicator (BSD Medical Corporation), which is shown in Fig.6. The SIGMA-Eye

applicator is a phased-array applicator which is composed of 24 identical antennas distributed in three eye-shaped rings. It has dimensions of 58 cm (horizontal) × 40 cm (vertical) × 50 cm (longitudinal). The basic frame is a cylinder made of acrylic glass with the eye-shaped cross section. The water bolus, attached to its internal sides is a closed silicone membrane filled with deionized water, filling the whole space between the phantom and the outer cylinder. The water bolus is necessary to cool the device on the outer surface of the phantom and to direct the radio-waves onto the phantom by impedance matching.

The 24 antennas arranged over the three eye-shaped rings are placed directly on the internal surface of the Lucite wall and covered with a thin isolating adhesive tape.^[56] Two operating parameters control the power and the phase of the irradiated field for each of the applicator’s 12 channels to steer a 3D heating pattern whereby each channel is built up from two antennas. Each antenna is about 12.5 cm long, and consists of two flat, quasi-conical copper strips, as shown in Fig.7. For the convenience of the following analysis, the 24 antennas are labeled as antenna 01 to antenna 24 from the lower ring to the upper ring and in the counter clock wise on each ring. As it is shown in Fig.6 (b), the antenna on the upper-right corner of the lower ring is antenna 01, and the one on the left to it is antenna 04. An elliptical phantom with 1 cm-thick outer “fat” wall, filled with the physiological salt solution was placed inside the applicator as a simple patient model.

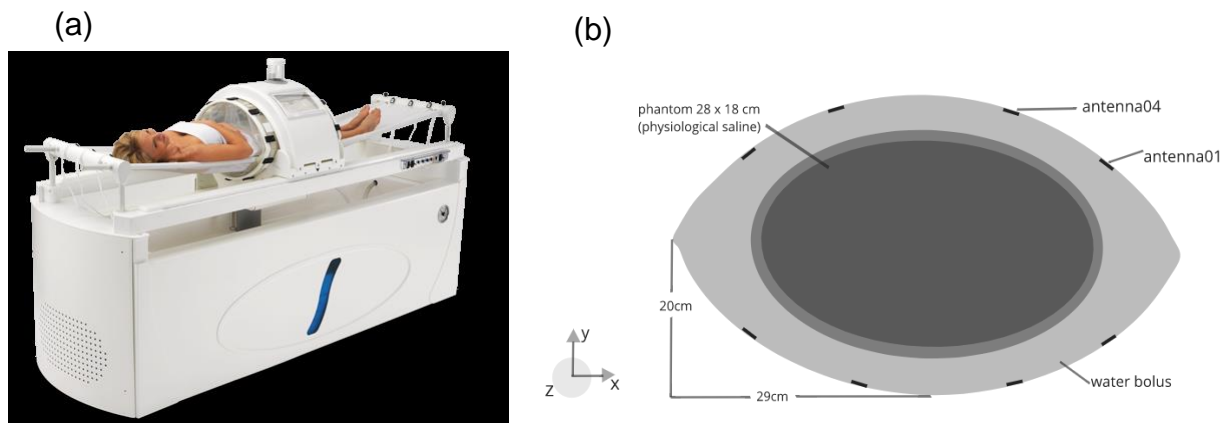


Fig.6: (a) The SIGMA-Eye applicator ^[91]; (b) Cross section of the SIGMA-Eye applicator

According to the ^[63], 100 MHz is an applicable excitation frequency for the three-ring applicator. Electric properties of different materials at 100 MHz excitation frequency used in the simulations are summarized in Tab.1.

Tab.1: Material properties at 100 MHz excitation frequency

Material	Relative Permittivity	Conductivity[S/m]
Air	1	0
Water Bolus	78	0
Plastic	2.8	0
Saline	78.4	0.499
Fat	10	0.0684

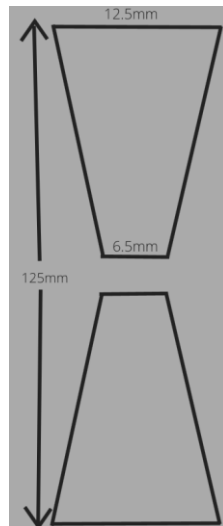


Fig.7: Topology of the antenna used in the Sigma-Eye applicator

2.2.3 COMSOL Multiphysics

COMSOL Multiphysics is a cross-platform software which implements multiple physics simulations based on finite element analysis. It is consisted of several modules for different applications, e.g. AC/DC Module, CAD Import Module, Chemical Engineering Module, Heat Transfer Module, RF Module and so on.

In this work, bow-tie antennas were created and simulated using RF Module in COMSOL 5.3 to generate near fields of bow-tie antennas as reference (measurement data) used in the IDM. The idea is that the bow-tie antenna embedded in the SIGMA-Eye Applicator is realized with two thin metallic arms that have a sinusoidal voltage difference applied between them.

Here are some more details about the implementation.

i) Geometry of the antenna

The model of the antenna consists of two hexahedrons representing each of the dipole arms, and a cuboid filled the gap in-between the two arms representing the voltage source.

ii) Boundary conditions

The power supply and feed structure are not modelled explicitly, but a uniform voltage difference, named port in COMSOL, is applied to the gap. This source induces electromagnetic fields and surface currents on the adjacent conductive faces. Moreover, the dipole arm surfaces are modelled using the impedance boundary condition, which is appropriate for conductive surface. This boundary condition introduces a finite conductivity at the surface as well as resistive losses.

The computational volume around the antenna is truncated with a PML that acts itself as an absorber of outgoing radiation.

iii) Basic building block

When creating a basic building block, create the geometry models for each antenna of the block, and do not apply voltage sources to all the antennas but the active one.

2.2.4 Optimization Using OQNLP

The global optimization toolbox of Matlab provides functions that search for global solutions to problems containing multiple maxima or minima. Global Search is one of the functions of the toolbox, which implements the OQNLP method. Therefore, in this work, the function Global Search (GS) of Matlab was used to perform the global optimization of the objective function of the IDM.

The workflow is illustrated in the following Fig.8. To use the GS solver, a problem structure needs to be firstly created using the function createOptimProblem. This means to define an objective function and a start point, to set bounds and constraints and to select a local solver. And then the next step is to create a solver object, which refers to create a GlobalSearch object. At last start optimization by calling the function “run” which combines the GlobalSearch object and the problem structure.

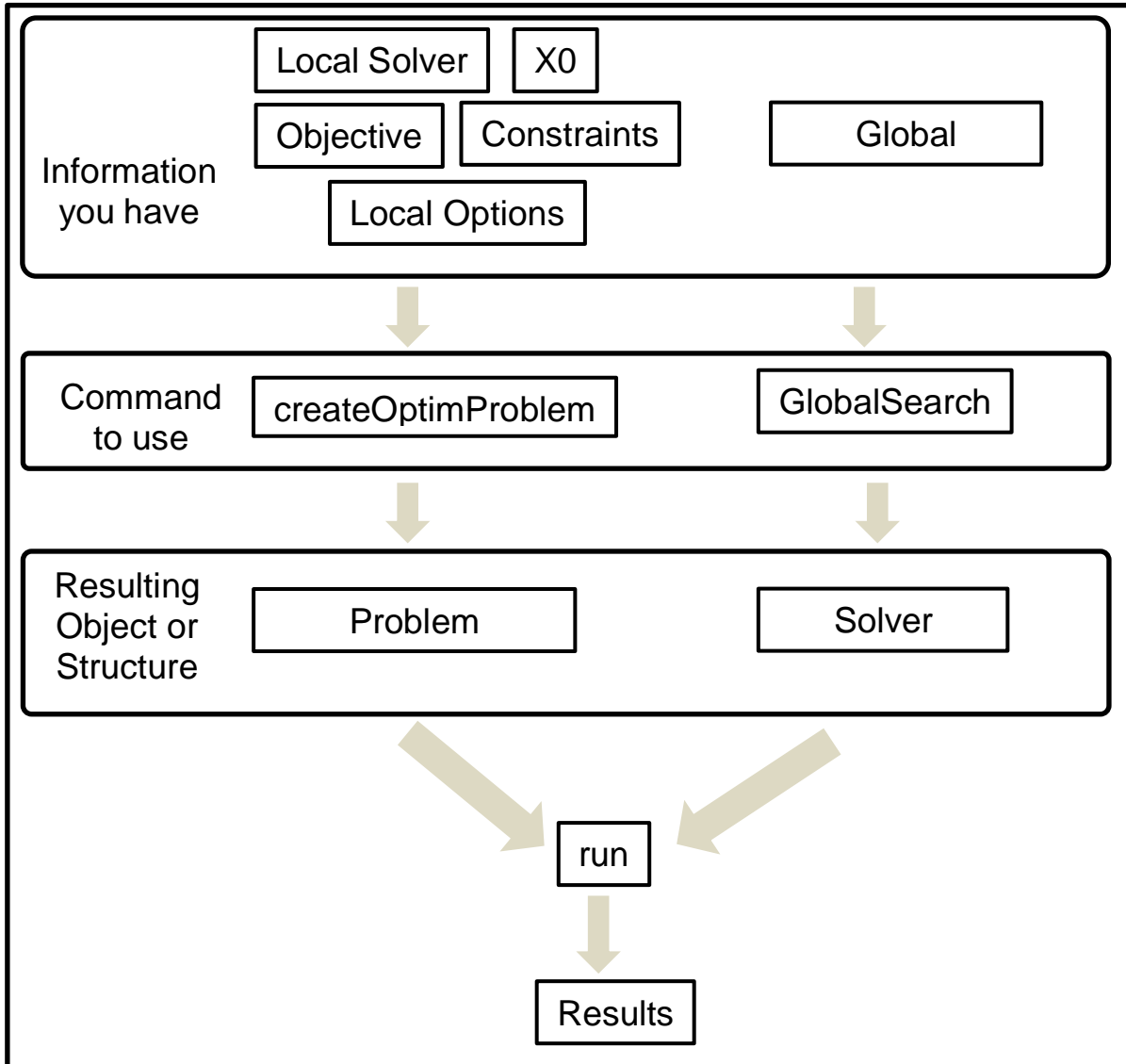


Fig.8: Workflow of GlobalSearch in Matlab

2.2.5 SIGMA-Eye Applicator Modeling

The Sigma-Eye applicator simulation was implemented step by step as follows.

- i) 24 basic building blocks for the 24 antennas in the SIGMA-applicator were created. For each block, the AUT, for example, for the block of antenna 01, the antenna 01 was the AUT, was taken as the active antenna, and all the other 23 antennas were taken as the passive ones. Based on the symmetrical topology of the antennas distributed in the applicator, there are four typical types of antenna positions in the applicator, respectively for antenna 01, antenna 02, antenna 04, and antenna 05. The other antennas are located symmetrically to the four typical antennas. It had been expected that the dipole models for the other antennas can be derived from the ones of the four typical antennas. However, the results of

the optimal IDM-weighting parameters of the antennas located on the middle ring, which have a symmetrical antenna-neighboring environment along z-axis, showed that the dipoles were not symmetrically distributed along z-axis (as shown in Tab-Appendix.2 and Tab-Appendix.4). Therefore it came to the conclusion that a specific basic-building-block for each antenna of the 24 antennas should be created.

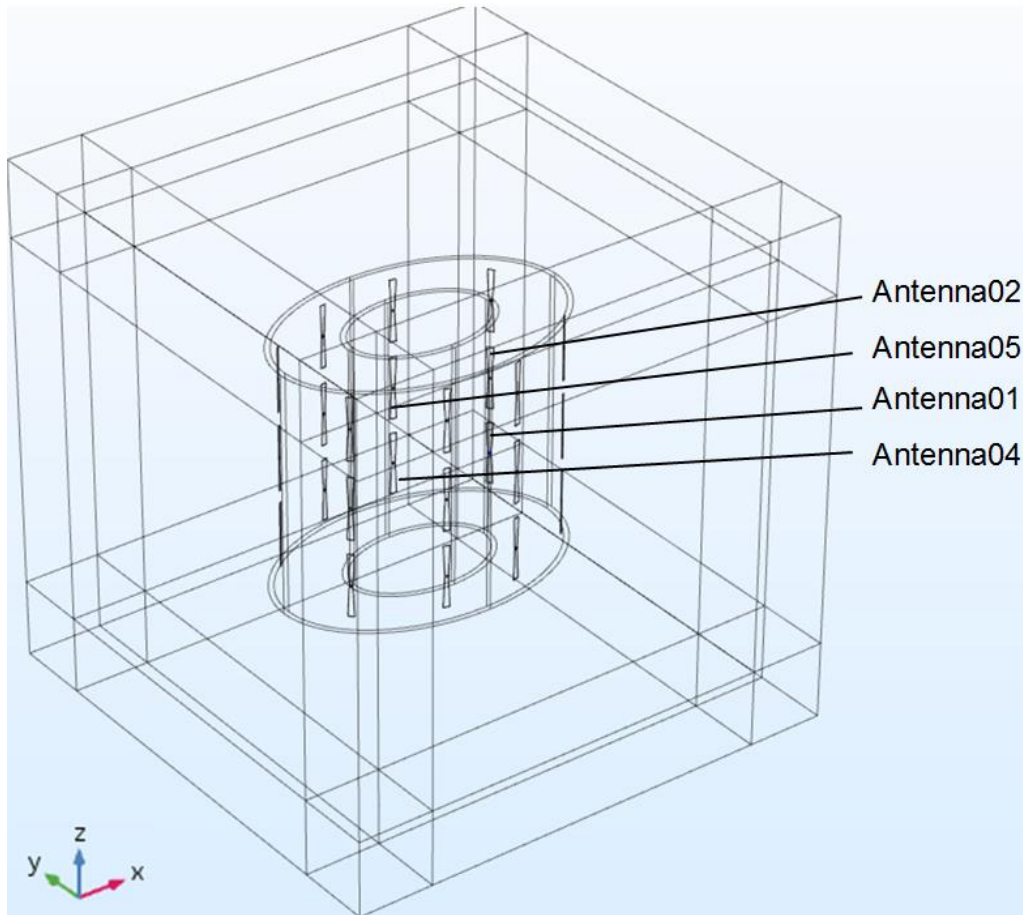


Fig.9: Topology of the SIGMA-Eye applicator simulated in COMSOL

- ii) Each basic building block was assumed to be placed in the equivalent water medium (relative permittivity = 78, electrical conductivity = 0 S/m). The center of the corresponding AUT was fed by a harmonic source with the frequency of 100 MHz. The physical volume of the corresponding AUT was approximated by a cuboid with the size of 2.5 cm × 2.5 cm × 15 cm centered at the feed point. A series of fixed-number dipoles was evenly distributed on a regular grid, which represented the cuboid. The near field of each dipole in the water equivalent water medium was simulated using the Meep library ^[90], and the near field data of the block was obtained from COMSOL ^[52]. Observation points of the near field were distributed in the phantom region shown in Fig.6 (b). Using the observation points, the relative difference was calculated by Equation (2.3-11).
- iii) For each block, OQNLP was used to search for the minimum of the objective function to determine the IDM weighting vector whereby the simulated electric fields of dipoles were updated using equations(2.3-9-1), (2.3-9-2) and (2.3-9-3).
- iv) The SIGMA-Eye applicator was simulated by superposing the 24 simulated antennas located in the same positions as in the actual applicator.

3 RESULTS

3.1 Parameter Determination in Meep

As mentioned before, the spatial resolution and PML boundary conditions are two important factors when using numerical algorithms for solving Maxwell's Equations. In this work, the open-source software Meep was used for calculating electromagnetic fields via the numerical algorithms, FDTD and FDFD. Therefore, several experiments were performed to determine the spatial resolution and the PML thickness.

3.1.1 PML Thickness Determination

As a rule of thumb, a PML thickness comparable to half a wavelength usually works pretty well. But this large PML thickness increases the computational burden a lot. Therefore, in practice, the common idea to determine the PML thickness is to keep doubling the PML thickness until the accuracy we are interested in is achieved.

For convenience, Meep's frequency-domain solver, which is used to compute the fields produced in a geometry in response to a continuous-wave source, was employed. Using the frequency-domain solver, a convergent tolerance parameter needs to be defined. If the tolerance parameter is successfully achieved, the solver will return true, otherwise it will return 'Convergence failure'.

It was assumed that there was a water-filled cubic computational volume of 100 cm * 100 cm * 100 cm, and an infinitesimal current dipole driven by a 100 MHz-continuous-wave current was placed inside the volume. If the center of the volume was taken as the original of the Cartesian coordinate system, then the dipole was at the position(-30 cm, -20 cm, -40 cm). In this work, the interested tolerance parameter value was $1.0 * 10^{-3}$.

Starting from 2 cm, the thickness was doubled up to 20 cm. Tab.2 illustrates the relative difference of electric fields generated with different PML thicknesses. The row of 'Diff' is the relative difference computed using equation (4.1-1) compared to the next thickness. The 'Diff' of interest should be less than $1.0 * 10^{-4}$. Therefore, the PML thickness of 15 cm is chosen to be used in this work.

$$Diff = \sqrt{\frac{\sum_i ((E_{x_1}(r_i) - E_{x_2}(r_i))^2 + (E_{y_1}(r_i) - E_{y_2}(r_i))^2 + (E_{z_1}(r_i) - E_{z_2}(r_i))^2)}{\sum_i ((E_{x_1}(r_i))^2 + (E_{y_1}(r_i))^2 + (E_{z_1}(r_i))^2)}} \quad (4.1-1)$$

where i denotes all the points inside the cubic volume, r_i the position vector of the point, and $(E_{x_1}, E_{y_1}, E_{z_1})$ and $(E_{x_2}, E_{y_2}, E_{z_2})$ stand for the electric fields with different PML thicknesses.

Tab.2: Relative difference of electric fields generated with different PML thicknesses

PML thickness	2 cm	5 cm	10 cm	15 cm	20 cm
Convergence	false	true	true	true	true
Diff	-	$2.50 * 10^{-3}$	$2.29 * 10^{-5}$	$3.11 * 10^{-6}$	-

3.1.2 Spatial Resolution Determination

The idea of spatial resolution determination, similar to that of PML thickness determination, is to keep increasing the resolution until the accuracy is good enough. On the other side, as mentioned before, at least 10 cells per wavelength are necessary to ensure a meaningful result. In this work, the typical wavelength is about 30 cm. Therefore, one cell cannot be larger than 3 cm.

The same computational volume as the one in the PML thickness determination was created, and the volume was surrounded by 15 cm-thick PM. Starting from 3 cm/cell, the cell size was decreased to 0.5 cm/cell. Here, Meep's time domain solver was used. The relative difference was calculated between the electric fields of two time points $t_1 = 8T$, and $t_2 = 12T$, where T is the time period of the field. If the difference is small enough, on one side, it means the cell size is small enough too. On the other side, it also tells that at the specified time point the convergence has been reached.

Tab.3 illustrates the relative difference of electric fields generated with different cell sizes between the two time points. The determination of the spatial resolution depends on one side on the relative difference. On the other side, the physical sizes of the objects in the environment, e.g. applicator wall, phantom wall, phantom in this work, also need to be taken into consideration. In addition, the spatial resolution significantly influences the computational time. A double resolution costs 8 times of computational time of the lower resolution. In the end, the spatial resolution used in this work was 1 cm/cell.

Tab.3: Relative difference of electric fields generated with cell sizes

Cell size(cm/cell)	3	2	1	0.5
Diff	$7.90 * 10^{-3}$	$5.50 * 10^{-3}$	$5.01 * 10^{-4}$	$2.588 * 10^{-5}$

3.2 Equivalent Dipole Models

In order to explore the effects of mutual coupling, the antennas embedded in the SIGMA-Eye applicator were simulated using both the IDM of the single isolated antenna and the basic-building-block-based IDM.

3.2.1 Equivalent Dipole Models of the Blocks

As mentioned before, the position and number of the dipoles of a dipole model is pre-defined. Therefore, one task before using the block-based modified IDM is to determine the proper number of the equivalent dipoles. The cuboid of the physical volume of the AUT was discretized into three kinds of regular grids, which corresponded to three series of dipoles. To have a statistic result, and at the same time, to avoid too much computational cost, the blocks for the four typical antennas, antenna 01, antenna 02, antenna 04, and antenna 05, were utilized here. The optimal IDM weighting vectors of the three series of dipoles were obtained using the proposed approach, the block-based modified dipole model. The optimal values of the objective function (equation 2.3-11) are presented in Tab.4.

According to Tab.4, as expected, more dipoles used in the IDM led to a lower value of the objective function, which means that the actual antenna is better approximated by the block-based modified IDM. On the other hand, it is not practical to use a too large number of dipoles in the dipole model because of high

computational cost in the optimization. To keep balance between computational cost and error function values, the number of dipoles was chosen to be $1 \times 1 \times 12$. The optimal IDM weighting vectors characterizing $1 \times 1 \times 12$ dipoles are displayed in Tab-Appendix.1, Tab-Appendix.2, Tab-Appendix.3 and Tab-Appendix.4 in the appendix respectively for the four typical basic building blocks. In the appendix, Fig-Appendix.1-Fig-Appendix.3 display the comparisons between COMSOL and the equivalent dipole models for the field components of the four blocks along the central axes of the phantom.

Using the $1 \times 1 \times 12$ dipole series, equivalent dipole models for all the 24 antennas were created, and later used for the SIGMA-Eye applicator simulation. The optimal errors are around 6.00%. Tab-Appendix.5 displays the optimal errors of the 24 equivalent dipole models.

Tab.4: Tests of the block-based modified IDMs with different numbers of dipoles

Dipole Series	Series 1	Series 2	Series 3
Dipole Number	$1 \times 1 \times 9$	$1 \times 1 \times 12$	$1 \times 1 \times 15$
Weighting Vector Length	36	48	60
Error of Block of Antenna 01	5.93%	5.76%	5.69%
Error of Block of Antenna 02	5.85%	5.69%	5.52%
Error of Block of Antenna 04	6.99%	6.98%	6.35%
Error of Block of Antenna 05	5.51%	5.21%	5.12%

3.2.2 Equivalent Dipole Models of the Single Isolated Antenna

In this part, the antenna is taken as a single isolated AUT and simulated without taken mutual coupling into consideration.

A single isolated antenna was assumed to be placed in the equivalent water medium (relative permittivity = 78, electrical conductivity = 0 S/m). Its center was fed by the harmonic source with the frequency of 100 MHz. Observation points of the near field were distributed in a box enclosing the dipole. The inner side of the box was of 0.3λ and the outer side of the box 0.8λ . The near field of the isolated AUT was simulated by COMSOL.

In order to compare to the block-based IDM, a series of dipoles $1 \times 1 \times 12$ was used, and the value of the objective function was 2.56%. The corresponding optimal IDM weighting vectors is displayed in Tab-Appendix.6. Fig-Appendix.4 illustrates the comparisons between COMSOL and the equivalent dipole model for the field components of the isolated antenna along the central circumferences of the observation box.

3.3 Comparison with the Measurement

The document of Paul F.Turner ^[92] explored the 3D energy focusing steering capability of the SIGMA-Eye applicator, and performed E-field measurements in the phantom placed inside the SIGMA-Eye applicator.

Electromagnetic simulation experiments of the applicator within the phantom (Fig.6 (b)) working under different phase settings (Tab.5) were performed using the IDM with and without the mutual coupling, respectively. And the relative SAR distributions, which were rescaled to the maximum SAR values of the displayed planes, were compared between the measurement and the simulation.

Tab.5: Phase settings of the SIGMA-Eye applicator

Setting	anterior-posterior-channel phase lag	left-right-channel phase lag	three-dipole-ring phase lag
Setting 1	40,40	0,0	0,0,0
Setting 2	40,40	0,0	0,120,0
Setting 3	40,40	0,0	-30,0,30

3.3.1 The IDM with Mutual Coupling

The applicator was approximated by the superposition of the 24 antennas whose equivalent models were based on the basic building blocks from the part “Equivalent Dipole Models of the Blocks”.

Fig.10-15 show relative SAR iso-contours of the middle anterior-posterior section and the middle left-right section of the phantom, respectively from the three experiments. Different phase settings led to different SAR patterns. It is told from the images that SAR distributions are approximately elliptical. Fig.10-11 show a central focus created within the phantom, thus the SAR pattern is approximately longitudinally symmetrical. Relative anterior-posterior surface SAR levels are approximately 60% of the SAR in the center of the phantom. Compared to Fig.10-11, a longitudinally narrower relative SAR pattern is displayed on Fig.12-13. The 70% iso-contour is extended along the central anterior-posterior axis to encompass the full 18 cm phantom diameter. On Fig.14-15, the SAR pattern is not longitudinal symmetrical. And the center focus is obviously shifted closer to the bottom of the phantom.

Tab.6 illustrates the length and width of the ellipses of 70% iso-contours of SAR patterns, respectively from the simulations and from the measurements. The average SAR relative error was 5.07%.

Tab.6: Comparisons between the measurement data and the simulation data by the block-based IDM (operating frequency = 100 MHz)

Setting		Anterior-posterior section		Left-right section	
		Length(cm)	Width(cm)	Length(cm)	Width(cm)
Setting1	Measurement	17.0±0.5	10.0±0.5	17.0±0.5	10.0±0.5
	Simulation	17.59±0.2	9.67±0.2	17.59±0.2	11.41±0.2
	Relative error (%)	3.47	3.30	3.47	14.10
Setting 2	Measurement	10.5±0.5	Full	10.5±0.5	-(*)
	Simulation	11.02±0.2	Full	11.02±0.2	11.60±0.2
	Relative error (%)	4.95	-	4.95	-
Setting 3	Measurement	16.5±0.5	10.0±0.5	16.5±0.5	12.0±0.5
	Simulation	17.60±0.2	9.86±0.2	17.60±0.2	11.79±0.2
	Relative error (%)	6.67	1.40	6.67	1.75

* This value is not given in the document^[92].

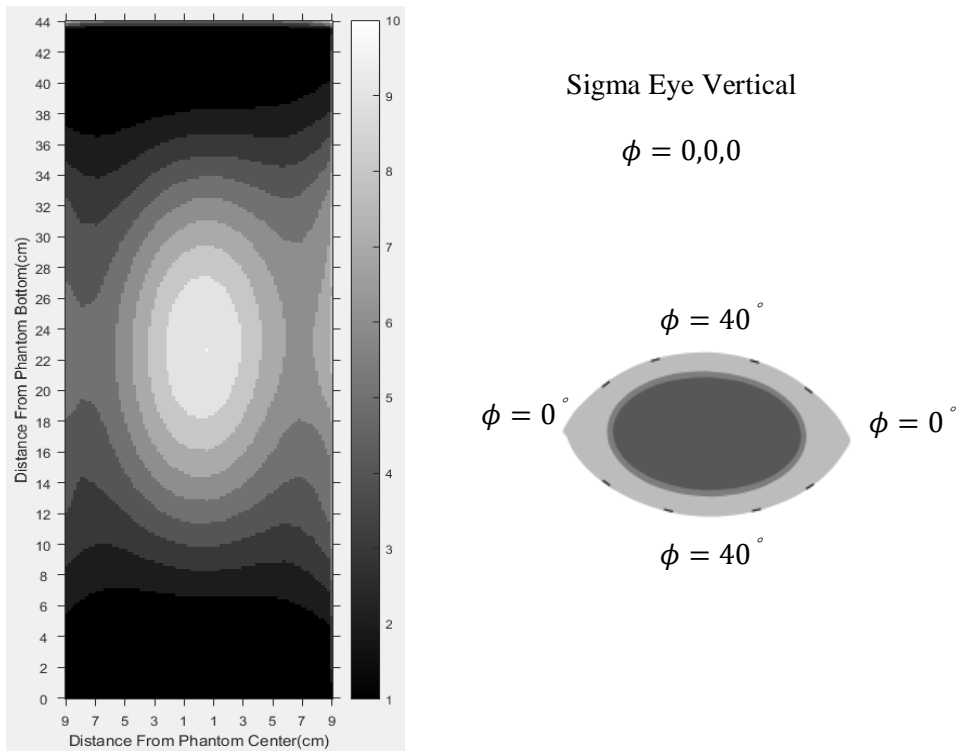


Fig.10: Anterior-posterior section of the relative iso-contour of SAR distribution under phase setting 1, using the method of basic-building-block-based IDM (operating frequency = 100 MHz)

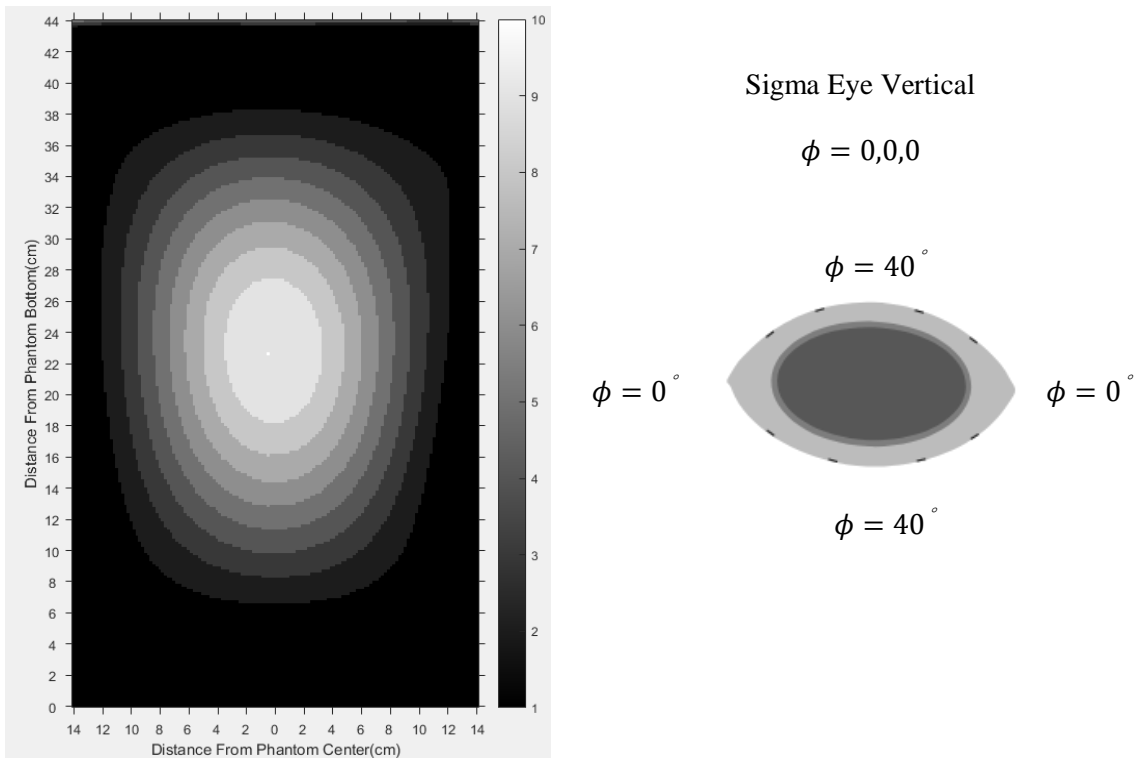


Fig.11: Left-right section of the relative iso-contour of SAR distribution under phase setting 1, using the method of basic-building-block-based IDM (operating frequency = 100 MHz)

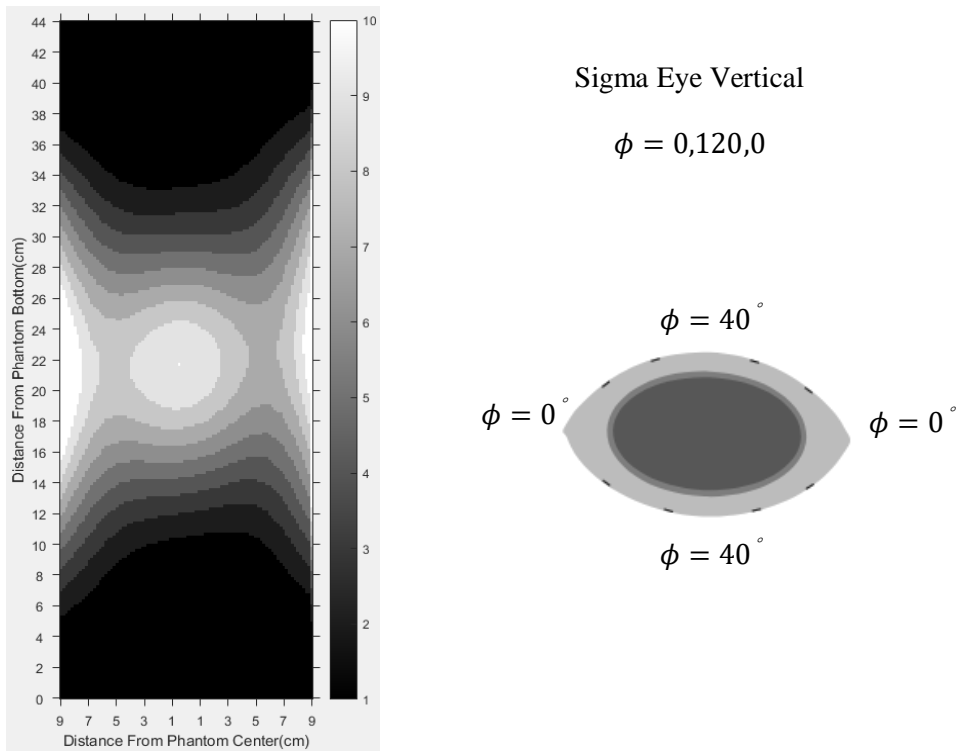


Fig.12: Anterior-posterior section of the relative iso-contour of SAR distribution under phase setting 2, using the method of basic-building-block-based IDM (operating frequency = 100 MHz)

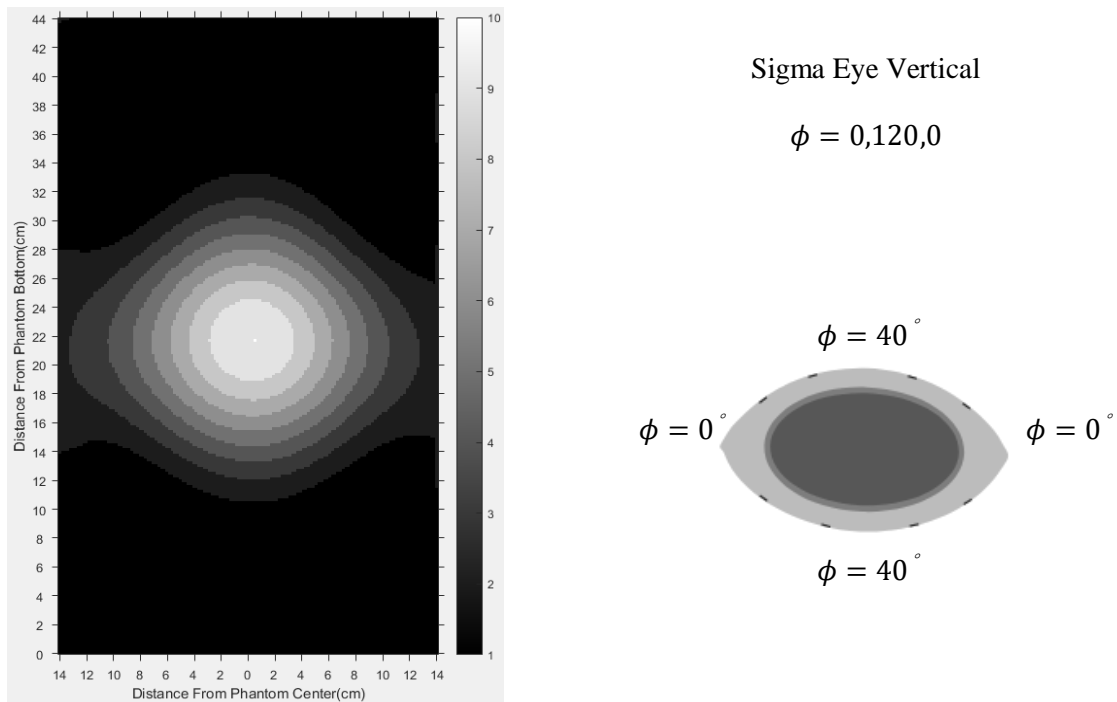


Fig.13: Left-right section of the relative iso-contour of SAR distribution under phase setting 2, using the method of basic-building-block-based IDM (operating frequency = 100 MHz)

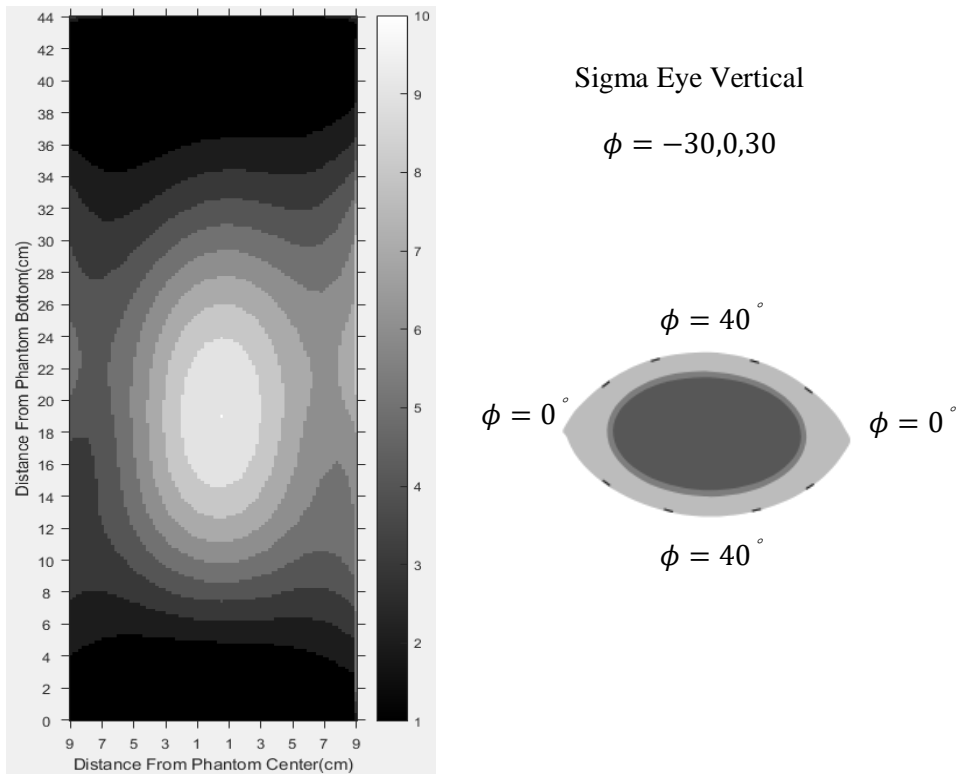


Fig.14: Anterior-posterior section of the relative iso-contour of SAR distribution under phase setting 3, using the method of basic-building-block-based IDM (operating frequency = 100 MHz)

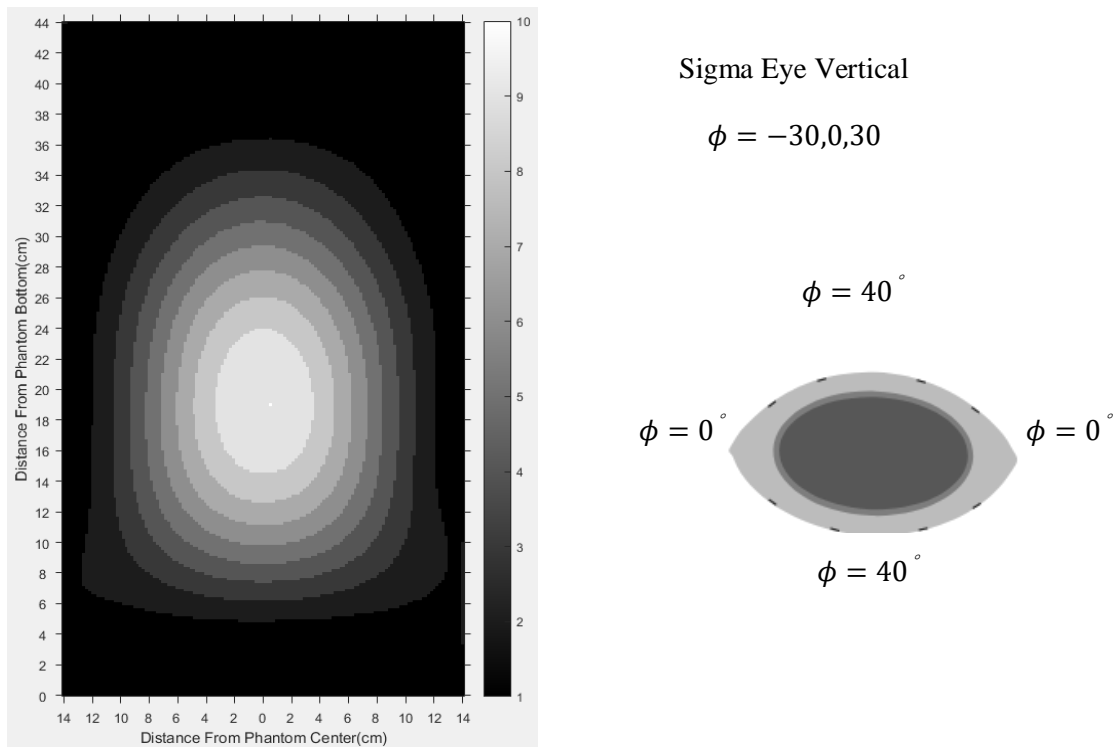


Fig.15: Left-right section of the relative iso-contour of SAR distribution under phase setting 3, using the method of basic-building-block-based IDM (operating frequency = 100 MHz)

3.3.2 The IDM of the Single Isolated AUT

The applicator was approximated by the superposition of the 24 antennas whose equivalent models were based on the single isolated antenna from the part “Equivalent Dipole Models of the Single Isolated Antenna”.

The relative SAR distributions simulated using the IDM without considering the mutual coupling are displayed in Fig.16-21. Tab.7 illustrates the length and width of the ellipses of 70% iso-contours of SAR patterns, respectively from the simulations without mutual coupling and from the measurements. The average SAR relative error was 25.31%.

Tab.7: Comparisons between the measurement data and the simulation data by the single isolated AUT (operating frequency = 100 MHz)

Setting	Anterior-posterior section		Left-right section		
		Length(cm)	Width(cm)	Length(cm)	Width(cm)
1	Measurement	17.0±0.5	10.0±0.5	17.0±0.5	10.0±0.5
	Simulation	23.98±0.2	7.54±0.2	23.98±0.2	14.70±0.2
	Relative error (%)	41.06	24.60	41.06	47.00
2	Measurement	10.5±0.5	Full	10.5±0.5	-(*)
	Simulation	9.08±0.2	8.31	9.08±0.2	15.47±0.2
	Relative error (%)	14.13	-	14.13	-
3	Measurement	16.5±0.5	10.0±0.5	16.5±0.5	12.0±0.5
	Simulation	18.37±0.2	7.34±0.2	18.37±0.2	14.50±0.2
	Relative error (%)	11.33	27.60	11.33	20.83

* This value is not given in the document^[92].

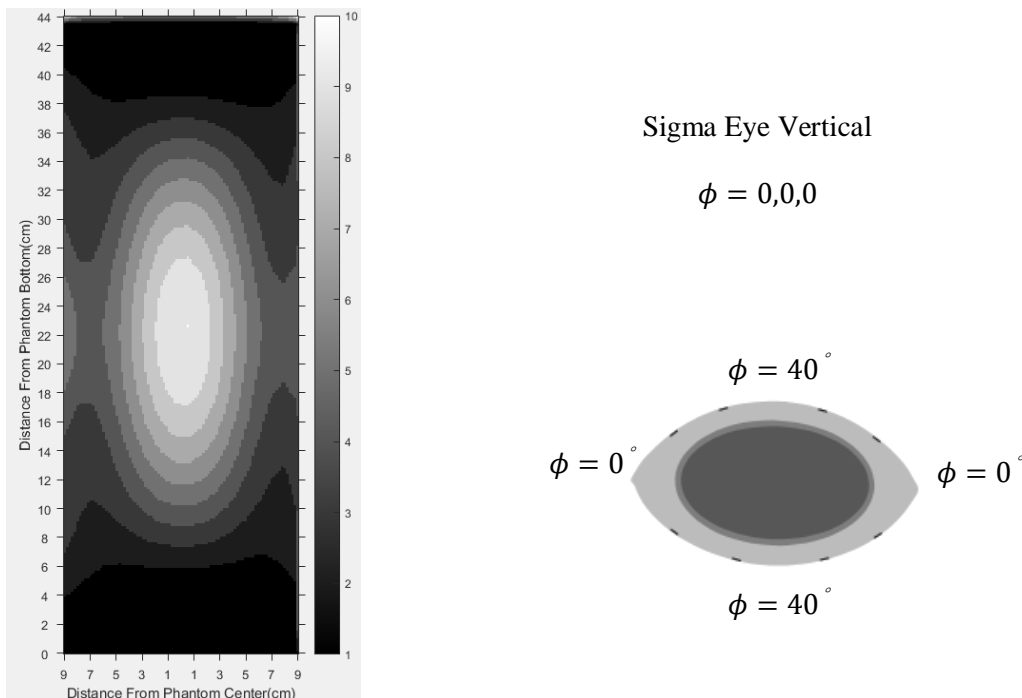


Fig.16: Anterior-posterior section of the relative iso-contour of SAR distribution under phase setting 1, using the IDM without mutual coupling (operating frequency = 100 MHz)

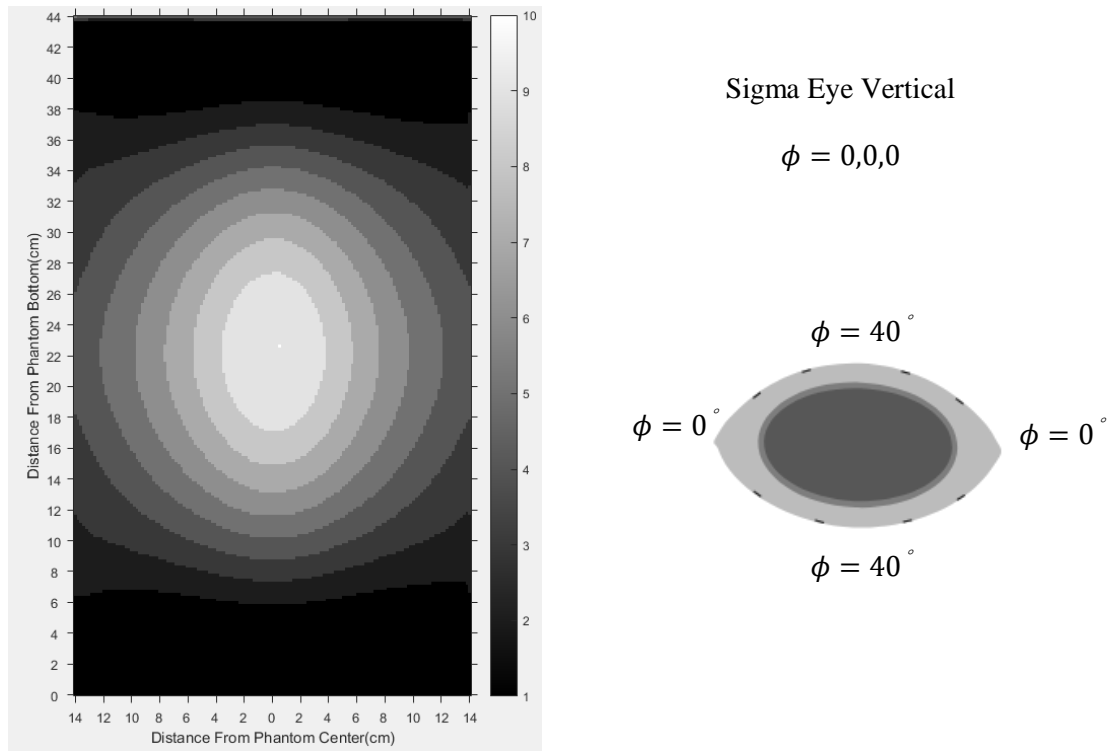


Fig.17 Left-right section of the relative iso-contour of SAR distribution under phase setting 1, using the IDM without mutual coupling (operating frequency = 100 MHz)

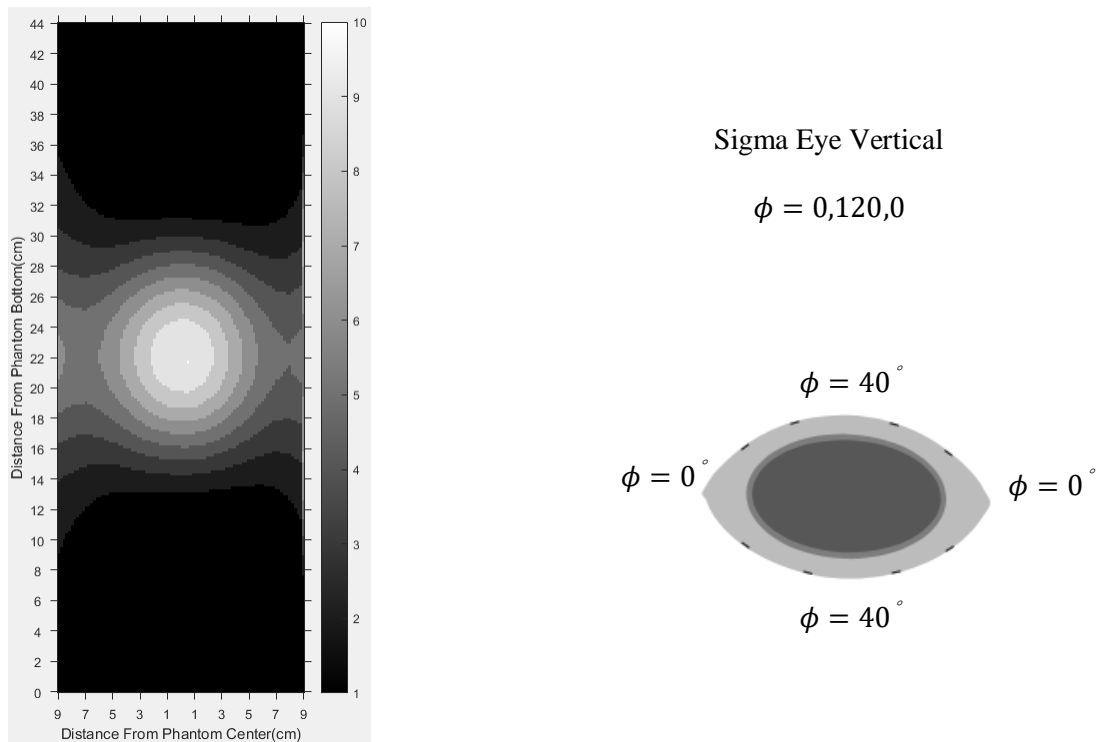


Fig.18: Anterior-posterior section of the relative iso-contour of SAR distribution under phase setting 2, using the IDM without mutual coupling (operating frequency = 100 MHz)

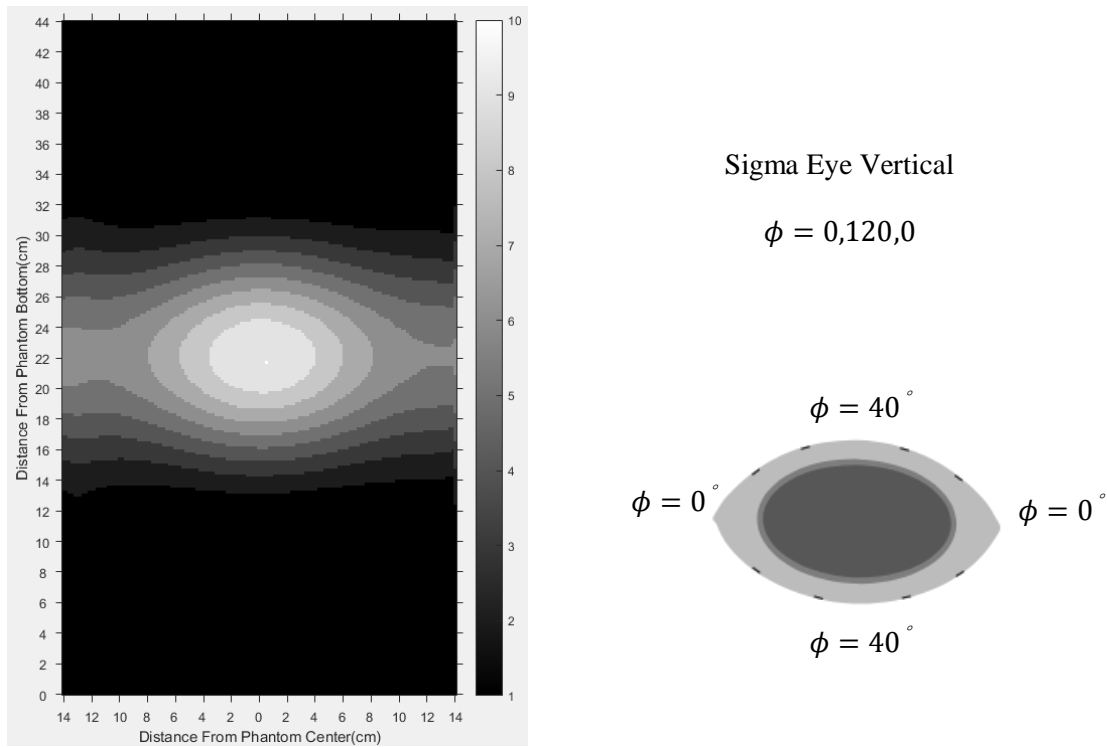


Fig.19: Left-right section of the relative iso-contour of SAR distribution under phase setting 2, using the IDM without mutual coupling (operating frequency = 100 MHz)

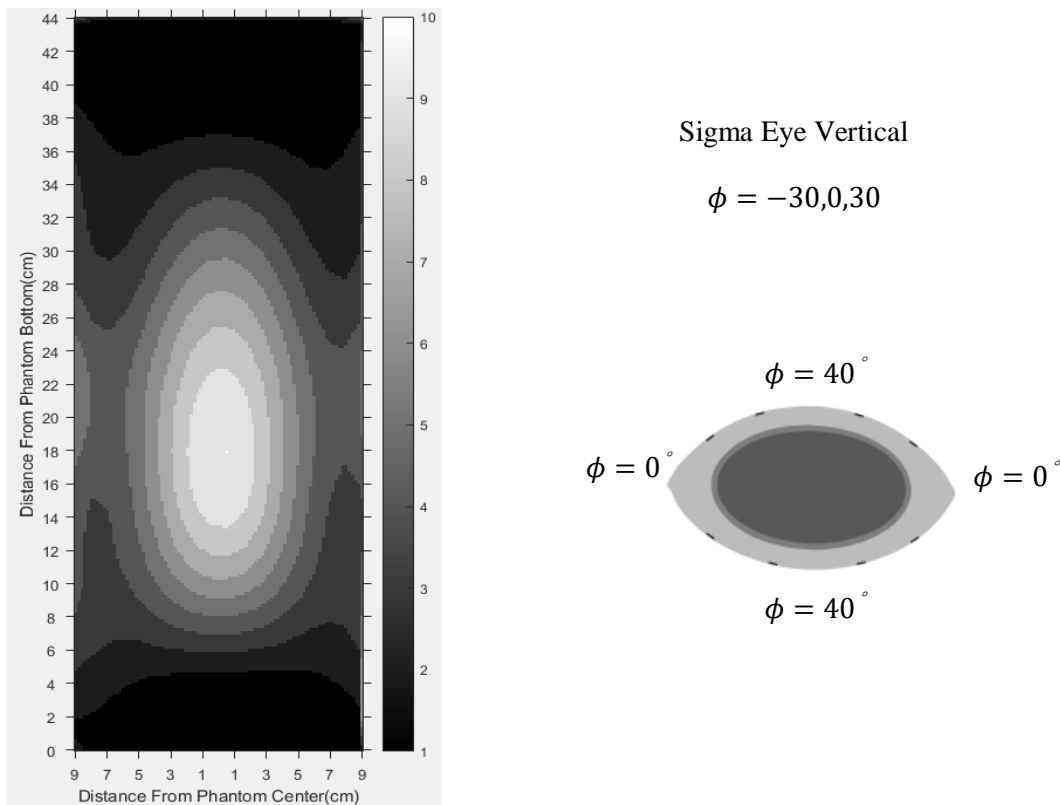


Fig.20: Anterior-posterior section of the relative iso-contour of SAR distribution under phase setting 3, using the IDM without mutual coupling (operating frequency = 100 MHz)

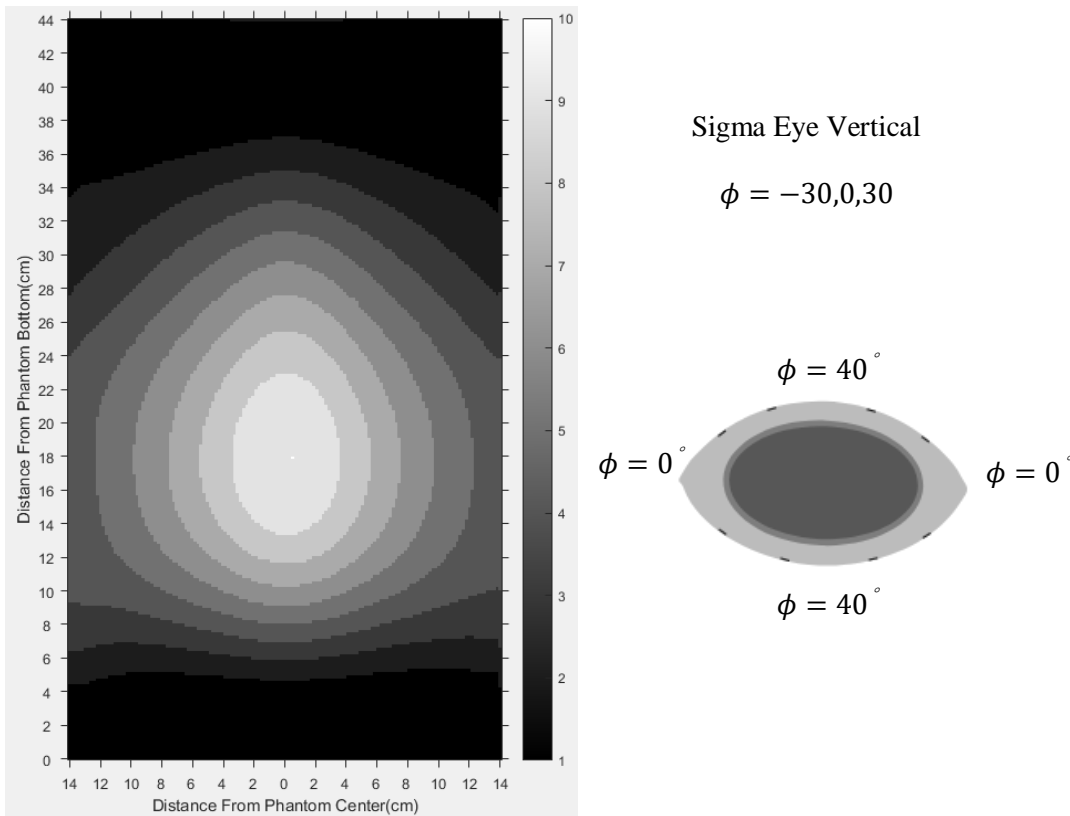


Fig.21: Left-right section of the relative iso-contour of SAR distribution under phase setting 3, using the IDM without mutual coupling (operating frequency = 100 MHz)

3.4 Frequency Analysis of the Basic-Building-Block-Based IDM

The previous experiments are based on one condition, that the operating frequency of the applicator or the ASU is a fixed frequency, 100 MHz in this work. Naturally, one question is proposed, whether the optimal equivalent series of dipoles is frequency dependent or not. In theory, the antenna current distribution is changing with the operating frequency. Therefore, it is expected that the optimal equivalent series of dipoles is a frequency-dependent function.

In this section, the frequency analysis of the block-based IDM is illustrated. The basic idea is to explore the applicability of the equivalent dipole model yielded at a reference frequency for other operating frequencies. The four typical blocks respectively of antenna 01, antenna 02, antenna 04 and antenna 05 were used.

Here is the specified experiment process taking block01 as an example.

- i) It was assumed that the reference frequency was 100 MHz, and the operating frequency was e.g. 105 MHz,
- ii) An equivalent dipole model for block01, which operated with the reference frequency, was obtained using the basic-building-block-based modified IDM, as described in the section 2.2.5 'Sigma-Eye Applicator Modeling'. It was to be stressed that the dipoles used here worked under the reference frequency.
- iii) Under the operating frequency, the dipole model with the optimal IDM weighting vector obtained in the last step produced a different electric field (named 'simulated' electric field) as in the last step. Here the dipoles worked under the operating frequency.
- iv) The 'standard' electric field of the block which worked under the operating frequency was still simulated by COMSOL.

v) The relative difference between the ‘simulated’ and ‘standard’ electric fields was calculated to explore the permittivity dependence of the dipole model.

Tab.8 illustrates the relative differences of the four typical blocks between the reference field and the ‘simulated’ field with the operating frequencies ranging from 90 MHz to 110 MHz. To make the frequency-dependence clearer, the changing tendencies of the relative differences are plotted in Fig.22. Fig-Appendix.5-Fig-Appendix.7 display the comparisons between the ‘standard’ field generated in COMSOL and the ‘simulated’ field with the reference frequency of 100 MHz for the four typical blocks operated at 110 MHz along the central axes of the phantom. Fig-Appendix.8-Fig-Appendix.10 are for the operating frequency of 105 MHz, Fig-Appendix.11-Fig-Appendix.13 for 103 MHz, Fig-Appendix.14-Fig-Appendix.16 for 98 MHz, Fig-Appendix.17-Fig-Appendix.19 for 95 MHz, and Fig-Appendix.20-Fig-Appendix.22 for 90 MHz.

As shown in Tab.8, when the operating frequency is 103 MHz or 98 MHz, the relative difference ranges from 4% to 9%, which shows good agreement between the ‘standard’ fields and the ‘simulated’ fields. However, the more deviated the operating frequency from the reference frequency, the larger the relative differences. With the operating frequency of 105 MHz or 95 MHz, the relative difference is around 11%. With the operating frequency of 110 MHz or 90 MHz, the relative difference is around 20%. Therefore it is concluded that the applicable frequency range of the block-based IDM is limited to a small range. Here, the equivalent model of 100 MHz works perfectly at frequencies of 100 ± 3 MHz, still acceptable at frequencies of 100 ± 5 MHz, but not acceptable at further frequencies. For further frequencies, new IDMs need to be created.

Tab.8: Frequency dependencies of the IDM (the reference frequency = 100 MHz)

	Frequency(MHz)	90	95	98	103	105	110
Relative difference (%)	Antenna01-block	19.13	10.93	6.76	7.93	10.07	14.91
	Antenna02-block	18.97	11.73	6.99	8.47	11.15	15.68
	Antenna04-block	14.94	8.54	6.53	9.87	12.36	19.04
	Antenna05-block	9.91	6.24	4.58	9.27	12.86	22.33

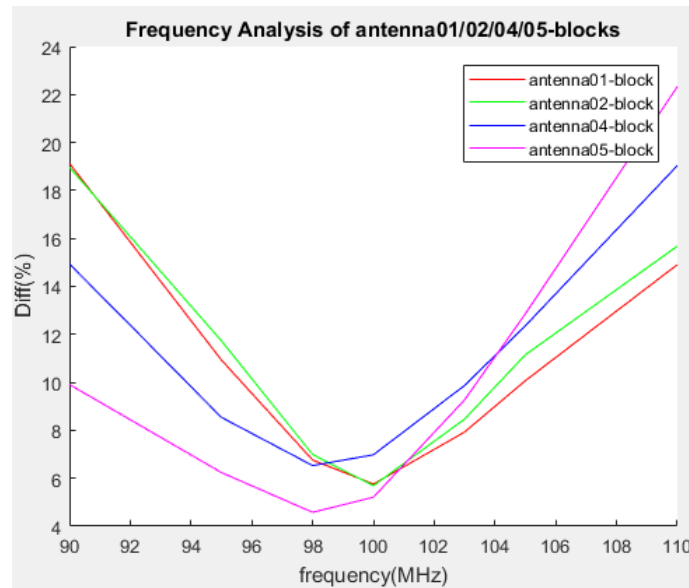


Fig.22: Frequency dependencies of the antenna01/02/04/05-block (the reference frequency = 100 MHz)

3.5 Permittivity-Dependence Analysis of the Basic-Building-Block-Based IDM

As mentioned before, in the basic-building-block-based modified IDM, mutual coupling between antenna elements are considered as multiple scattering effect. Naturally, this scattering effect is influenced by the non-free space environment, which is surrounding the antennas. In addition, strong mutual coupling between antennas induces a current distortion, which refers to the difference between antenna current distributions with and without coupling. ^[93] The non-free space environment also influence the current distortion significantly, thus has an effect on the antenna performances.

When used in clinic, the antennas of the Sigma-Eye applicator are located in a relative stable environment, which is the water bolus. Even so, it cannot be guaranteed that the environment is constant without inducing any differences in the scattering effect or even in the current distribution of antennas. There exist several factors which influence the electric properties of the water bolus intra- and inter-treatments, e.g. operating frequency of the applicator, water temperature, air pressure and so on. Also, the theoretical electric property data used in the IDM is not perfectly agreed with the real data because of measurement deviation. It is found that there is a 4% accumulated uncertainty of water-bolus permittivity in average based on different published data and related reviews ^[94-96].

Similar to the frequency dependence analysis, the idea is to explore the applicability of the equivalent dipole model yielded at a 'measured' permittivity of water bolus for other 'real' permittivity values, which is deviated from the measured one. The four typical blocks respectively of antenna 01, antenna 02, antenna 04 and antenna 05 were used.

Here is the specified experiment process taking block01 as an example.

- vi) It was assumed that the 'measured' relative permittivity of water bolus was 78, and the 'real' value was e.g. 75,
- vii) An equivalent dipole model for block01 was obtained using the basic-building-block-based modified IDM, as described in the section 2.2.5 'Sigma-Eye Applicator Modeling'. To be stressed here, in the optimization, the dipoles worked with the 'measured' relative permittivity of water-bolus that was 78.

- viii) In 'reality', where all dipoles worked with the 'real' relative permittivity, the dipole model with the optimal IDM weighting vector obtained in the last step produced a different electric field (named 'simulated' electric field) as in the last step.
- ix) The 'standard' electric field of the block which worked with the 'real' permittivity was still simulated by COMSOL.

The relative difference between the 'simulated' and 'standard' electric fields was calculated to explore the permittivity dependence of the dipole model.

Tab.9 illustrates the relative differences changing with the deviation of the 'measured' permittivity to a set of 'real' permittivity for the four typical blocks. To be on the safe side, the permittivity dependence of the block-based modified IDM will be analyzed in the uncertainty range of water-bolus permittivity of 10%. To make the permittivity-dependence clearer, the changing tendencies of the relative differences are plotted in Fig.23. Fig-Appendix.23-Fig-Appendix.25 display the comparisons between the 'standard' field and the 'simulated' fields of the four typical blocks with the 'real' relative permittivity of 70 along the central axes of the phantom. Fig-Appendix.26-Fig-Appendix.28 are for the 'real' relative permittivity of 75, Fig-Appendix.29-Fig-Appendix.31 for 81, Fig-Appendix.32-Fig-Appendix.34 for 85.

As shown in Tab.9, within 4% deviation of the 'measured' permittivity from the 'real' permittivity, the relative difference ranges from 6.63% to 8.49%, which is in the same error level as the equivalent dipole model of the 'measured' permittivity, and shows good agreement between the 'measured' and 'simulated' electric fields. It is concluded that the approach, basic-building-block-based modified IDM is capable of adapting to the uncertainty of the permittivity of water bolus caused by measurement methods, temperature and so on. However, on the other side, the more deviated the 'measured' permittivity from the 'real' permittivity, the larger the relative differences ranging from 6.50% to 13.48%. The larger differences, when the environment changes a lot, also imply that the dipole model needs to be updated based on the surrounding environment.

Tab.9: Permittivity-dependence analysis with 'measured' relative permittivity of 78

		'Measured'	70	75	81	85
		relative permittivity				
		Deviation percent	10%	4%	4%	9%
Relative difference (%)		Antenna01-block	12.51	6.83	6.99	9.63
		Antenna02-block	13.48	7.06	7.33	10.74
		Antenna04-block	9.32	6.63	8.49	11.31
		Antenna05-block	6.50	8.49	7.33	11.33

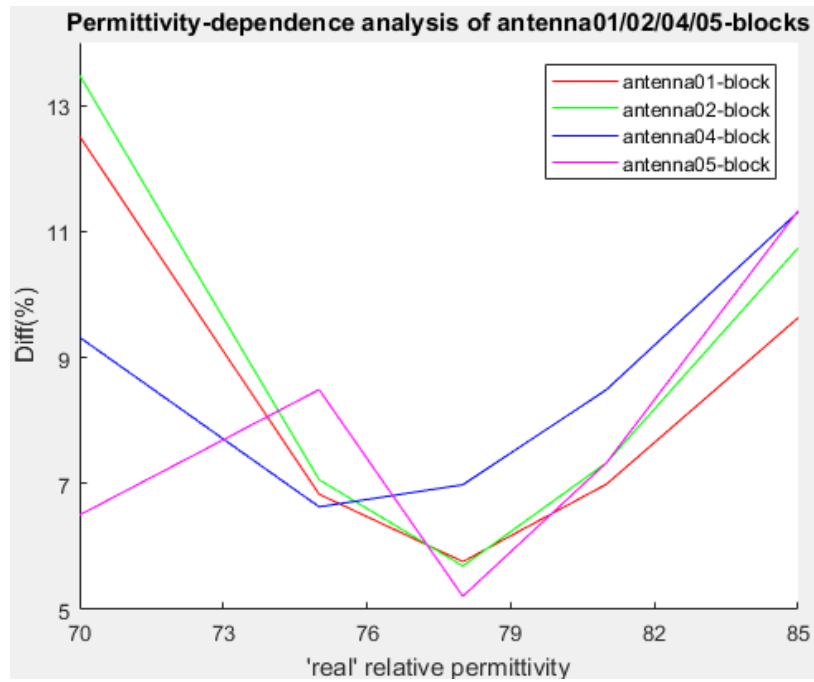


Fig.23: Water-bolus permittivity dependencies of the antenna01/02/04/05-block (the 'measured' relative permittivity = 98)

3.6 Conductivity-Dependence Analysis of the Basic-Building-Block-Based IDM

Similar to the water-bolus permittivity dependence, the other electric properties of water bolus, conductivity will also have an effect on antenna current distribution and mutual coupling effect, thus on electric field pattern. In theory, the conductivity of pure water changes with temperature, pressure and electromagnetic field frequency. At 25°C, for ultra-pure water, the typical conductivity is about 5.5×10^{-6} S/m.^[97] For drinking water, because of salinity, it is increased to around 0.005 S/m.^[97] The uncertainty of conductivity measurement at 25°C is around 0.25%.^[98] In theory, at such a low frequency, such as 100 MHz in this work, the water conductivity is assumed to be 0 S/m.

In this work, to explore the water-bolus conductivity dependence of the equivalent dipole model, the 'measured' conductivity of water bolus was assumed to be 0 S/m, and the 'real' conductivity was started from 0.005 S/m, and up to 0.05 S/m. The water-bolus conductivity dependence was analysed using the four typical blocks. The relative differences were illustrated in Tab.10. To make the conductivity-dependence clearer, the changing tendencies of the relative differences are plotted in Fig.24. Fig-Appendix.35-Fig-Appendix.37 display the comparisons between the 'standard' field and the 'simulated' fields of the four typical blocks with the 'real' conductivity of 0.005 S/m along the central axes of the phantom. Fig-Appendix.38-Fig-Appendix.40 are for the 'real' conductivity of 0.01 S/m, Fig-Appendix.41-Fig-Appendix.43 for 0.05 S/m.

As shown in Tab.10, at the drinking water conductivity of 0.005 S/m, the relative difference ranges from 5.46% to 7.10%, which indicates good agreement between the 'simulated' and 'standard' electric fields. And even when the conductivity goes up to 0.01 S/m, the relative difference is still very small. However, when the 'measured' conductivity is 0.05 S/m, the relative differences increase to around 17%, and this implies that the dipole model needs to be updated at this moment.

Tab.10: Conductivity-dependence analysis with 'measured' conductivity of 0 S/m

Relative difference (%)	'Measured' Conductivity(S/m)	0.005	0.01	0.05
	Antenna01-block		5.97	6.73
Antenna02-block		5.69	6.31	17.17
Antenna04-block		7.10	7.73	18.40
Antenna05-block		5.46	6.27	17.41

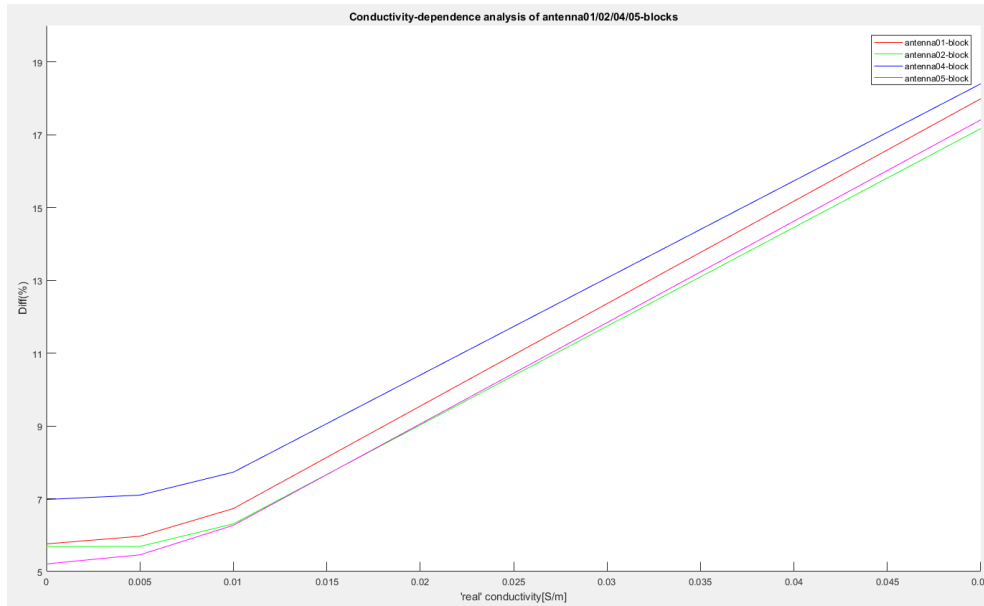


Fig.24: Water-bolus permittivity dependencies of the antenna01/02/04/05-block (the 'measured' conductivity = 0 S/m)

4 DISCUSSION

A new EM simulation method for HTP, which combined the basic-building-block-based modified IDM with the OQNLP optimization, was presented in this work.

The only required information for the IDM is the volume size of the AUT which is roughly the same as the physical volume occupied by the AUT, but need not be exactly identical, no matter how complex the geometry of the AUT is (the near field measurement is anyway necessary for all antenna modeling methods). In contrast, a geometric model of an AUT, which matches the geometry of each antenna^[56], needs a geometry data fitting for each component of the AUT due to small manufacturing errors. Therefore, the IDM is a good choice to reduce the cost of geometry fitting, especially when the geometry is very complicated.

The objective function values of the block-based modified IDM in this work are in good agreement with the errors ranged from 2-8% as reported by ^[63, 70, 99, 100].

Compared to the conventional IDM ^[63, 70, 99, 100], the main update of the modified IDM is the usage of fixed-number and fixed-position dipoles. Firstly, it reduces the dimension of the IDM weighting vector, and thus simplifies the optimization problem. Secondly, with equations (2.3-9-1), (2.3-9-2) and (2.3-9-3), the electric field of the IMD during the optimization progress can be updated fast and easily, without repeatedly using Green's Function^[60]. Since equations (2.3-9-1) to (2.3-9-3) are simpler than Green's Function, the error function is simplified to a much easier equation, which significantly reduces the complexity of the objective function of optimization problem.

However, the fixation of the number and position of dipoles also limits the flexibility of the modified IDM to a certain degree, which is at the expense of more dipoles needed in the modified IDM in comparison with the conventional IDM consisting of movable dipoles^[101].

One limitation of the current modified IDM is that, the weighting parameters of each dipole in the IDM are constants independent on frequencies, which makes this model only work for a narrow frequency band, as shown in the section 'Frequency Analysis'. For exciting frequencies outside the narrow frequency band, the IDM simulation should be performed again with new near field measurement data to obtain new weighting data. In the hyperthermia treatment, different exciting frequencies ranged from 100 MHz to 200 MHz or even higher^[63] are used to fulfill various treatment requirements. To better adapt to this wide frequency problem, frequency dependent dipole models^[101] need to be developed.

Similarly, from the analysis of water-bolus permittivity and conductivity dependence, it is known that the block-based modified IDM is dependent on the surrounding environment of the antennas of the applicator to some extent. However, in the clinical practice, the environment is water bolus, which is relatively constant. The analysis has proved the adaptability of the approach to the uncertainty of the electric properties (permittivity and conductivity) of water bolus. Therefore, the approach is applicable in clinical hyperthermia treatment planning.

When it comes to the simulation of the antenna-array applicator, as shown in the section 'Comparison with the measurement', the block-based modified IDM which took mutual coupling into consideration yielded electromagnetic fields in better agreement with the measurement data, compared to the modified IDM, which did not take mutual coupling into consideration. This proves necessity to take the mutual

coupling into account, and also proves the applicability of the block-based IDM in the mutual effect computation.

The question posed naturally now is whether it is possible to consider the entire applicator as a single large AUT, which will naturally account for the interaction inside the applicator. However, it is not practical for the following reasons.

The number of dipoles used for the simulation of the entire applicator, and hence the dimensionality of the optimization problem, becomes very large. For example, there are 24 antennas in the SIGMA-Eye applicator. If 10 dipoles are used for each antenna, then the number of dipoles for the entire applicator is $10 * 24 = 240$, which results in an optimization problem with $240 * 4 = 960$ unknowns, an extremely large size to work with in a global optimization problem.

Even if the previous computational demands were met, the dipole model obtained for the entire applicator is valid only for fixed-phase-and-amplitude applicators. If the phases or amplitudes of one or some of the antenna elements are changed, it would take much more time and computational cost to re-solve Maxwell's Equations. Therefore, it is more efficient and convenient to simulate each antenna separately instead of the entire applicator, and then to calculate the electromagnetic field of the entire applicator by the superposition of the fields of each antenna element when the phases and amplitudes of antennas are tuned in order to focus energy on the target tissue in hyperthermia treatment planning.

To take the mutual coupling effect into account, the basic-building-block-based IDM was chosen for its computational simplicity and conceptual clarity. It is not necessary to change the basic work frame of the conventional IDM to implement this approach. In addition, by building a library of dipole models corresponding to the various antennas with various coupling environment, it is possible to predict the field for arbitrary combinations of the antennas.

In contrast, another approach of mutual coupling calculation using the reaction theorem^[60, 61, 100], whereby a closed form expressing of mutual admittance is derived, is computationally more expensive. Moreover, the mutual coupling calculation method based on reaction theorem can only predict the mutual coupling as long as one antenna element is outside of the second antenna's observation box defined in the IDM.^[100]

As mentioned in the result section, the average relative error of SAR iso-contours within the phantom in the SIGMA-Eye applicator was 5.07%. One of the possible reasons is the intrinsic limit of the basic-building-block-based modified IDM. In the approach, one hypothesis is that the electromagnetic interaction between antenna elements in an applicator is solely due to the multiple scattering effects between the active element, that is the AUT and the nearby passive elements. Based on this hypothesis, the effect of the "passive" element which is indeed active in the applicator is ignored.

Another cause for the deviation is inherited from the referenced near field data used in the IDM. As mentioned before, the power supply and feed structure of the blocks were not modelled explicitly in COMSOL, instead a uniform voltage difference was applied to the feed point. Therefore, the influence of e.g. transforming networks was not taken into account. However, in practice, in multi-antenna applicators, e.g. the SIGMA-Eye applicator, which consists of 12 pairs of antennas, phases and amplitudes in the feed points of these antennas under certain conditions can significantly differ from the values selected at the multichannel amplifier (forward parameters), mainly due to coupling.^[102] Here the coupling refers to the interaction affected by the transforming networks between the generators and the feed points. In the SIGMA-Eye applicator, the influence of coupling channels on the phases and

voltages in the feed point of a particular antenna are largest for adjacent longitudinal channels. According to ^[102], the $\pm 10^\circ$ phase shift and $\pm 30\%$ voltage change were observed if the disturbed channel and disturbing channel were equally powered. When the disturbed channel is fed with much lower power than the disturbing channel, the changes could even reach -30° to 100° phase shift and -80% to 50% voltage change. This affect could be minimized by the simulation of the transforming networks or fitting the phases and amplitudes in the simulated uniform voltage sources to the ones in the feeding points in reality.

Various global optimization algorithms have been used in the IDM, like genetic algorithm^[99], Invasive Weed Optimization (IWO)^[61, 64], Quantum particle swarm optimization (QPSO)^[70] and so on, and they were proved to be valid in certain application areas. OQNLP was chosen to be used in this work is because of its flexibility and strong global search ability. For smooth problems, the advantage of a search method over a gradient-based optimization solver lies in its ability to locate an approximation to a good local solution which is near to the global optimum. Gradient-based optimization solvers usually converge to the 'nearest' local solution to the starting point, thus are trapped in a local optimum. However, compared to gradient-based optimization solvers, search methods are weak in limited accuracy. Gradient-based optimization is chosen because of its high speed of converging to a high accuracy. The combination of the scatter search method and a gradient-based local optimization solver is to take the advantages of the both to achieving a rapid convergence to a global optimum. There is no guarantee that the final solution is the global optimum, and no bound is provided on how far that solution is from the global optimum. However, the algorithm has been tested extensively on 135 problems from the set gathered by Chris Floudas et al.^[103] and the test results were presented by Lasdon et al. in ^[104]. According to Lasdon et al., OQNLP found the best known solutions on all the 135 problems but three of them using default parameters and options within one or two calls of the local solver. Moreover, by combination with different kinds of local solvers, OQNLP can be adapted to different kinds of problems. It is very flexible, since each of its elements can be implemented in a variety of ways and degrees of sophistication

5 CONCLUSION

In this work, the basic-building-block based modified IDM was applied to model the SIGMA-Eye applicator for the EM simulation in EM-HTP.

Firstly, a modified IDM was proposed on the basis of the conventional IDM theory. By pre-defining the position and number of the dipoles, the dimension of the IDM weighting parameter was decreased by 3*the number of the dipoles, and the objective function was simplified, which resulted in less computational cost compared to the conventional IDM.

In addition, the concept of basic building block for the AUT was introduced, whereby the mutual coupling between nearby antenna elements in the applicator is interpreted as multiple scattering effects. The block-based IDM of the AUT takes the field data of the block as the reference field data, not of the AUT, and then OQNLP is applied to search for an equivalent dipole model for the AUT of the specified block. In this work, infinitesimal dipole models composed of different numbers of dipoles were explored, and the series of $1 \times 1 \times 12$ dipoles was chosen. The average optimal objective function value of the equivalent dipole models of the 24 basic building blocks reached 5.98%.

Within the above-mentioned optimal dipole series, the SIGMA-Eye applicator was simulated by the superposition of the 24 antennas. Three experiments with different phase settings were performed, and the resulted relative SAR patterns were compared to the measurement^[92]. An average relative SAR error of 5.07% was achieved, which validated the applicability of the IDM in EM-HTP.

Moreover, the frequency dependence and water-bolus permittivity and conductivity dependence of the block-based modified IDM was explored, and it was found that this approach is only applicable for a narrow-band frequency, and is adaptable to the uncertainty of the water-bolus permittivity and conductivity. When operating at a frequency further away from the reference frequency, or the surrounding environment of the antennas changes a lot, the applicator needs to be simulated using a new equivalent model.

As mentioned in the discussion section, the interaction caused by the transforming networks between the generators and the feed points has a significant influence in the electric field distribution, therefore it is necessary to introduce the transforming network simulation or fitting into the electromagnetic simulation in the future work. Also, it is considered to utilize ultra-wide-frequency-band IDM, e.g. using frequency-dependent weighting parameters in the objective function. In the current work, the electromagnetic simulation was performed using a homogeneous phantom. Like every other computational simulation of the other medical applications, the next step should go to inhomogeneous phantom, and then real patient anatomical geometries.

6 REFERENCES

- [1] Siegel, R., et al., *Cancer statistics, 2014*. CA Cancer J Clin, 2014. **64**(1): p. 9-29.
- [2] Institute, N.C. *Hyperthermia in cancer treatment*. 2018 7 Apr. 2018]; Available from: <https://www.cancer.gov/about-cancer/treatment/types/surgery/hyperthermia-fact-sheet>
- [3] van der Zee, J., *Heating the patient: a promising approach?* Ann Oncol, 2002. **13**(8): p. 1173-84.
- [4] McGhana, J.P. and G.D. Dodd, 3rd, *Radiofrequency ablation of the liver: current status*. AJR Am J Roentgenol, 2001. **176**(1): p. 3-16.
- [5] Sterzer, F., *Microwave medical devices*. IEEE Microwave Magazine, 2002. **3**(1): p. 65-70.
- [6] Orth, K., et al., *Thermo-controlled device for inducing deep coagulation in the liver with the Nd:YAG laser*. Lasers in Surgery and Medicine, 1997. **20**(2): p. 149-156.
- [7] Curiel, L., et al., *1.5-D high intensity focused ultrasound array for non-invasive prostate cancer surgery*. IEEE Transactions on Ultrasonics Ferroelectrics and Frequency Control, 2002. **49**(2): p. 231-242.
- [8] Moros, E., *Physics of thermal therapy : fundamentals and clinical applications*. Imaging in medical diagnosis and therapy. 2013, Boca Raton, FL: CRC/Taylor & Francis. xvi, 359 p.
- [9] Kaur, P., et al., *Combined hyperthermia and radiotherapy for the treatment of cancer*. Cancers (Basel), 2011. **3**(4): p. 3799-823.
- [10] Hager, D., *Hyperthermia In cancer treatment*. whole body hyperthermia at 43.5-44°C: dreams or reality?, ed. A.V. Suvernev. 2006: Springer.
- [11] Rao, W., Z.S. Deng, and J. Liu, *A review of hyperthermia combined with radiotherapy/chemotherapy on malignant tumors*. Crit Rev Biomed Eng, 2010. **38**(1): p. 101-16.
- [12] Kong, G., et al., *Efficacy of liposomes and hyperthermia in a human tumor xenograft model: importance of triggered drug release*. Cancer Res, 2000. **60**(24): p. 6950-7.
- [13] Dikomey, E. and J. Franzke, *Effect of heat on induction and repair of DNA strand breaks in X-irradiated CHO cells*. Int J Radiat Biol, 1992. **61**(2): p. 221-33.
- [14] Wust, P., et al., *Hyperthermia in combined treatment of cancer*. Lancet Oncol, 2002. **3**(8): p. 487-97.
- [15] Peschke, P., et al., *Improved therapeutic response by distinct timing of multiple heat treatments during interstitial radiation in the Dunning R3327 prostate tumor model*. J Cancer Res Clin Oncol, 1998. **124**(3-4): p. 172-8.
- [16] Arora, D., M. Skliar, and R.B. Roemer, *Minimum-time thermal dose control of thermal therapies*. IEEE Trans Biomed Eng, 2005. **52**(2): p. 191-200.
- [17] Thrall, D.E., et al., *Thermal dose is related to duration of local control in canine sarcomas treated with thermoradiotherapy*. Clinical Cancer Research, 2005. **11**(14): p. 5206-5214.
- [18] Song, C.W., et al., *Tumour oxygenation is increased by hyperthermia at mild temperatures*. International Journal of Hyperthermia, 1996. **12**(3): p. 367-373.

- [19] Manon, R., et al., *The impact of mid-treatment MRI on defining boost volumes in the radiation treatment of glioblastoma multiforme*. Technology in Cancer Research & Treatment, 2004. **3**(3): p. 303-307.
- [20] Larson, B., et al., *In vivo temperature mapping of prostate during treatment with TherMatrix TMx-2000 device: Heat field and MRI determinations of necrotic lesions*. Journal of Endourology, 2005. **19**(8): p. 1021-1025.
- [21] Viglianti, B.L., et al., *Dynamic contrast-enhanced magnetic resonance imaging as a predictor of clinical outcome in canine spontaneous soft tissue sarcomas treated with thermoradiotherapy (vol 15, pg 4993, 2009)*. Clinical Cancer Research, 2009. **15**(17): p. 5601-5601.
- [22] Giustini, A.J., et al., *Magnetic nanoparticle hyperthermia in cancer treatment*. Nano Life, 2010. **1**(1n02).
- [23] Botstein, R.W.P.F.S.J.M.E.F.C., *27 MHz waveguide applicators for localized hyperthermia treatment of cancer*. IEEE MTT-S International, 1981.
- [24] Croghan, M.K., et al., *A phase I study of the toxicity of regional hyperthermia with systemic warming*. Am J Clin Oncol, 1993. **16**(4): p. 354-8.
- [25] De Leeuw, A.A., J. Mooibroek, and J.J. Lagendijk, *Specific absorption rate steering by patient positioning in the 'Coaxial TEM' system: phantom investigation*. Int J Hyperthermia, 1991. **7**(4): p. 605-11.
- [26] Van Es, C., Wyrdean, H., De Leeuw, A., Mooibroek, J., Lagendijk, J. and Battermann, J., *Regional hyperthermia of pelvic tumors using the Utrecht 'Coaxial TEM' system*. International Journal of Hyperthermia, 1995. **11**(2): p. 173-186.
- [27] Van Vulpen, M., et al., *Comparison of intra-luminal versus intra-tumoural temperature measurements in patients with locally advanced prostate cancer treated with the coaxial TEM system: report of a feasibility study*. Int J Hyperthermia, 2003. **19**(5): p. 481-97.
- [28] Turner, P.F., *Regional hyperthermia with an annular phased array*. IEEE Trans Biomed Eng, 1984. **31**(1): p. 106-14.
- [29] Sapozink, M.D., et al., *Phase I evaluation of hyperthermia equipment--University of Utah institutional report*. Int J Hyperthermia, 1988. **4**(1): p. 117-32.
- [30] Paulsen, K.D., J.W. Strohbeh, and D.R. Lynch, *Theoretical temperature distributions produced by an annular phased array-type system in CT-based patient models*. Radiat Res, 1984. **100**(3): p. 536-52.
- [31] Strohbeh, J.W., et al., *Optimization of the absorbed power distribution for an annular phased-array hyperthermia system*. International Journal of Radiation Oncology Biology Physics, 1989. **16**(3): p. 589-599.
- [32] *BSD-2000 function and operations*. 2004, BSD Medical Corporation. p. 22-23.
- [33] Chou, C.K., et al., *Effects of fat thickness on heating patterns of the microwave applicator MA-151 at 631 and 915 MHz*. Int J Radiat Oncol Biol Phys, 1990. **19**(4): p. 1067-70.
- [34] Chan, K.W., J.A. McDougall, and C.K. Chou, *FDTD simulations of Clini-Therm applicators on inhomogeneous planar tissue models*. Int J Hyperthermia, 1995. **11**(6): p. 809-20.
- [35] Sherar, M.D., et al., *Beam shaping for microwave waveguide hyperthermia applicators*. Int J Radiat Oncol Biol Phys, 1993. **25**(5): p. 849-57.
- [36] Gopal, M.K., et al., *Current sheet applicator arrays for superficial hyperthermia of chestwall lesions*. Int J Hyperthermia, 1992. **8**(2): p. 227-40.

- [37] van Rhooen, G.C., P.J. Rietveld, and J. van der Zee, *A 433 MHz Lucite cone waveguide applicator for superficial hyperthermia*. *Int J Hyperthermia*, 1998. **14**(1): p. 13-27.
- [38] Stauffer, P., Jacobsen, S. and Neuman, D, *Microwave array applicator for radiometry-controlled superficial hyperthermia*. *Thermal Treatment of Tissue: Energy Delivery and Assessment*, 2001.
- [39] Seegenschmiedt, M., Bolomey, J., Brady, L., Burgman, P., Heilmann, H., Fessenden, P., Choi, I., Vernon, C., Crezee, J., Dahl, O., Dewhirst, M., Diederich, C., Felix, R., Hynynen, K., Kelleher, D., Konings, A., Lagendijk, J., Le Bihan, D., Lee, E., Li, G., Mizushima, S., Mooibroeck, J., Nadobny, J., Nah, B., Nussenzweig, A., Olmi, R., Osborn, J., Paulsen, K., Prescott, D., Roos, D., Sahu, S., Schneider, C., Seebass, M., Seegenschmiedt, M., Song, C., Stauffer, P., Streffer, C., Dijk, J., Roon, G., Vaupel, P., Vernon, C., Visser, A., Waterman, F. and Wust, P, *Thermoradiotherapy and thermochemotherapy*. 2013, Berlin: Springer
- [40] Handl-Zeller, L., *Interstitial hyperthermia*. 1992, Vienna: Springer Vienna.
- [41] DeFord, J.A., et al., *Effective estimation and computer control of minimum tumour temperature during conductive interstitial hyperthermia*. *Int J Hyperthermia*, 1991. **7**(3): p. 441-53.
- [42] Patel, U.H., J.A. DeFord, and C.F. Babbs, *Computer-aided design and evaluation of novel catheters for conductive interstitial hyperthermia*. *Med Biol Eng Comput*, 1991. **29**(1): p. 25-33.
- [43] Hulshof, M.C., et al., *A feasibility study of interstitial hyperthermia plus external beam radiotherapy in glioblastoma multiforme using the Multi ELECTrode Current Source (MECS) system*. *Int J Hyperthermia*, 2004. **20**(5): p. 451-63.
- [44] Canters, R.A., et al., *Optimizing deep hyperthermia treatments: are locations of patient pain complaints correlated with modelled SAR peak locations?* *Phys Med Biol*, 2011. **56**(2): p. 439-51.
- [45] Kok, H.P., et al., *Online adaptive hyperthermia treatment planning during locoregional heating to suppress treatment-limiting hot spots*. *Int J Radiat Oncol Biol Phys*, 2017. **99**(4): p. 1039-1047.
- [46] Paulides, M.M., et al., *Simulation techniques in hyperthermia treatment planning*. *Int J Hyperthermia*, 2013. **29**(4): p. 346-57.
- [47] Pennes, H.H., *Analysis of tissue and arterial blood temperatures in the resting human forearm*. *J Appl Physiol*, 1948. **1**(2): p. 93-122.
- [48] DETLEV STALLING, M.S., MALTE ZO"CKLER, HANS-CHRISTIAN HEGE. *Hyperthermia treatment planning with HyperPlan*. 2000; Available from: www.zib.de/hege/pdf/ZR-00-27.pdf.
- [49] de Bruijne, M., et al., *Benefits of superficial hyperthermia treatment planning: five case studies*. *Int J Hyperthermia*, 2007. **23**(5): p. 417-29.
- [50] Paulides, M.M., et al., *Winner of the "New Investigator Award" at the European Society of Hyperthermia Oncology Meeting 2007. The HYPERcollar: a novel applicator for hyperthermia in the head and neck*. *Int J Hyperthermia*, 2007. **23**(7): p. 567-76.
- [51] Albahyperthermia. *Hyperthermia Treatment Planning System (HTPS)*. 2018; Available from: <http://www.albahyperthermia.com/hyperthermia-treatment-planning-system.html>
- [52] Comsol.de. *COMSOL Multiphysics® Modellierung software*. 2018; Available from: <https://www.comsol.de>.
- [53] Ansys.com. *Engineering Simulation & 3-D Design Software | ANSYS*. 2018; Available from: <https://www.ansys.com/>.

- [54] Castillo, J.E., *Mathematical aspects of grid generation*. Society for Industrial and applied Mathematics, 1991.
- [55] Neal, M.L. and R. Kerckhoffs, *Current progress in patient-specific modeling*. Brief Bioinform, 2010. **11**(1): p. 111-26.
- [56] Wust, P., et al., *Electric field distributions in a phased-array applicator with 12 channels: measurements and numerical simulations*. Med Phys, 2000. **27**(11): p. 2565-79.
- [57] Y. T. Lo, D.S., and W. F. Richards, *Theoretical and experimental studies of microstrip antennas*, in *1978 URSI Meeting*. 1978: Washington. D. C.
- [58] Vicko Doriæ, D.P., John Paul, Christos Christopoulos, *Modeling of a straight thin wire: comparison of antenna approach and transmission line model*, in *2007 15th International Conference on Software, Telecommunications and Computer Networks*. 2007: Split-Dubrovnik, Croatia.
- [59] Symon K. Podilchak, P.B., Paolo Baccarelli, Al P. Freundorfer, Yahia M. M. Antar, *A circuits-based modeling approach for leaky-wave antennas using a transverse equivalent network representation*, in *2014 XXXIth URSI General Assembly and Scientific Symposium (URSI GASS)*. 2014: Beijing, China.
- [60] Mikki, S.M. and A.A. Kishk, *Theory and applications of infinitesimal dipole models for computational electromagnetics*. IEEE Transactions on Antennas and Propagation, 2007. **55**(5): p. 1325-1337.
- [61] Karimkashi, S., A.A. Kishk, and D. Kajfez, *Antenna array optimization using dipole models for MIMO applications*. IEEE Transactions on Antennas and Propagation, 2011. **59**(8): p. 3112-3116.
- [62] Karimkashi, S., Kishk, A., Kajfez, D. and Zhang, G, *Focusing properties of ultra wideband transient arrays*. Progress In Electromagnetics Research, 2013. **56**: p. 387-407.
- [63] Seebass, M., et al., *Electromagnetic phased arrays for regional hyperthermia: optimal frequency and antenna arrangement*. Int J Hyperthermia, 2001. **17**(4): p. 321-36.
- [64] Karimkashi, S., A.A. Kishk, and G. Zhang, *Modeling of aperiodic array antennas using infinitesimal dipoles*. Int Microwaves Antennas & Propagation, 2012. **6**(7): p. 761-767.
- [65] Carter, P.S., *Circuit relations in radiating systems and applications to antenna problems*. Proceedings of the Institute of Radio Engineers, 1932. **20**(6): p. 1004-1041.
- [66] Henault, S., Antar, Y., Rajan, S., Inkol, R. and Wang, S, *The multiple antenna induced EMF method for the precise calculation of the coupling matrix in a receiving antenna array*. Progress In Electromagnetics Research, 2009. **8**: p. 103-118.
- [67] Gupta, I.a.K., A, *Effect of mutual coupling on the performance of adaptive arrays*. IEEE Transactions on Antennas and Propagation, 1983. **31**(5): p. 785-791.
- [68] Hui, H.T., *Decoupling methods for the mutual coupling effect in antenna arrays: a review*. Recent Patents on Engineering, 2007. **1**(2): p. 187-193.
- [69] Henault, S., et al., *A methodology for mutual coupling estimation and compensation in antennas*. IEEE Transactions on Antennas and Propagation, 2013. **61**(3): p. 1119-1131.
- [70] Mikki, S.M. and Y.M.M. Antar, *Near-field analysis of electromagnetic interactions in antenna arrays through equivalent dipole models*. IEEE Transactions on Antennas and Propagation, 2012. **60**(3): p. 1381-1389.

- [71] Vendik, O.G. and D.S. Kozlov, *A novel method for the mutual coupling calculation between antenna array radiators analysis of the radiation pattern of a single radiator in the antenna array*. IEEE Antennas and Propagation Magazine, 2015. **57**(6): p. 16-21.
- [72] Wiersma, J. and J.D. Van Dijk, *RF hyperthermia array modeling; validation by means of measured EM-field distributions*. Int J Hyperthermia, 2001. **17**(1): p. 63-81.
- [73] Samaras, T., P.J.M. Rietveld, and G.C. van Rhoon, *Effectiveness of FDTD in predicting SAR distributions from the lucite cone applicator*. IEEE Transactions on Microwave Theory and Techniques, 2000. **48**(11): p. 2059-2063.
- [74] Jacobsen, S., H.O. Rolfsnes, and P.R. Stauffer, *Characteristics of microstrip muscle-loaded single-arm Archimedean spiral antennas as investigated by FDTD numerical computations*. IEEE Transactions on Biomedical Engineering, 2005. **52**(2): p. 321-330.
- [75] Wu, L.Y., et al., *An RF phased array applicator designed for hyperthermia breast cancer treatments*. Physics in Medicine and Biology, 2006. **51**(1): p. 1-20.
- [76] Gellermann, J., et al., *Comparison of MR-thermography and planning calculations in phantoms*. Medical Physics, 2006. **33**(10): p. 3912-3920.
- [77] B. Vrbová, L.V., *Simulation of hyperthermic treatment using the matrix of stripline applicators*. Journal of Advanced Engineering, 2010. **50**(4).
- [78] Chakaravarthi, G. and K. Arunachalam, *A compact microwave patch applicator for hyperthermia treatment of cancer*. Conf Proc IEEE Eng Med Biol Soc, 2014. **2014**: p. 5320-2.
- [79] Poggio, G.J.B.E.K.M.A.J., *The numerical electromagnetics code (NEC) - a brief history*. Antennas and Propagation Society International Symposium, 2004. IEEE, 2004.
- [80] Cardoso, J., *Electromagnetics through the finite element method*. 2017, Boca Raton: CRC Press, Taylor & Francis.
- [81] Sullivan, D., *Electromagnetic simulation using the FDTD method*. 2013, Hoboken: IEEE Press
- [82] Jones, D., *Field Computation by Moment Methods*. The Computer Journal, 1969. **12**(1): p. 37-37.
- [83] Yee, K., *Numerical solution of initial boundary value problems involving Maxwell's equations in isotropic media*. IEEE Transactions on Antennas and Propagation, 1966. **14**(3): p. 302–307.
- [84] Engquist, B. and A. Majda, *Absorbing boundary conditions for numerical simulation of waves*. Proc Natl Acad Sci U S A, 1977. **74**(5): p. 1765-6.
- [85] Berenger, J.P., *A perfectly matched layer for the absorption of electromagnetic-waves*. Journal of Computational Physics, 1994. **114**(2): p. 185-200.
- [86] Ugray, Z., Lasdon, L., Plummer, J., Glover, F., Kelly, J. and Martí, R, *Scatter Search and Local NLP Solvers: A multistart framework for global optimization*. INFORMS Journal on Computing, 2007. **19**(3): p. 328-340.
- [87] Foschini, G., *On limits of wireless communications in a fading environment when using multiple antennas*. Wireless Personal Communications, 1998. **6**: p. 311-355.
- [88] Glover, F., *A template for scatter search and path relinking*. Artificial Evolution, 1998. **1363**: p. 3-51.

- [89] Byrd, R.H., J.C. Gilbert, and J. Nocedal, *A trust region method based on interior point techniques for nonlinear programming*. Mathematical Programming, 2000. **89**(1): p. 149-185.
- [90] *MEEP Documentation*. 2017; Available from: <https://meep.readthedocs.io/en/latest/>
- [91] Wilkens, D. *BSD-2000 3D microwave hyperthermia system*. 2018; Available from: <https://www.pyrexar.com/hyperthermia/bsd-2000-3d>.
- [92] F.Turner, P., *Technical aspect of the BSD-2000 and BSD-2000-3D*, in *European Society for Hyperthermia Oncology and BSD Medical Corporation User's Conference*. 1997.
- [93] Qi, H.Y., et al., *A current distortion parameter for characterizing coupling of antennas*. Journal of Electromagnetic Waves and Applications, 2015. **29**(9): p. 1157-1173.
- [94] Gabriel, C., *Compilation of the dielectric properties of body tissues at RF and microwave frequencies*, in *Occupational and environmental health directorate, Radiofrequency Radiation Division*. 1996, Brooks Air Force Base: Texas (USA).
- [95] Fernandez, D.P., et al., *A database for the static dielectric-constant of water and steam*. Journal of Physical and Chemical Reference Data, 1995. **24**(1): p. 33-69.
- [96] Uematsu, M. and E.U. Franck, *Static dielectric-constant of water and steam*. Journal of Physical and Chemical Reference Data, 1980. **9**(4): p. 1291-1306.
- [97] WaterFacts. *Water and WasterWater*. 2018 [cited 2018 2018.04.21]; Available from: <https://web.archive.org/web/20100127024904/http://waterfacts.net/html/conductivity.html>.
- [98] Light, T.S., et al., *The fundamental conductivity and resistivity of water*. Electrochemical and Solid State Letters, 2005. **8**(1): p. E16-E19.
- [99] Sijher, T.S. and A.A. Kishk, *Antenna modeling by infinitesimal dipoles using genetic algorithms*. Progress in Electromagnetics Research-Pier, 2005. **52**: p. 225-254.
- [100] Mikki, S.a.K., A, *Infinitesimal dipole model for dielectric resonator antennas using the QPSO algorithm*, in *2006 IEEE Antennas and Propagation Society International Symposium*. 2006.
- [101] Wu, X.H., A.A. Kishk, and A.W. Glisson, *Modeling of wideband antennas by frequency-dependent Hertzian dipoles*. IEEE Transactions on Antennas and Propagation, 2008. **56**(8): p. 2481-2489.
- [102] Wust, P., et al., *Antenna arrays in the SIGMA-eye applicator: interactions and transforming networks*. Med Phys, 2001. **28**(8): p. 1793-805.
- [103] Floudas, C., *Handbook of test problems in local and global optimization*. 1999, Dordrecht: Kluwer Academic Publishers.
- [104] Ugray, Z., Lasdon, L., Plummer, J. C., Glover, F., Kelly, J., & Marti, R, *A multistart scatter search heuristic for smooth NLP and MINLP problems*. Metaheuristic Optimization via Memory and Evolution, 2005. **30**: p. 25-57.

7 TABLE AND FIGURE APPENDIX

Tab-Appendix.1: The optimal IDM weighting vector of the block of antenna 01

Tab-Appendix.2: The optimal IDM weighting vector of the block of antenna 02

Tab-Appendix.3: The optimal IDM weighting vector of the block of antenna 04

Tab-Appendix.4: The optimal IDM weighting vector of the block of antenna 05

Tab-Appendix.5: The optimal errors of the 24 equivalent dipole models

Tab-Appendix.6: The optimal IDM weighting vector of the isolated AUT

Fig-Appendix.1: Electric field E_x profiles of the four typical blocks respectively from the equivalent dipoles and COMSO at the operating frequency of 100 MHz

Fig-Appendix.2: Electric field E_y profiles of the four typical blocks respectively from the equivalent dipoles and COMSO at the operating frequency of 100 MHz

Fig-Appendix.3: Electric field E_z profiles of the four typical blocks respectively from the equivalent dipoles and COMSO at the operating frequency of 100 MHz

Fig-Appendix.4: Profiles of electric field components of the isolated antenna respectively from the equivalent dipoles and COMSO at the operating frequency of 100 MHz

Fig-Appendix.5: Electric field E_x profiles of the four typical blocks operating at 90 MHz respectively from 'simulated' and 'standard' electric field based on the reference frequency of 100 MHz

Fig-Appendix.6: Electric field E_y profiles of the four typical blocks operating at 90 MHz respectively from 'simulated' and 'standard' electric field based on the reference frequency of 100 MHz

Fig-Appendix.7: Electric field E_z profiles of the four typical blocks operating at 90 MHz respectively from 'simulated' and 'standard' electric field based on the reference frequency of 100 MHz

Fig-Appendix.8: Electric field E_x profiles of the four typical blocks operating at 95 MHz respectively from 'simulated' and 'standard' electric field based on the reference frequency of 100 MHz

Fig-Appendix.9: Electric field E_y profiles of the four typical blocks operating at 95 MHz respectively from 'simulated' and 'standard' electric field based on the reference frequency of 100 MHz

Fig-Appendix.10: Electric field E_z profiles of the four typical blocks operating at 95 MHz respectively from 'simulated' and 'standard' electric field based on the reference frequency of 100 MHz

Fig-Appendix.11: Electric field E_x profiles of the four typical blocks operating at 98 MHz respectively from 'simulated' and 'standard' electric field based on the reference frequency of 100 MHz

Fig-Appendix.12: Electric field E_y profiles of the four typical blocks operating at 98 MHz respectively from 'simulated' and 'standard' electric field based on the reference frequency of 100 MHz

Fig-Appendix.13: Electric field E_z profiles of the four typical blocks operating at 98 MHz respectively from 'simulated' and 'standard' electric field based on the reference frequency of 100 MHz

Fig-Appendix.14: Electric field E_x profiles of the four typical blocks operating at 103 MHz respectively from 'simulated' and 'standard' electric field based on the reference frequency of 100 MHz

Fig-Appendix.15: Electric field E_y profiles of the four typical blocks operating at 103 MHz respectively from 'simulated' and 'standard' electric field based on the reference frequency of 100 MHz

Fig-Appendix.16: Electric field E_z profiles of the four typical blocks operating at 103 MHz respectively from 'simulated' and 'standard' electric field based on the reference frequency of 100 MHz

Fig-Appendix.17: Electric field E_x profiles of the four typical blocks operating at 105 MHz respectively from 'simulated' and 'standard' electric field based on the reference frequency of 100 MHz

Fig-Appendix.18: Electric field E_y profiles of the four typical blocks operating at 105 MHz respectively from 'simulated' and 'standard' electric field based on the reference frequency of 100 MHz

Fig-Appendix.19: Electric field E_z profiles of the four typical blocks operating at 105 MHz respectively from 'simulated' and 'standard' electric field based on the reference frequency of 100 MHz

Fig-Appendix.20: Electric field E_x profiles of the four typical blocks operating at 110 MHz respectively from 'simulated' and 'standard' electric field based on the reference frequency of 100 MHz

Fig-Appendix.21: Electric field E_y profiles of the four typical blocks operating at 110 MHz respectively from 'simulated' and 'standard' electric field based on the reference frequency of 100 MHz

Fig-Appendix.22: Electric field E_z profiles of the four typical blocks operating at 110 MHz respectively from 'simulated' and 'standard' electric field based on the reference frequency of 100 MHz

Fig-Appendix.23: Electric field E_x profiles of the four typical blocks under the 'real' relative permittivity of water bolus of 70 respectively from 'simulated' and 'standard' electric field based on the 'measured' permittivity of 78

Fig-Appendix.24: Electric field E_y profiles of the four typical blocks under the 'real' relative permittivity of water bolus of 70 respectively from 'simulated' and 'standard' electric field based on the 'measured' permittivity of 78

Fig-Appendix.25: Electric field E_z profiles of the four typical blocks under the 'real' relative permittivity of water bolus of 70 respectively from 'simulated' and 'standard' electric field based on the 'measured' permittivity of 78

Fig-Appendix.26: Electric field E_x profiles of the four typical blocks under the 'real' relative permittivity of water bolus of 75 respectively from 'simulated' and 'standard' electric field based on the 'measured' permittivity of 78

Fig-Appendix.27: Electric field E_y profiles of the four typical blocks under the 'real' relative permittivity of water bolus of 75 respectively from 'simulated' and 'standard' electric field based on the 'measured' permittivity of 78

Fig-Appendix.28: Electric field E_z profiles of the four typical blocks under the 'real' relative permittivity of water bolus of 75 respectively from 'simulated' and 'standard' electric field based on the 'measured' permittivity of 78.

Fig-Appendix.29: Electric field E_x profiles of the four typical blocks under the 'real' relative permittivity of water bolus of 81 respectively from 'simulated' and 'standard' electric field based on the 'measured' permittivity of 78

Fig-Appendix.30: Electric field E_y profiles of the four typical blocks under the 'real' relative permittivity of water bolus of 81 respectively from 'simulated' and 'standard' electric field based on the 'measured' permittivity of 78

Fig-Appendix.31: Electric field E_z profiles of the four typical blocks under the 'real' relative permittivity of water bolus of 81 respectively from 'simulated' and 'standard' electric field based on the 'measured' permittivity of 78

Fig-Appendix.32: Electric field E_x profiles of the four typical blocks under the 'real' relative permittivity of water bolus of 85 respectively from 'simulated' and 'standard' electric field based on the 'measured' permittivity of 78

Fig-Appendix.33: Electric field E_y profiles of the four typical blocks under the 'real' relative permittivity of water bolus of 85 respectively from 'simulated' and 'standard' electric field based on the 'measured' permittivity of 78

Fig-Appendix.34: Electric field E_z profiles of the four typical blocks under the 'real' relative permittivity of water bolus of 85 respectively from 'simulated' and 'standard' electric field based on the 'measured' permittivity of 78

Fig-Appendix.35: Electric field E_x profiles of the four typical blocks under the 'real' conductivity of water bolus of 0.005 S/m respectively from 'simulated' and 'standard' electric field based on the 'measured' conductivity of 0 S/m

Fig-Appendix.36: Electric field E_y profiles of the four typical blocks under the 'real' conductivity of water bolus of 0.005 S/m respectively from 'simulated' and 'standard' electric field based on the 'measured' conductivity of 0 S/m

Fig-Appendix.37: Electric field E_z profiles of the four typical blocks under the 'real' conductivity of water bolus of 0.005 S/m respectively from 'simulated' and 'standard' electric field based on the 'measured' conductivity of 0 S/m

Fig-Appendix.38: Electric field E_x profiles of the four typical blocks under the 'real' conductivity of water bolus of 0.01 S/m respectively from 'simulated' and 'standard' electric field based on the 'measured' conductivity of 0 S/m

Fig-Appendix.39: Electric field E_y profiles of the four typical blocks under the 'real' conductivity of water bolus of 0.01 S/m respectively from 'simulated' and 'standard' electric field based on the 'measured' conductivity of 0 S/m

Fig-Appendix.40: Electric field E_z profiles of the four typical blocks under the 'real' conductivity of water bolus of 0.01 S/m respectively from 'simulated' and 'standard' electric field based on the 'measured' conductivity of 0 S/m

Fig-Appendix.41: Electric field E_x profiles of the four typical blocks under the 'real' conductivity of water bolus of 0.05 S/m respectively from 'simulated' and 'standard' electric field based on the 'measured' conductivity of 0 S/m

Fig-Appendix.42: Electric field E_y profiles of the four typical blocks under the 'real' conductivity of water bolus of 0.05 S/m respectively from 'simulated' and 'standard' electric field based on the 'measured' conductivity of 0 S/m

Fig-Appendix.43: Electric field E_z profiles of the four typical blocks under the 'real' conductivity of water bolus of 0.05 S/m respectively from 'simulated' and 'standard' electric field based on the 'measured' conductivity of 0 S/m

Tab-Appendix.1: The optimal IDM weighting vector of the block of antenna 01

Dipole	I_x/I_0	I_y/I_0	I_z/I_0	$\theta(\text{radian})$
No.01	0.5576	0.2391	-0.6492	0.0095
No.02	-0.0037	-0.0091	0.0923	-0.0235
No.03	0.0387	-0.0583	0.1805	-0.1936
No.04	-0.2094	-0.0549	-0.0660	0.0704
No.05	-0.5502	-0.4581	-0.0132	-0.0821
No.06	-1.1364	-0.0018	0.6080	-0.0538
No.07	0.4720	0.0078	0.0213	0.0845
No.08	0.0283	0.0023	0.0019	0.0393
No.09	1.3761	0.6627	-1.8564	-0.0548
No.10	0.3233	0.0770	-0.8093	0.1175
No.11	0.4339	0.1163	1.0690	-0.2461
No.12	-1.2751	-0.4980	0.1149	-0.0220

Tab-Appendix.2: The optimal IDM weighting vector of the block of antenna 02

Dipole	I_x/I_0	I_y/I_0	I_z/I_0	$\theta(\text{radian})$
No.01	0.0733	0.1007	-0.2645	0.2391
No.02	-0.0042	-0.0005	0.0776	-0.0248
No.03	-0.0798	-0.0532	0.3291	-0.2217
No.04	0.0439	-0.0325	-0.0090	0.1169
No.05	0.0354	-0.0352	-0.2888	0.1404
No.06	0.0012	-0.0019	-0.1420	0.0030
No.07	0.1572	-0.0009	-0.5500	-0.0768
No.08	-0.0056	0.0067	-0.8247	0.1003
No.09	-0.0700	0.0981	-0.0022	0.0055
No.10	-0.2450	0.0026	0.3450	-0.0976
No.11	0.1374	0.0615	0.2440	-0.4198
No.12	-0.0333	-0.1392	-0.2027	0.0034

Tab-Appendix.3: The optimal IDM weighting vector of the block of antenna 04

Dipole	I_x/I_0	I_y/I_0	I_z/I_0	$\theta(\text{radian})$
No.01	-0.0361	-0.2652	-0.8134	-0.2213
No.02	-0.0718	-0.7897	0.6366	0.3375
No.03	0.0202	-0.0021	-0.0034	-0.0102
No.04	0.1725	1.2564	-0.4939	0.2162
No.05	0.0275	0.0567	-0.0049	0.1483
No.06	0.2582	1.3242	-0.5052	0.2641
No.07	-0.1743	-0.4933	0.8952	-0.0538
No.08	-0.3263	-0.5887	-0.0654	0.2022
No.09	-0.0020	-0.0042	-0.0147	0.0120
No.10	-0.1359	-1.9702	-1.1033	0.3638
No.11	0.2602	0.2514	-1.6275	0.0686
No.12	-0.0020	1.1793	1.6585	0.3591

Tab-Appendix.4: The optimal IDM weighting vector of the block of antenna 05

Dipole	I_x/I_0	I_y/I_0	I_z/I_0	$\theta(\text{radian})$
No.01	0.0859	-0.1381	-0.2780	-0.1070
No.02	-0.1268	-0.0345	0.0010	-0.1354
No.03	-0.0027	0.0012	-0.0224	-0.0632
No.04	0.0026	0.3094	-0.0007	-0.0046
No.05	0.0228	0.0040	0.0778	0.0478
No.06	-0.0023	0.0546	-0.0320	-0.0046
No.07	0.0159	-0.0779	-0.8518	-0.0572
No.08	0.0340	-0.0031	-0.0451	-0.0220
No.09	0.0033	-0.1553	-0.3747	0.0344
No.10	-0.0121	-0.1607	-0.0514	0.0836
No.11	-0.0661	0.0120	0.4625	0.0998
No.12	0.0437	0.1844	-0.3353	-0.0131

Tab-Appendix.5: The optimal errors of the 24 equivalent dipole models

Block	Error (%)	Block	Error (%)
Block 01	5.76	Block 13	5.74
Block 02	5.69	Block 14	5.97
Block 03	5.71	Block 15	5.64
Block 04	6.98	Block 16	6.50
Block 05	5.21	Block 17	4.00
Block 06	6.77	Block 18	6.72
Block 07	6.90	Block 19	7.07
Block 08	3.97	Block 20	5.34
Block 09	6.77	Block 21	7.01
Block 10	6.01	Block 22	5.96
Block 11	6.00	Block 23	6.14
Block 12	5.88	Block 24	5.81

Tab-Appendix.6: The optimal IDM weighting vector of the isolated AUT

Dipole	I_x/I_0	I_y/I_0	I_z/I_0	$\theta(\text{radian})$
No.01	-0.0006	0.0002	-0.0165	-0.0190
No.02	-0.0000	0.0001	-0.0033	-0.2565
No.03	-0.0010	-0.0005	-0.0121	0.1026
No.04	0.0075	0.0057	-0.3983	-0.0172
No.05	0.0062	0.0036	-0.0874	0.2137
No.06	-0.0267	-0.0223	-0.0610	0.0732
No.07	0.0069	0.0081	-0.2292	0.1418
No.08	0.0083	0.0066	-0.4303	-0.0189
No.09	0.0011	-0.0005	-0.1995	0.0146
No.10	-0.0018	0.0017	0.0684	-0.0320
No.11	0.0044	-0.0017	-0.0430	-0.0319
No.12	-0.0046	-0.0009	-0.0135	-0.0234

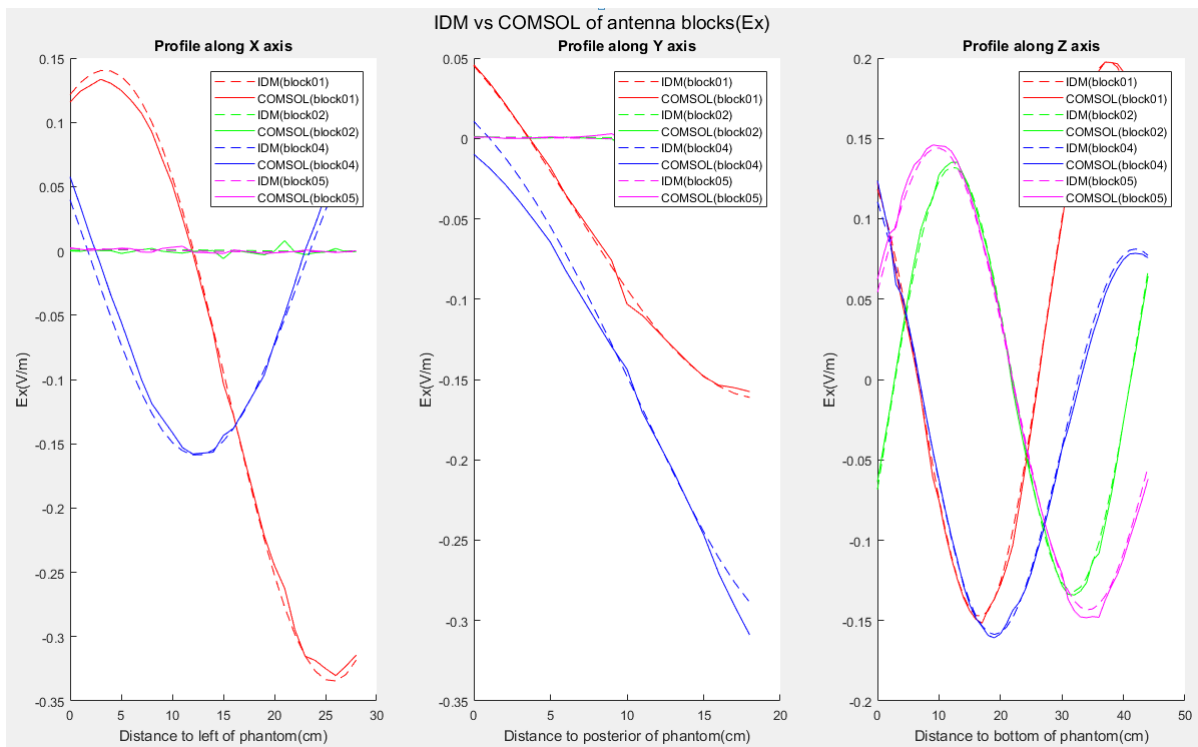


Fig-Appendix.1: Electric field E_x profiles of the four typical blocks respectively from the equivalent dipoles and COMSO at the operating frequency of 100 MHz

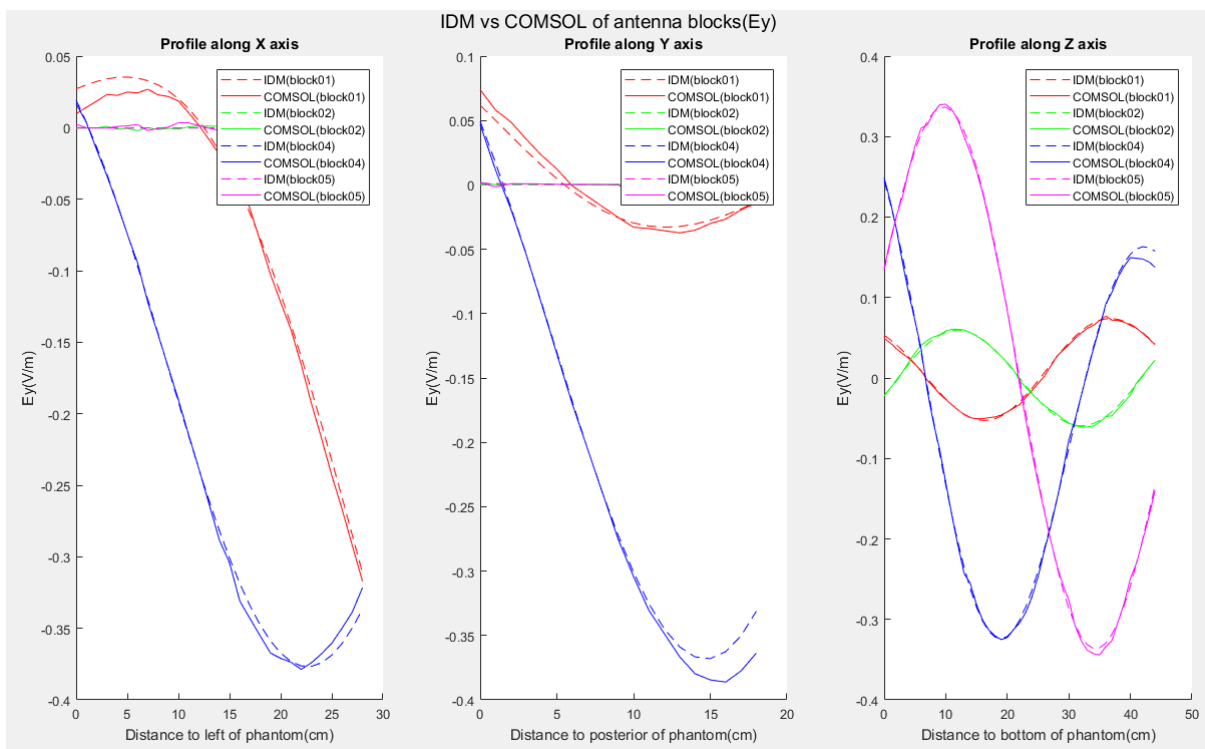


Fig-Appendix.2: Electric field E_y profiles of the four typical blocks respectively from the equivalent dipoles and COMSO at the operating frequency of 100 MHz

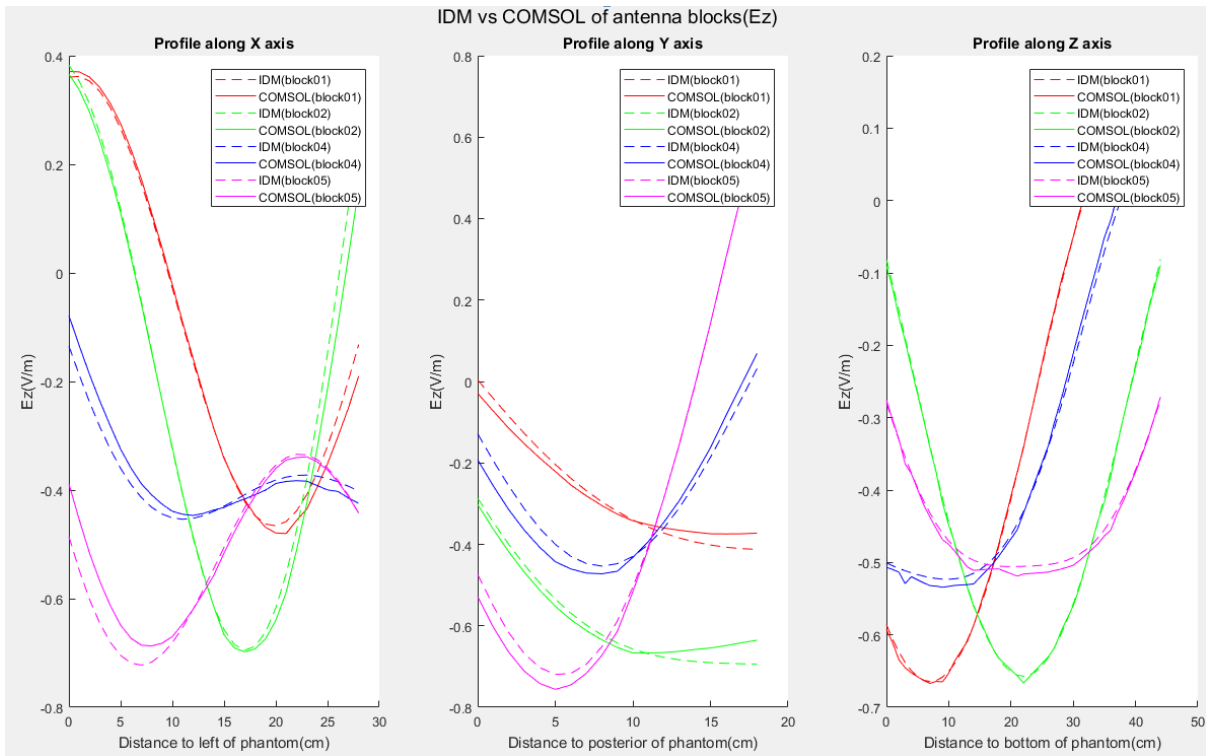


Fig-Appendix.3: Electric field E_z profiles of the four typical blocks respectively from the equivalent dipoles and COMSO at the operating frequency of 100 MHz

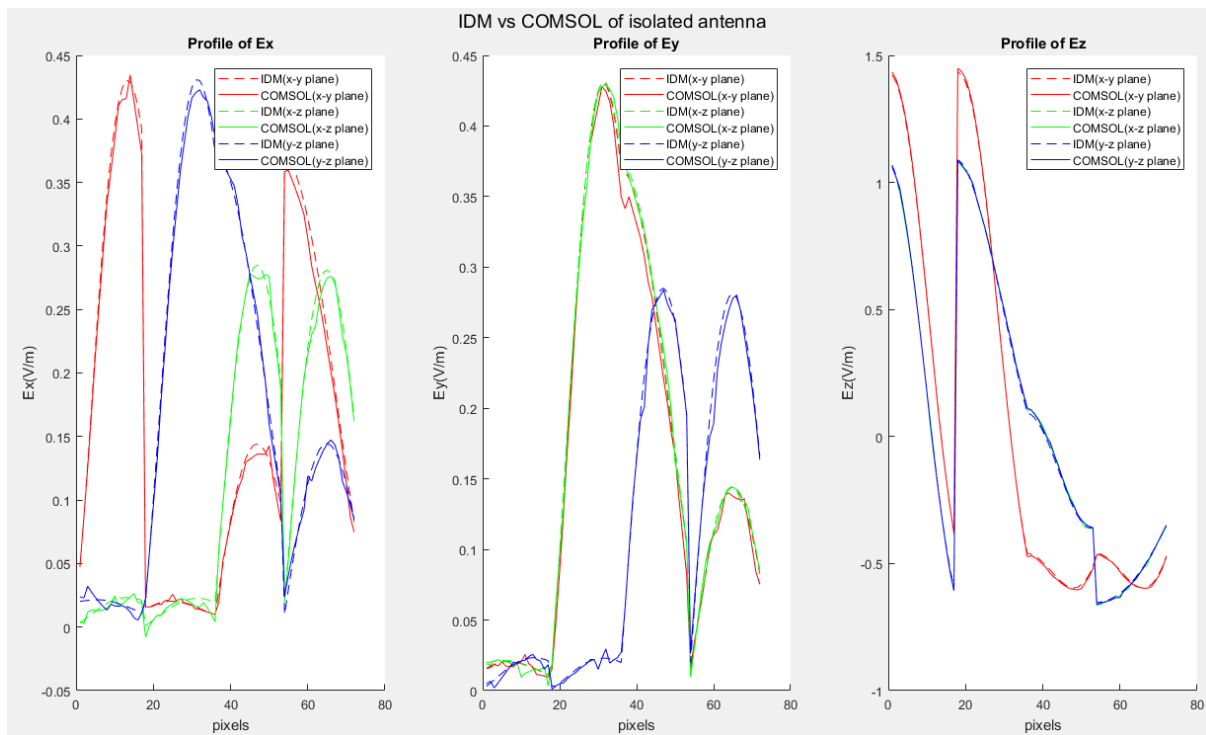


Fig-Appendix.4: Profiles of electric field components of the isolated antenna respectively from the equivalent dipoles and COMSO at the operating frequency of 100 MHz

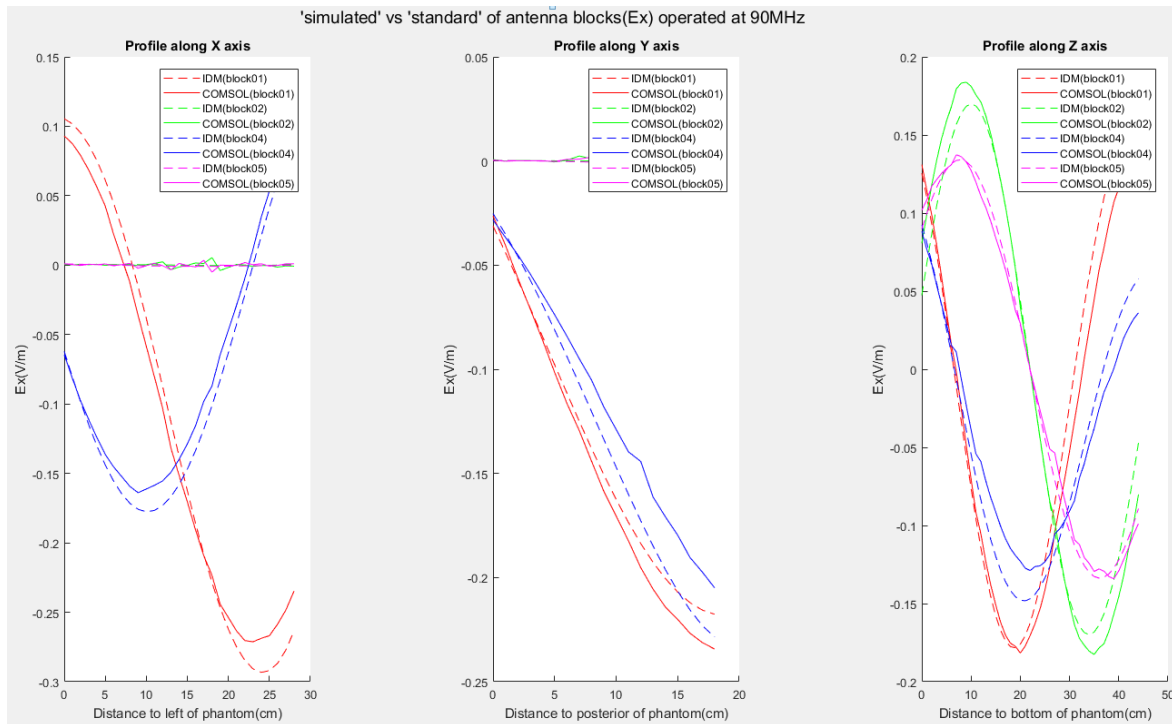


Fig-Appendix.5: Electric field E_x profiles of the four typical blocks operating at 90 MHz respectively from 'simulated' and 'standard' electric field based on the reference frequency of 100 MHz

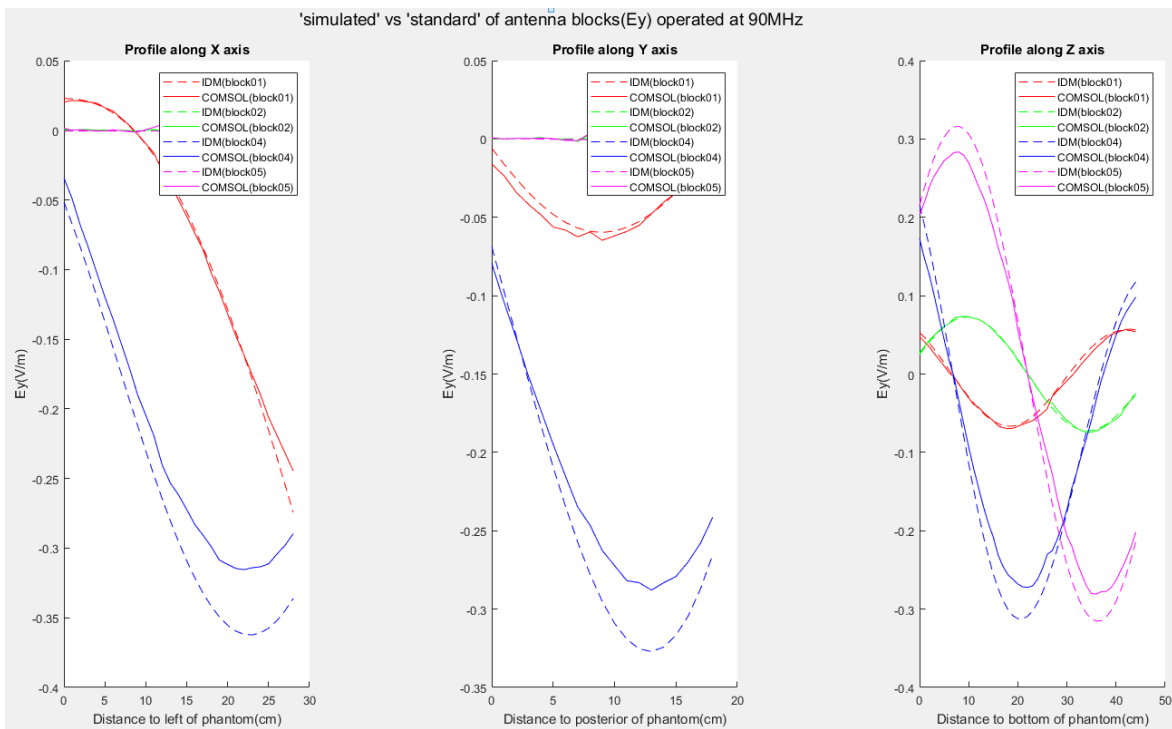


Fig-Appendix.6: Electric field E_y profiles of the four typical blocks operating at 90 MHz respectively from 'simulated' and 'standard' electric field based on the reference frequency of 100 MHz

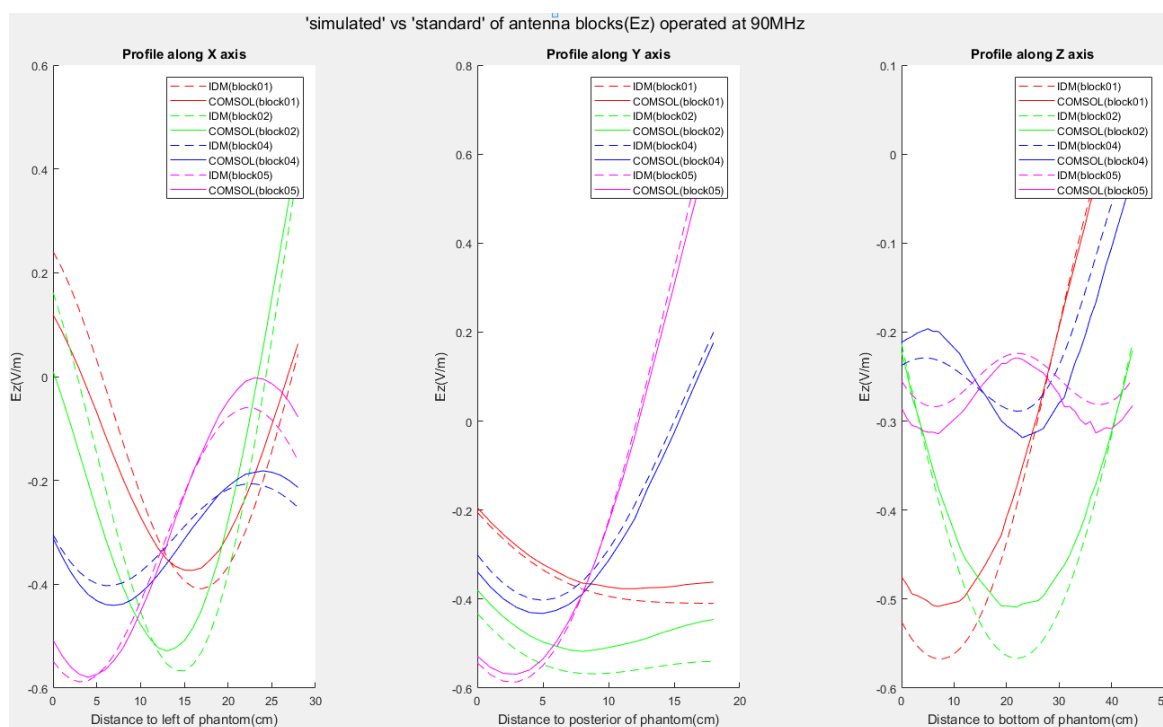


Fig-Appendix.7: Electric field E_z profiles of the four typical blocks operating at 90 MHz respectively from 'simulated' and 'standard' electric field based on the reference frequency of 100 MHz

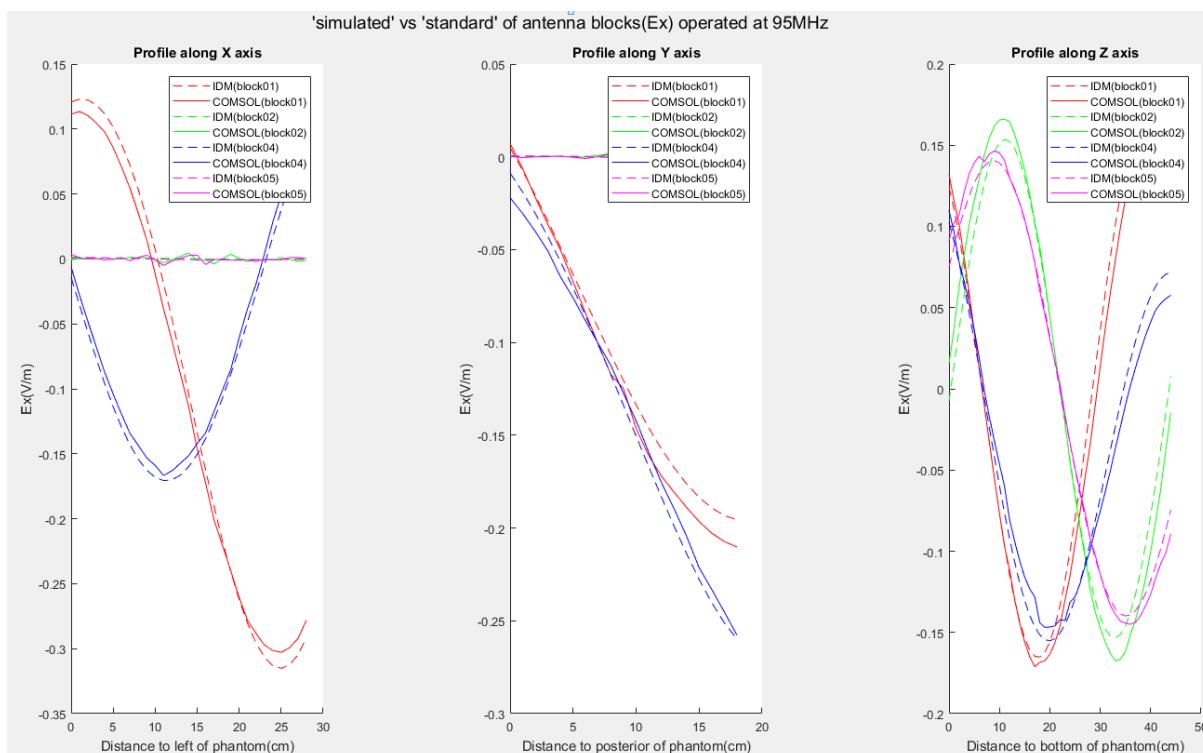


Fig-Appendix.8: Electric field E_x profiles of the four typical blocks operating at 95 MHz respectively from 'simulated' and 'standard' electric field based on the reference frequency of 100 MHz

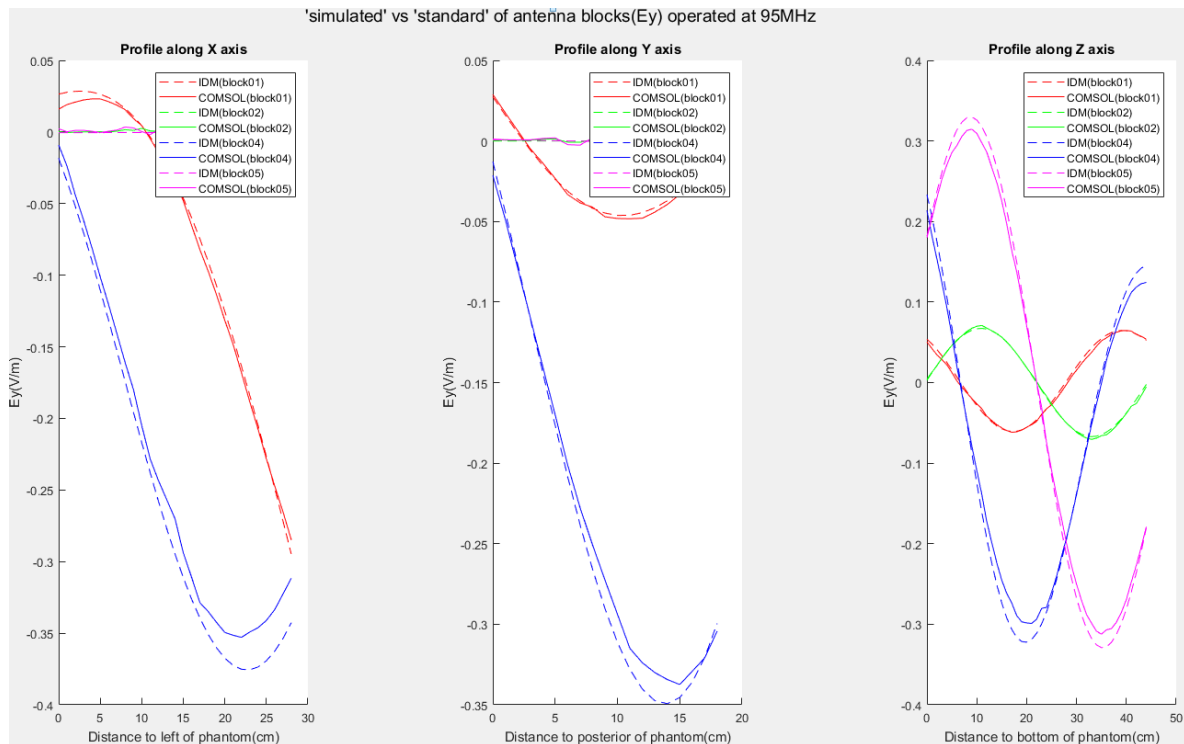


Fig-Appendix.9: Electric field E_y profiles of the four typical blocks operating at 95 MHz respectively from 'simulated' and 'standard' electric field based on the reference frequency of 100 MHz

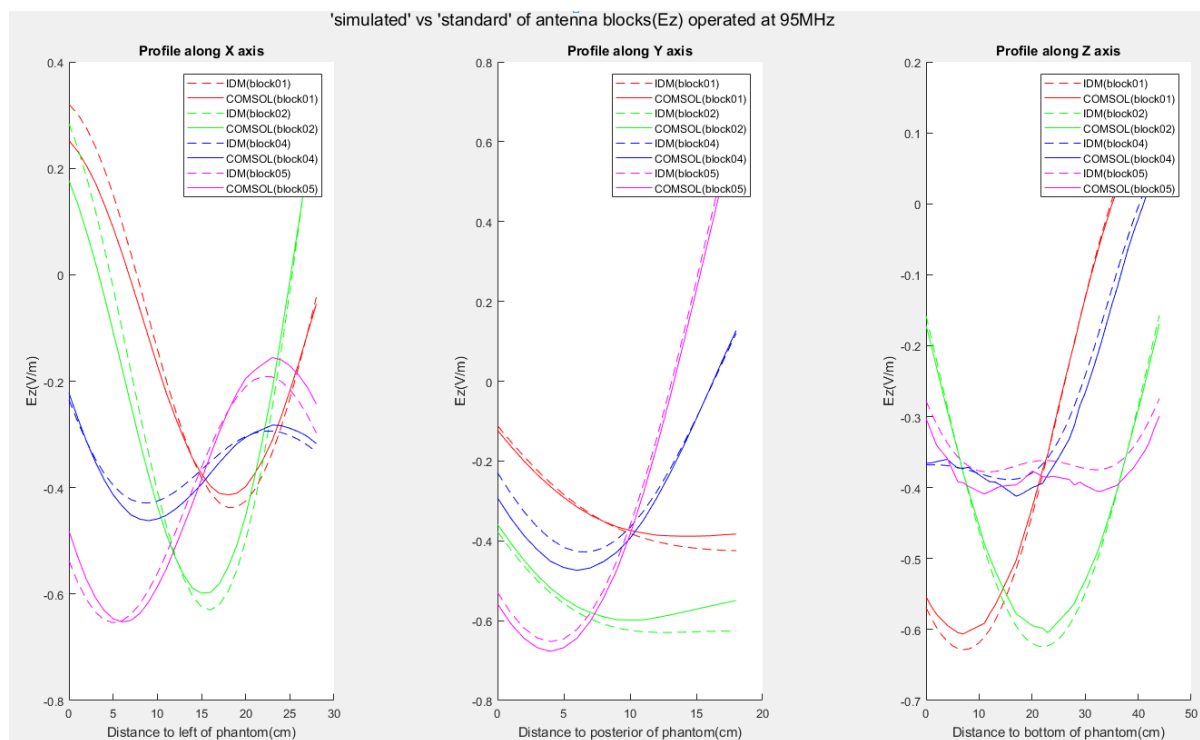


Fig-Appendix.10: Electric field E_z profiles of the four typical blocks operating at 95 MHz respectively from 'simulated' and 'standard' electric field based on the reference frequency of 100 MHz

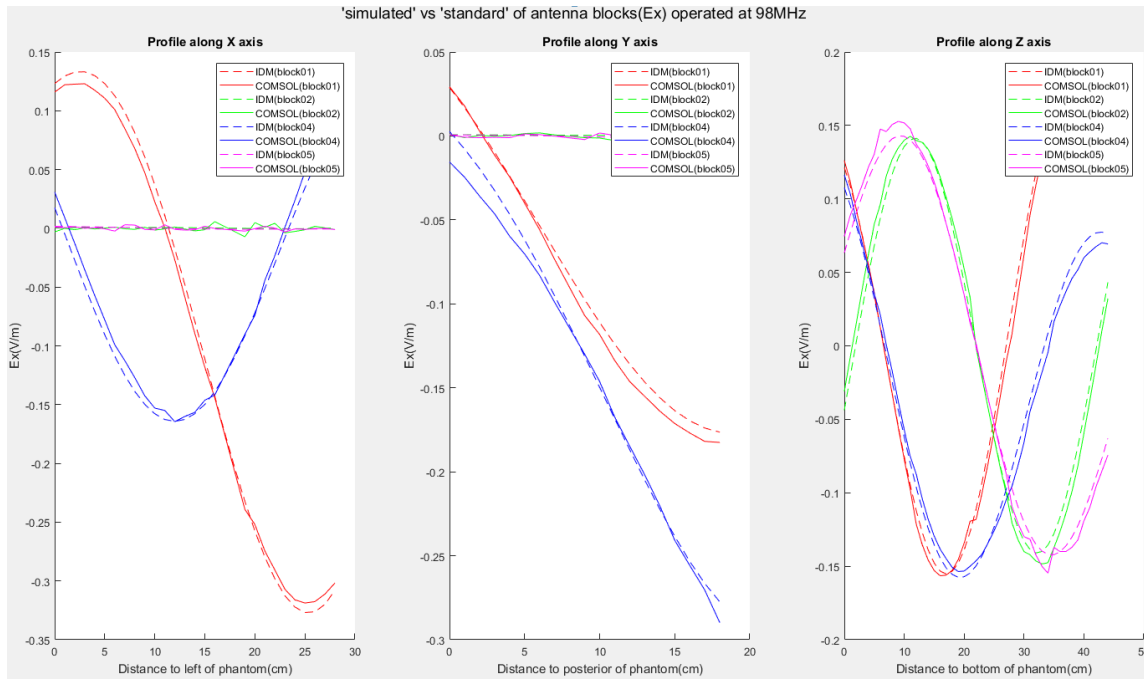


Fig-Appendix.11: Electric field E_x profiles of the four typical blocks operating at 98 MHz respectively from 'simulated' and 'standard' electric field based on the reference frequency of 100 MHz

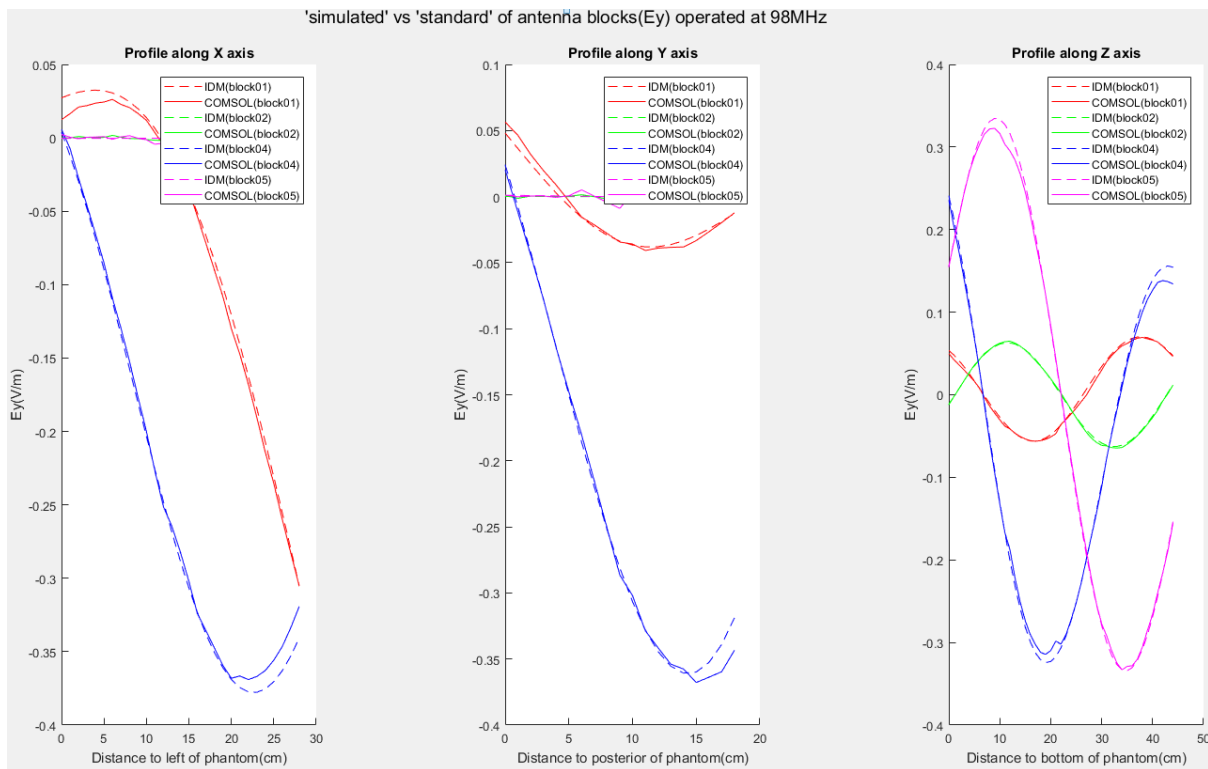


Fig-Appendix.12: Electric field E_y profiles of the four typical blocks operating at 98 MHz respectively from 'simulated' and 'standard' electric field based on the reference frequency of 100 MHz

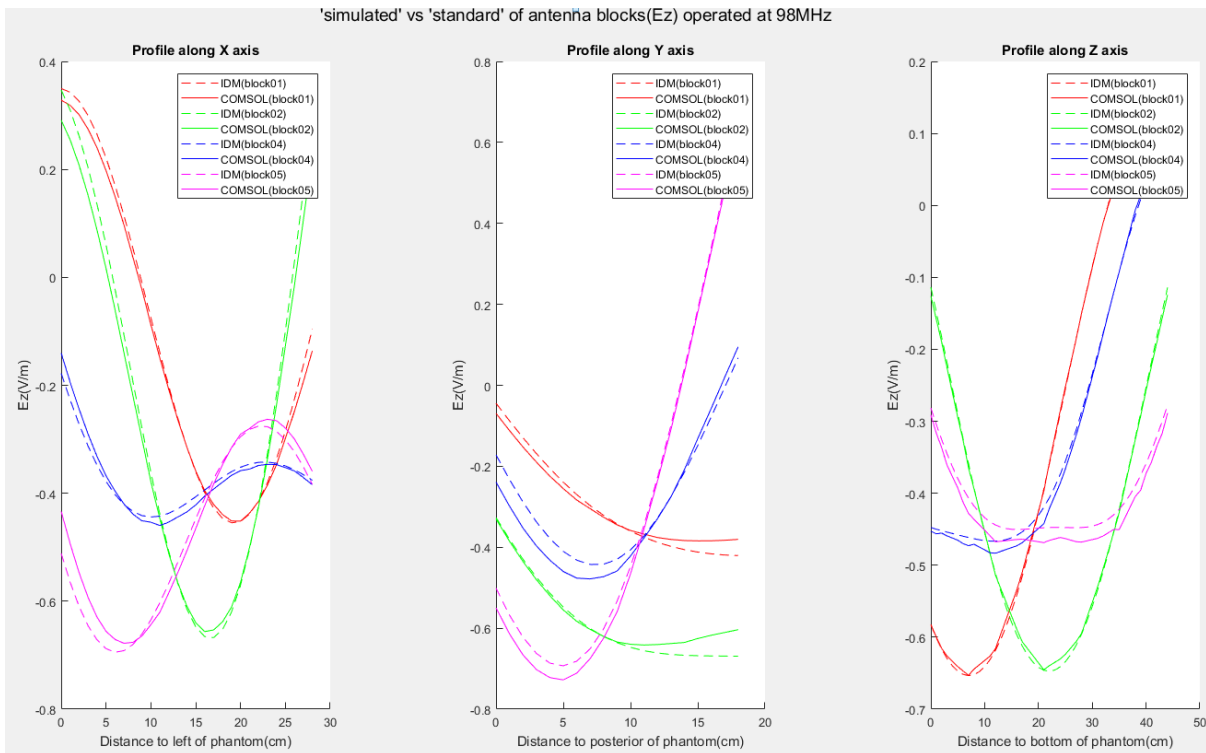


Fig-Appendix.13: Electric field E_z profiles of the four typical blocks operating at 98 MHz respectively from 'simulated' and 'standard' electric field based on the reference frequency of 100 MHz

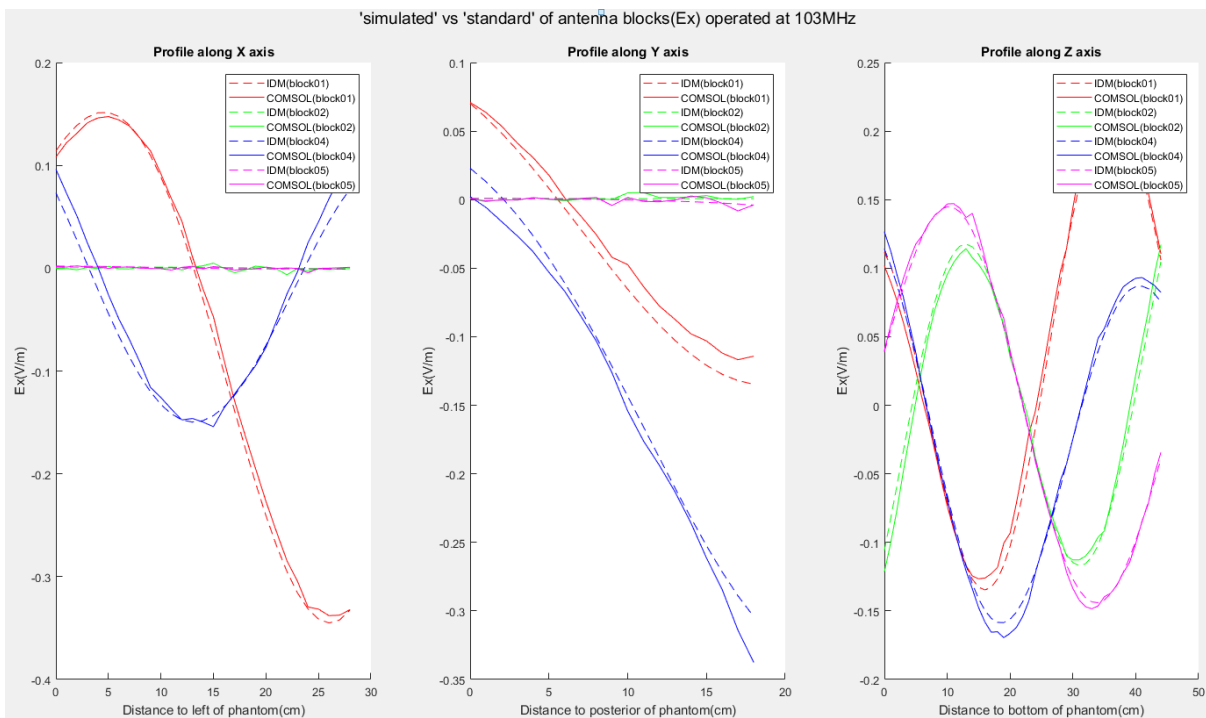


Fig-Appendix.14: Electric field E_x profiles of the four typical blocks operating at 103 MHz respectively from 'simulated' and 'standard' electric field based on the reference frequency of 100 MHz

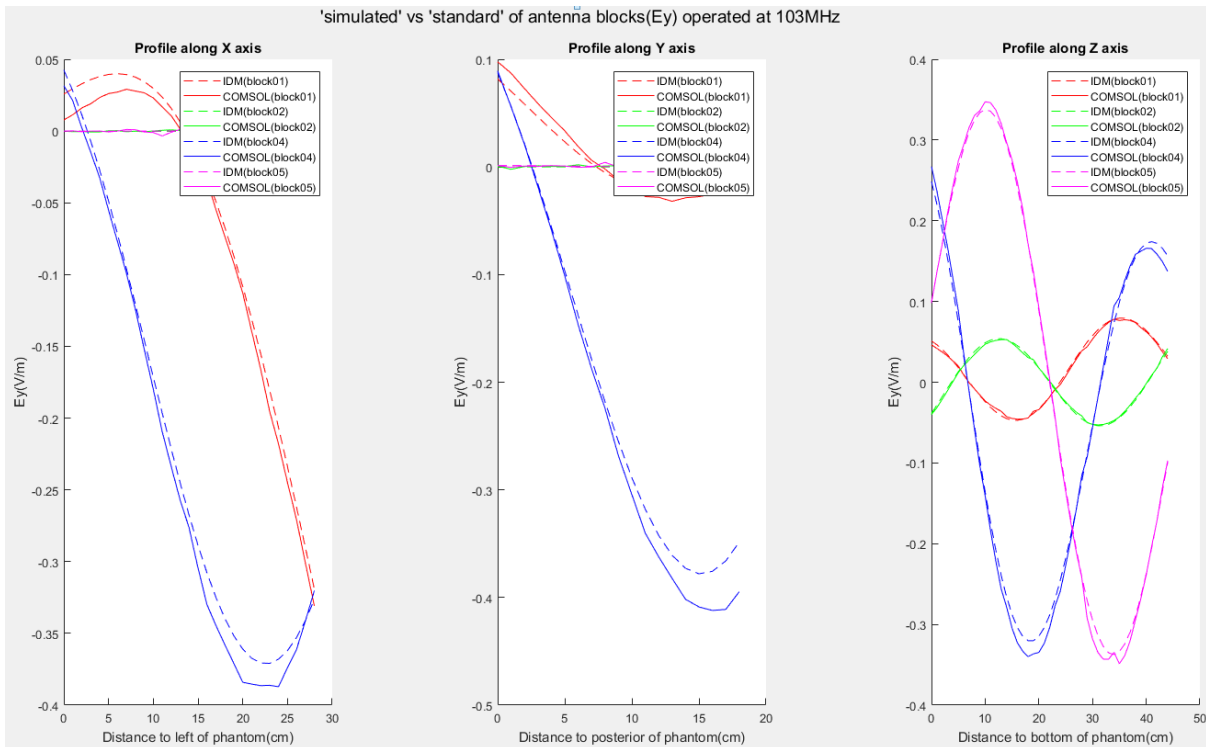


Fig-Appendix.15: Electric field E_y profiles of the four typical blocks operating at 103 MHz respectively from 'simulated' and 'standard' electric field based on the reference frequency of 100 MHz

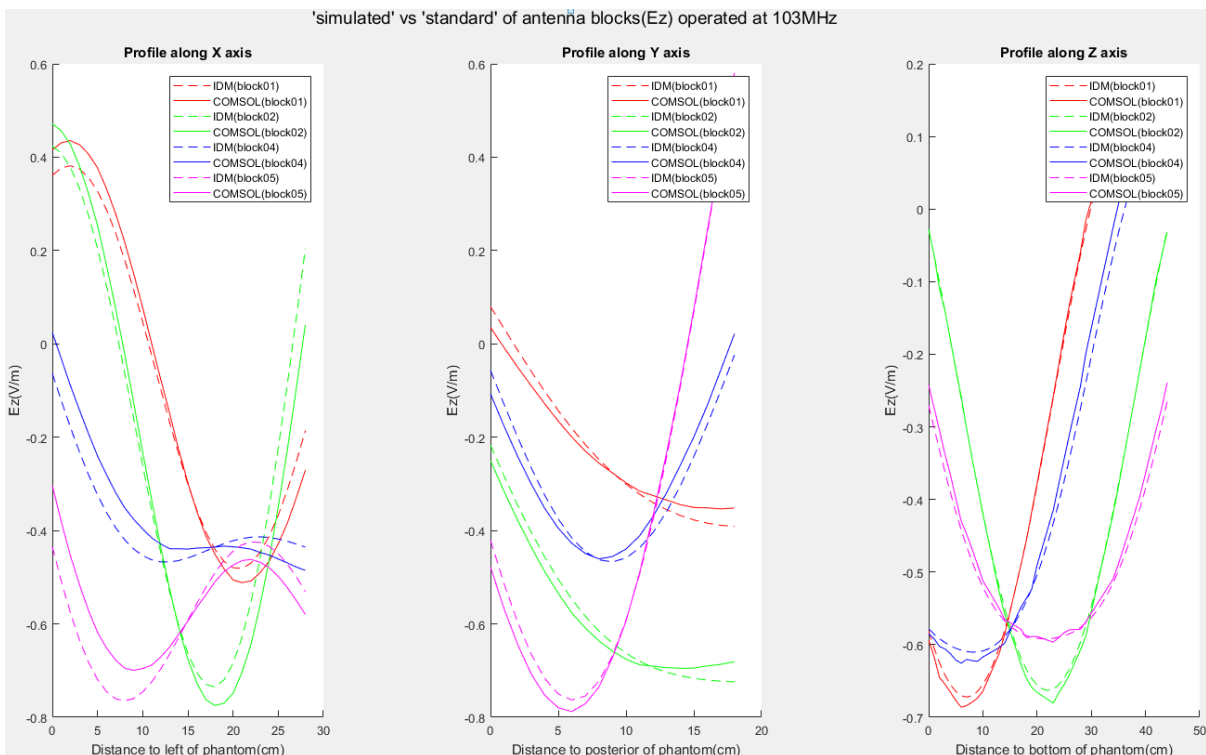


Fig-Appendix.16: Electric field E_z profiles of the four typical blocks operating at 103 MHz respectively from 'simulated' and 'standard' electric field based on the reference frequency of 100 MHz

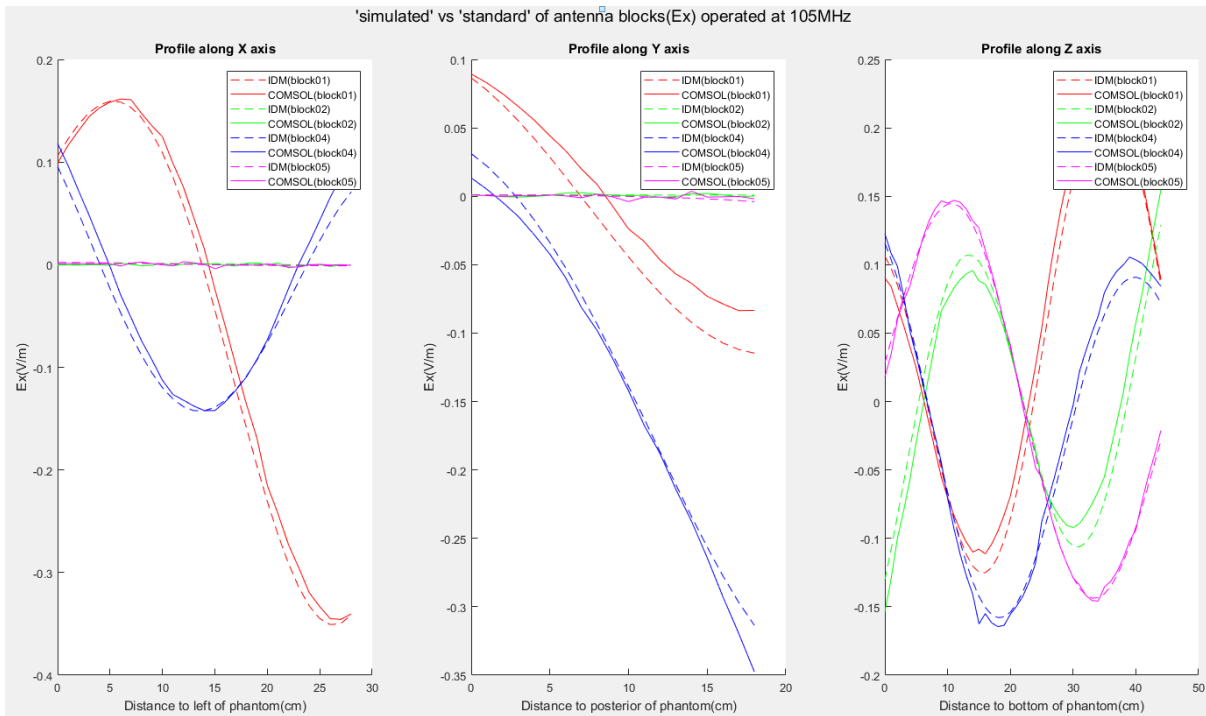


Fig-Appendix.17: Electric field E_x profiles of the four typical blocks operating at 105 MHz respectively from 'simulated' and 'standard' electric field based on the reference frequency of 100 MHz

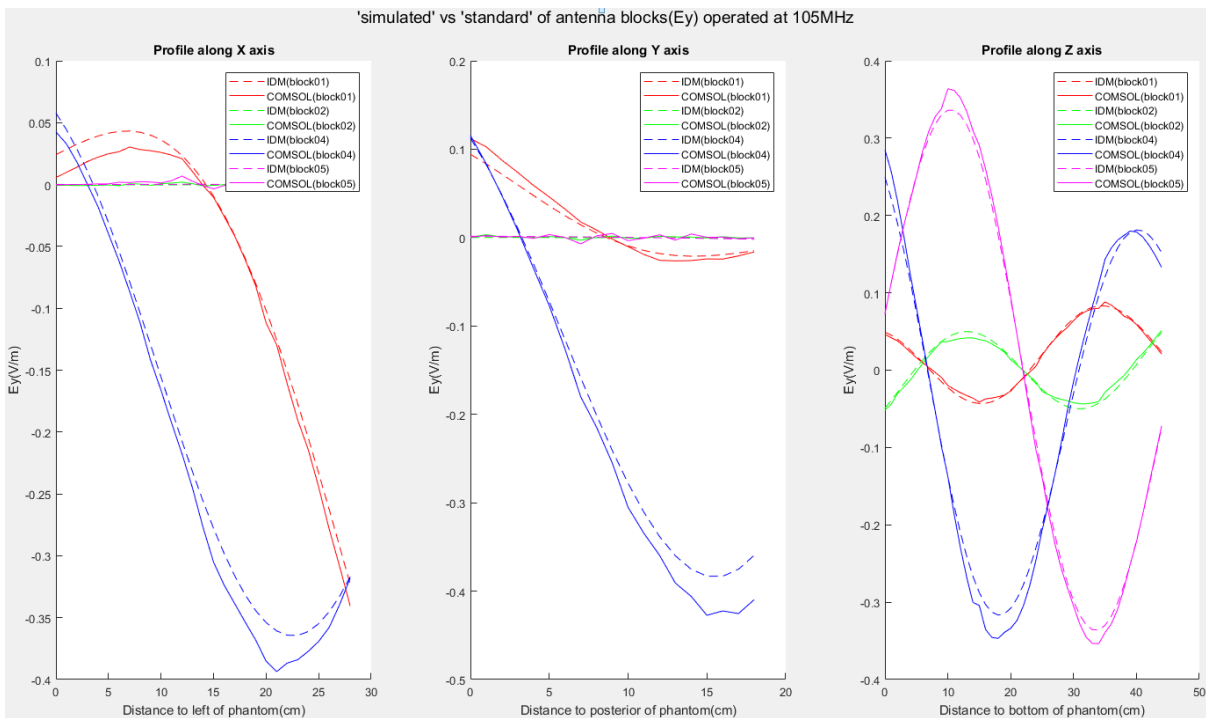


Fig-Appendix.18: Electric field E_y profiles of the four typical blocks operating at 105 MHz respectively from 'simulated' and 'standard' electric field based on the reference frequency of 100 MHz

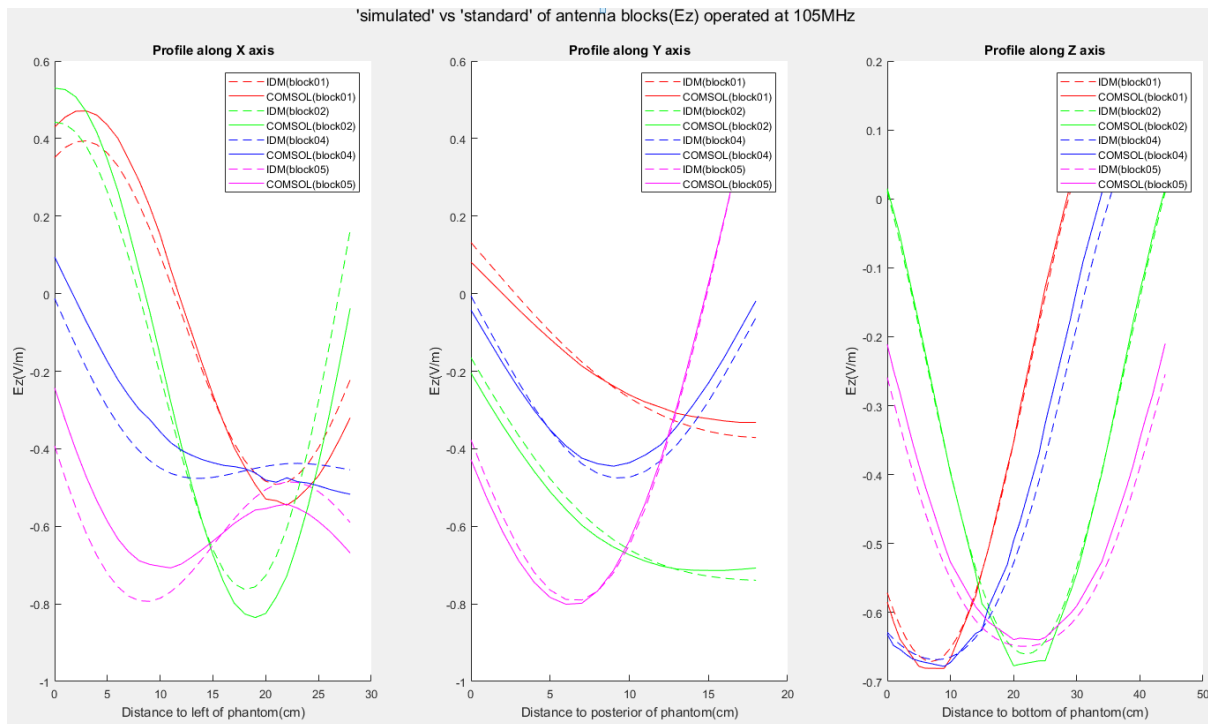


Fig-Appendix.19: Electric field E_z profiles of the four typical blocks operating at 105 MHz respectively from 'simulated' and 'standard' electric field based on the reference frequency of 100 MHz

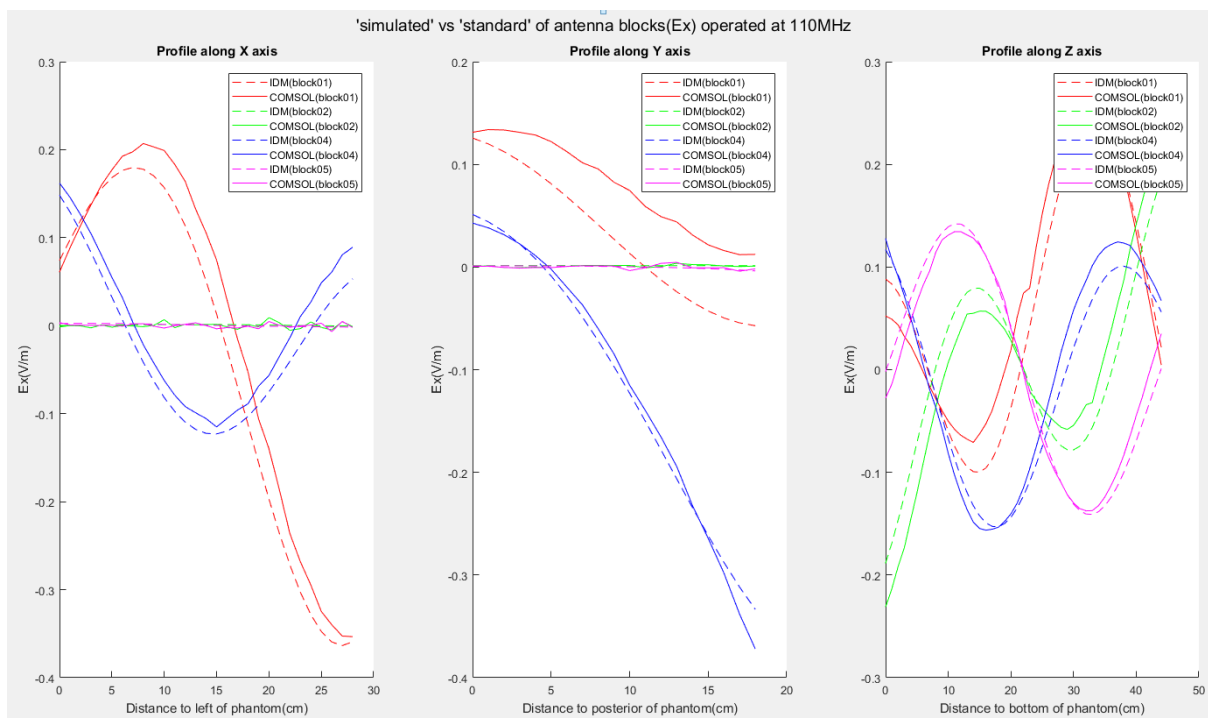


Fig-Appendix.20: Electric field E_x profiles of the four typical blocks operating at 110 MHz respectively from 'simulated' and 'standard' electric field based on the reference frequency of 100 MHz

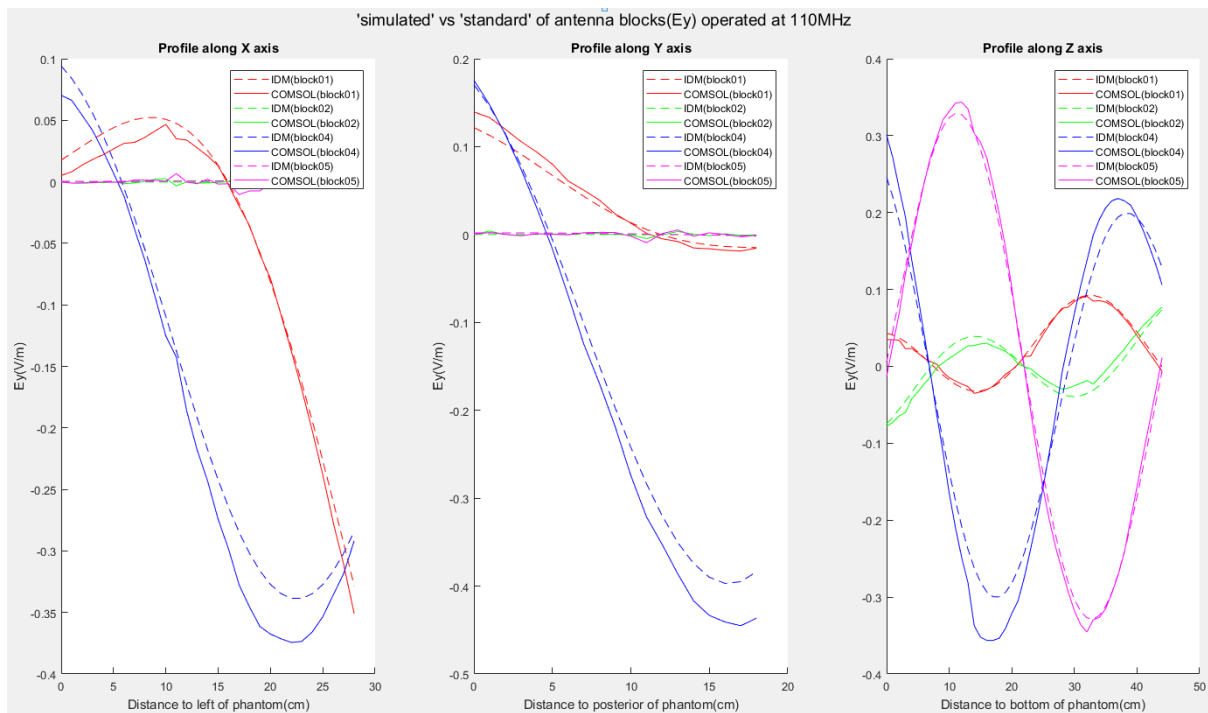


Fig-Appendix.21: Electric field E_y profiles of the four typical blocks operating at 110 MHz respectively from 'simulated' and 'standard' electric field based on the reference frequency of 100 MHz

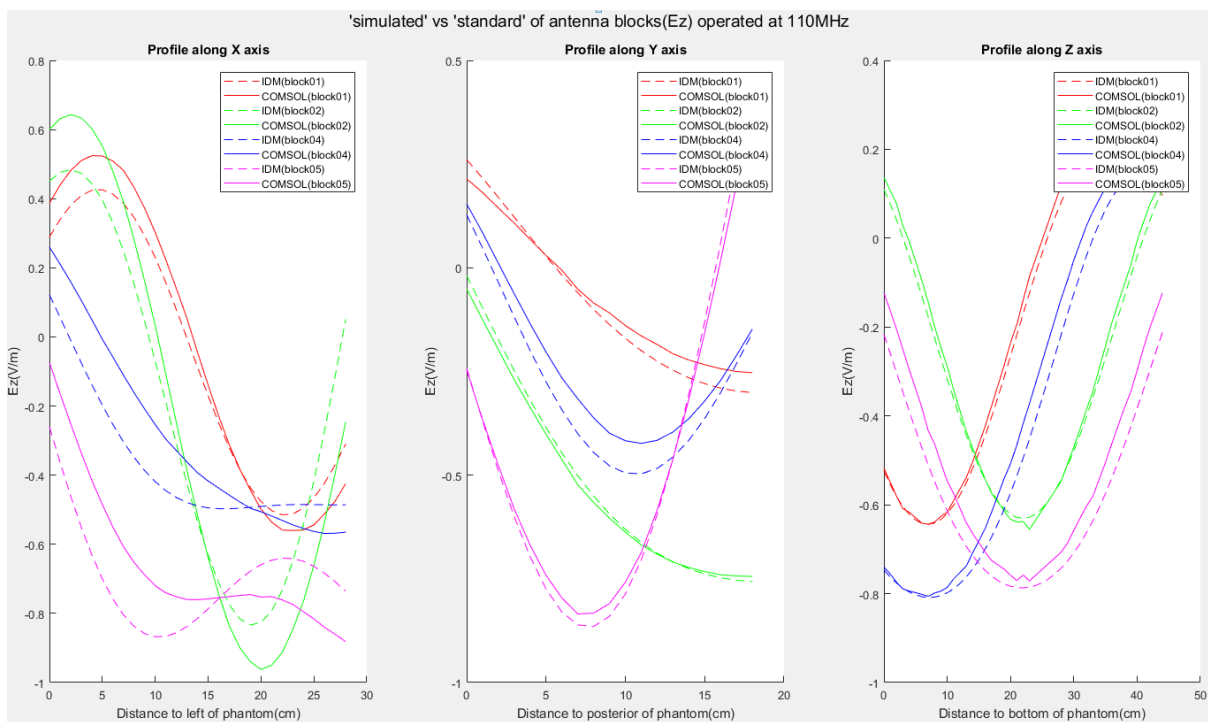


Fig-Appendix.22: Electric field E_z profiles of the four typical blocks operating at 110 MHz respectively from 'simulated' and 'standard' electric field based on the reference frequency of 100 MHz

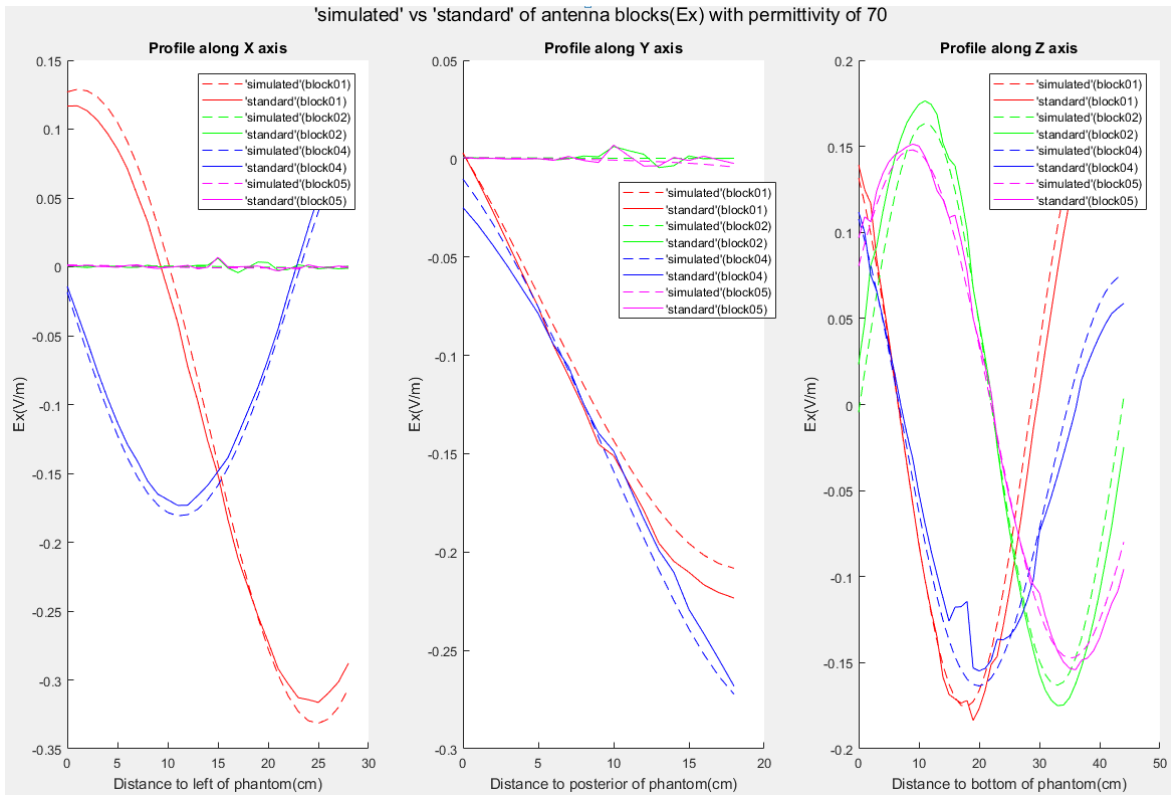


Fig-Appendix.23: Electric field E_x profiles of the four typical blocks under the 'real' relative permittivity of water bolus of 70 respectively from 'simulated' and 'standard' electric field based on the 'measured' permittivity of 78

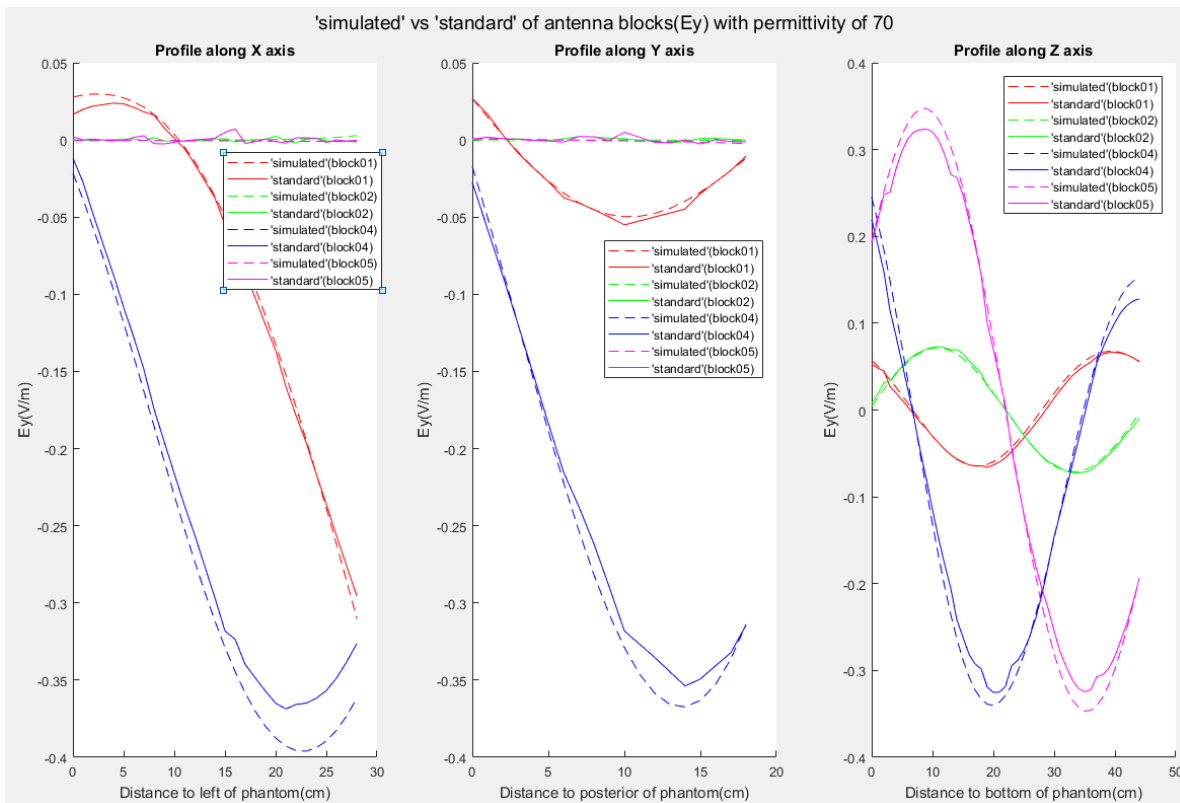


Fig-Appendix.24: Electric field E_y profiles of the four typical blocks under the 'real' relative permittivity of water bolus of 70 respectively from 'simulated' and 'standard' electric field based on the 'measured' permittivity of 78

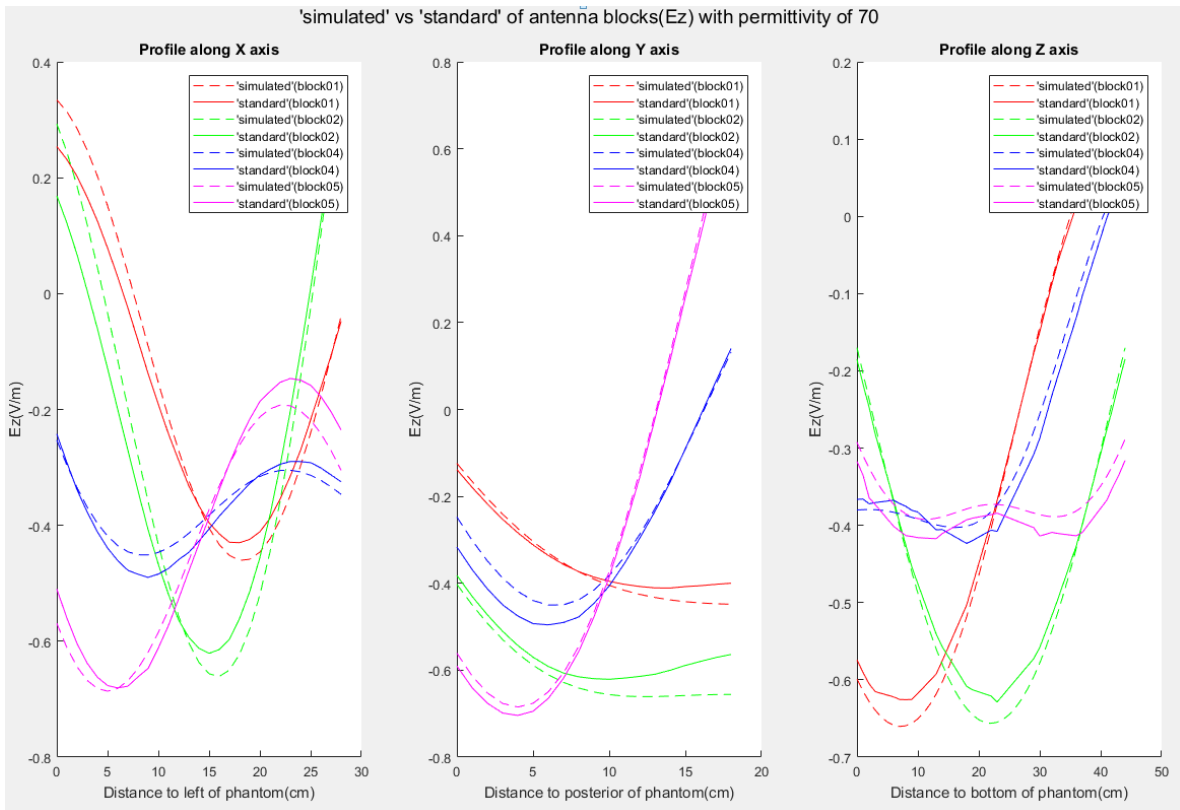


Fig-Appendix.25: Electric field E_z profiles of the four typical blocks under the 'real' relative permittivity of water bolus of 70 respectively from 'simulated' and 'standard' electric field based on the 'measured' permittivity of 78

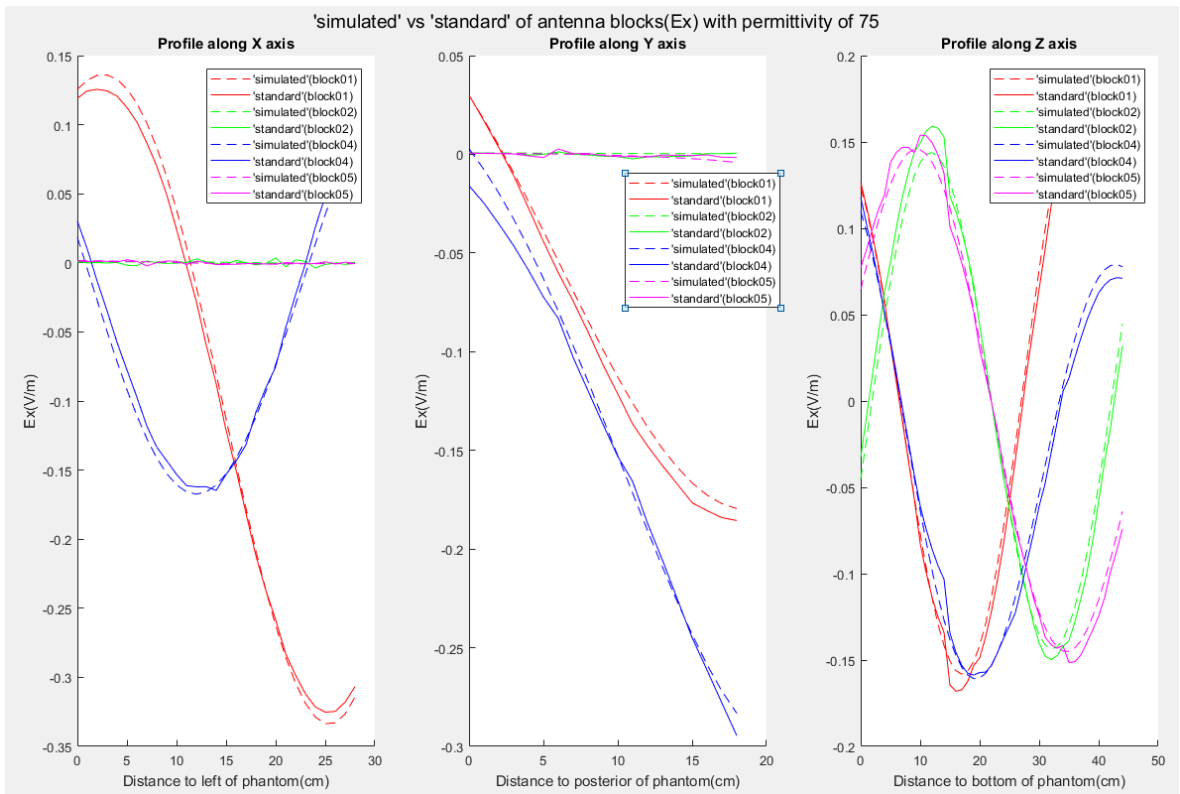


Fig-Appendix.26: Electric field E_x profiles of the four typical blocks under the 'real' relative permittivity of water bolus of 75 respectively from 'simulated' and 'standard' electric field based on the 'measured' permittivity of 78

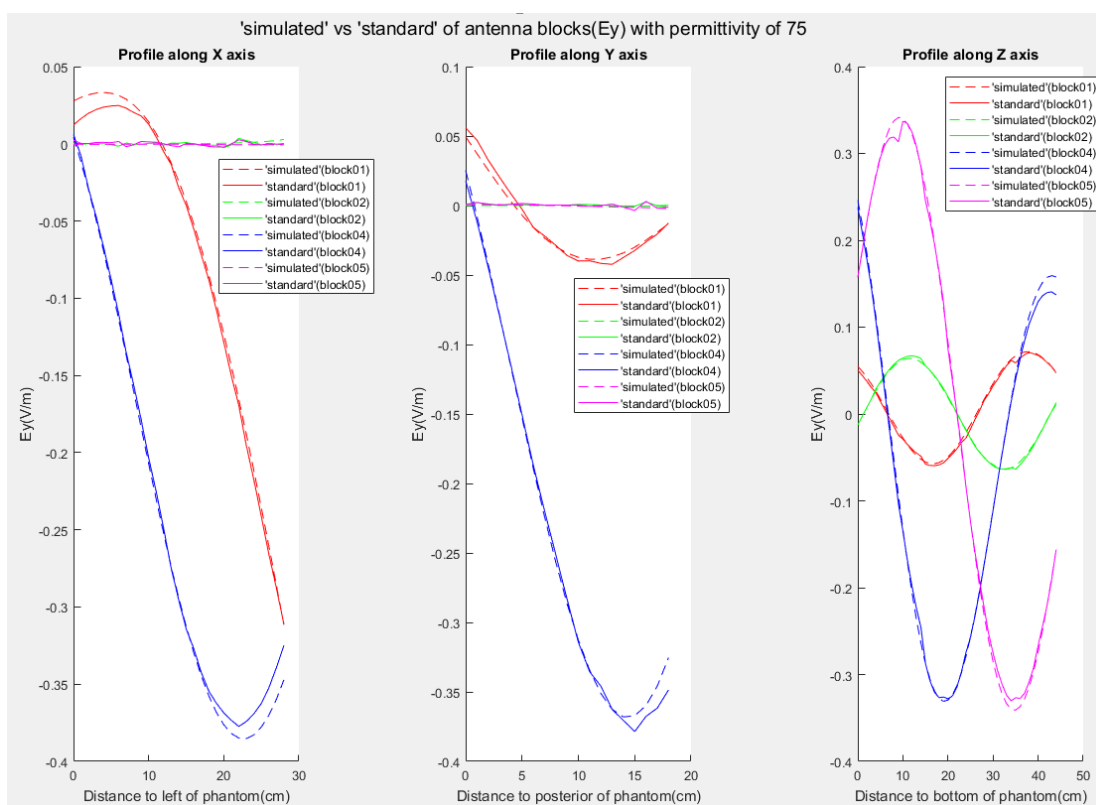


Fig-Appendix.27: Electric field E_y profiles of the four typical blocks under the 'real' relative permittivity of water bolus of 75 respectively from 'simulated' and 'standard' electric field based on the 'measured' permittivity of 78

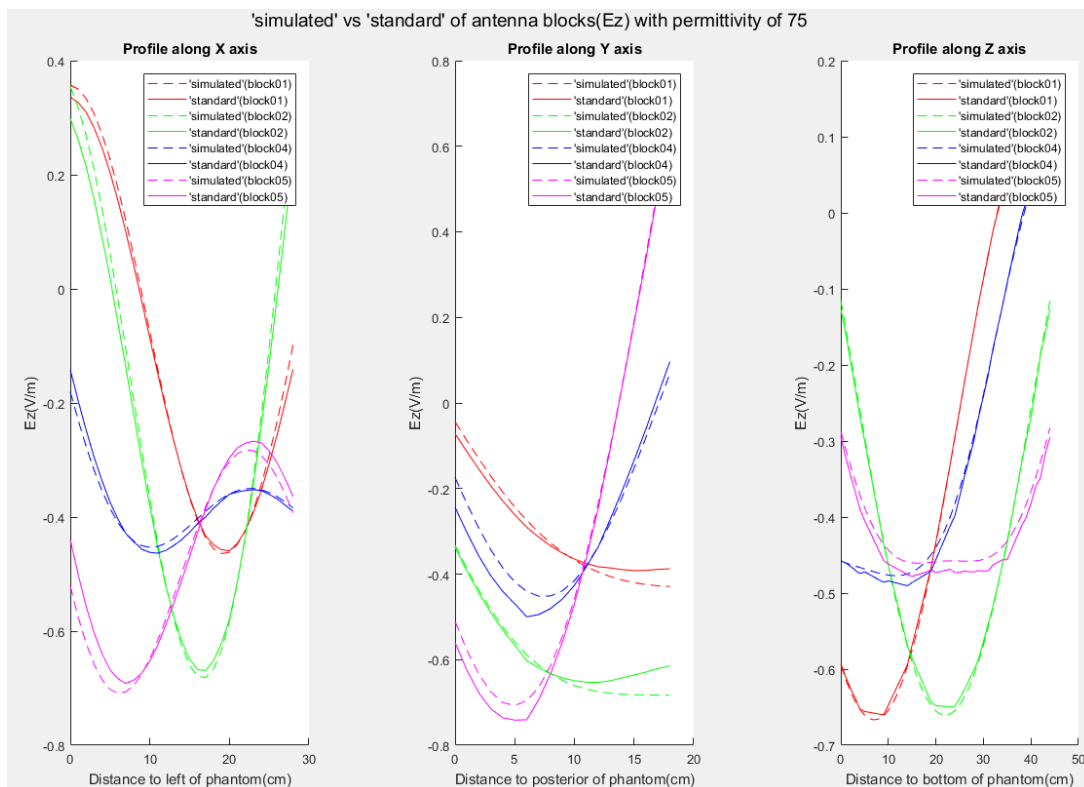


Fig-Appendix.28: Electric field E_z profiles of the four typical blocks under the 'real' relative permittivity of water bolus of 75 respectively from 'simulated' and 'standard' electric field based on the 'measured' permittivity of 78

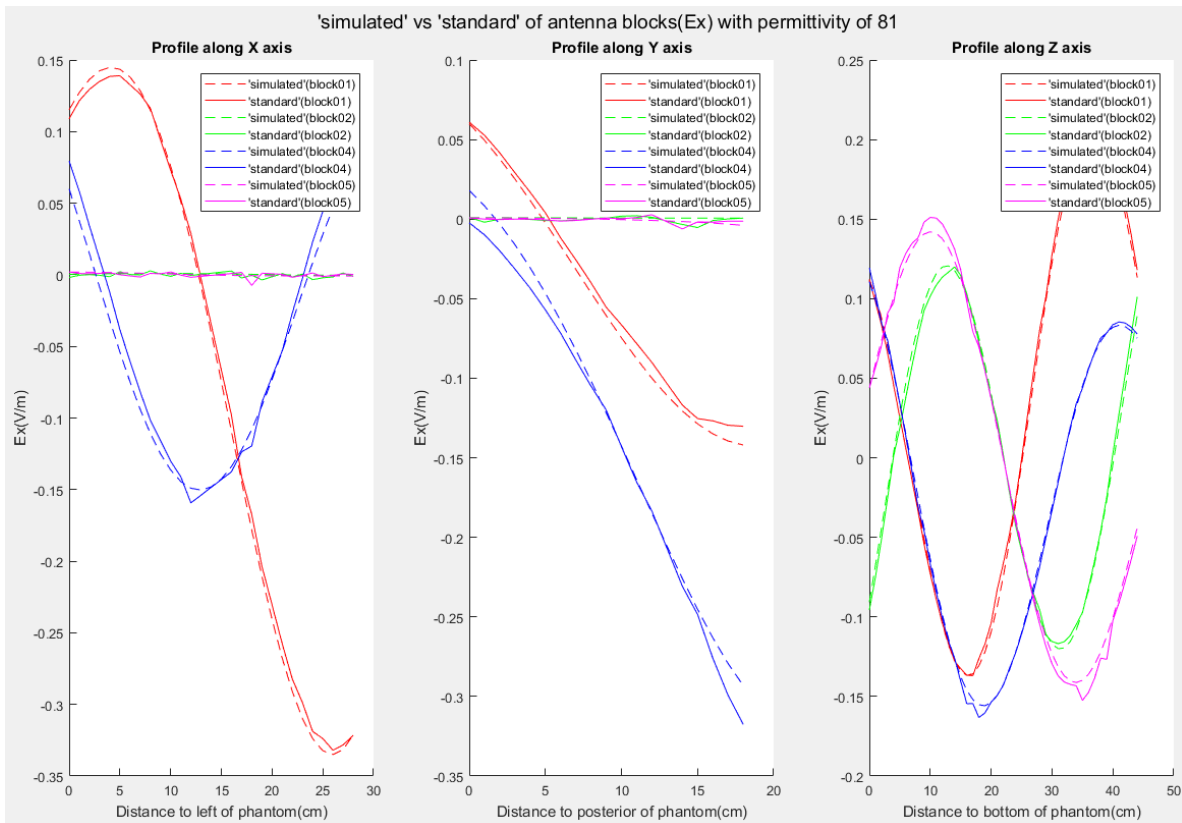


Fig-Appendix.29: Electric field E_x profiles of the four typical blocks under the 'real' relative permittivity of water bolus of 81 respectively from 'simulated' and 'standard' electric field based on the 'measured' permittivity of 78

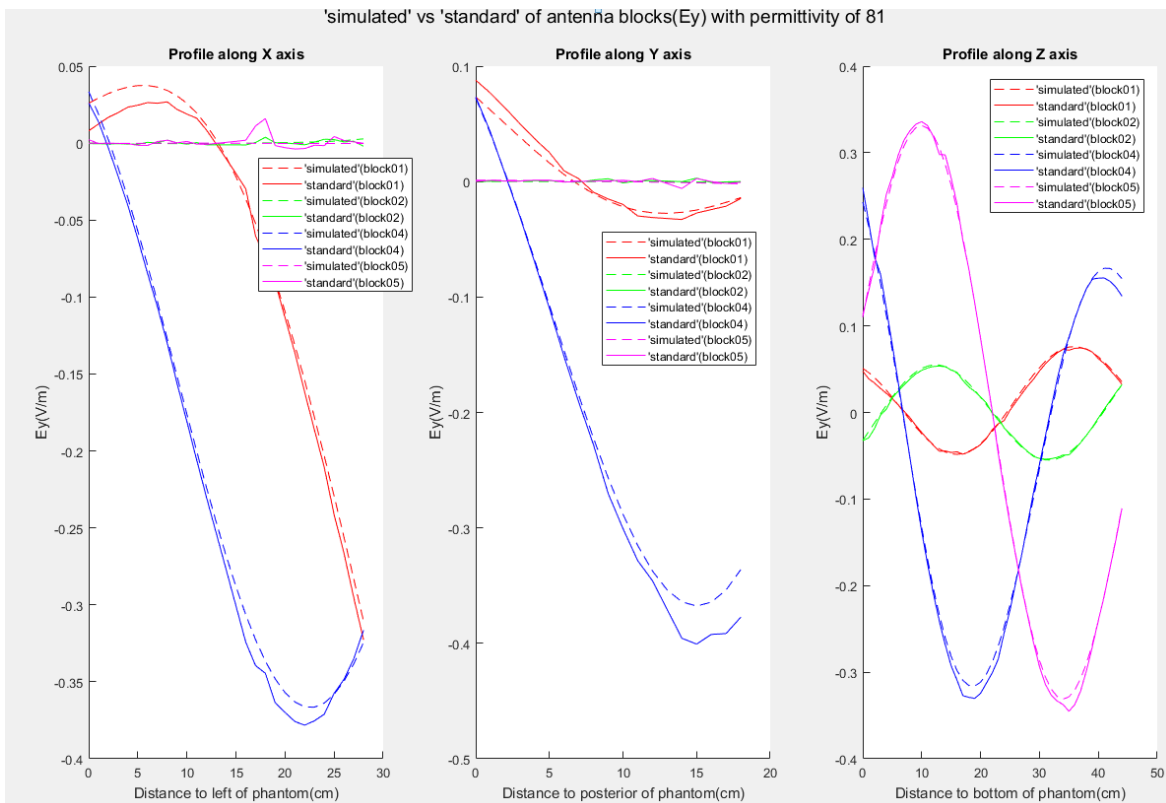


Fig-Appendix.30: Electric field E_y profiles of the four typical blocks under the 'real' relative permittivity of water bolus of 81 respectively from 'simulated' and 'standard' electric field based on the 'measured' permittivity of 78

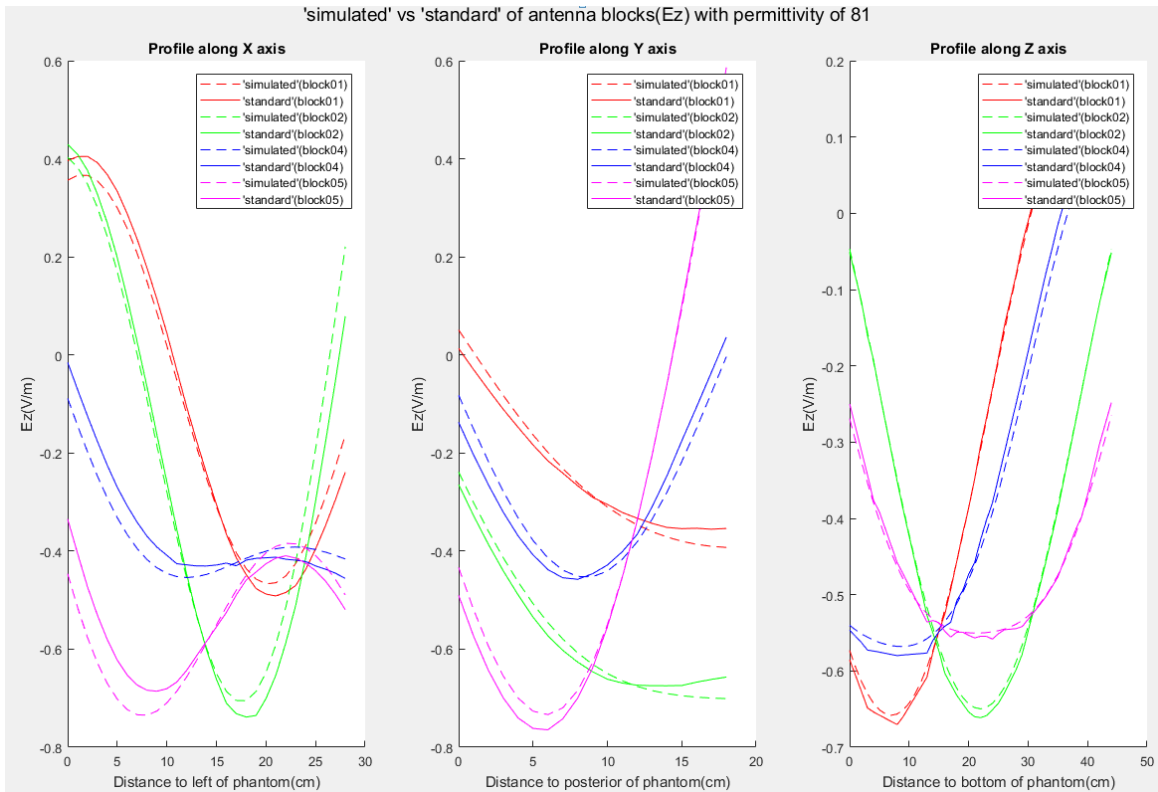


Fig-Appendix.31: Electric field E_z profiles of the four typical blocks under the 'real' relative permittivity of water bolus of 81 respectively from 'simulated' and 'standard' electric field based on the 'measured' permittivity of 78

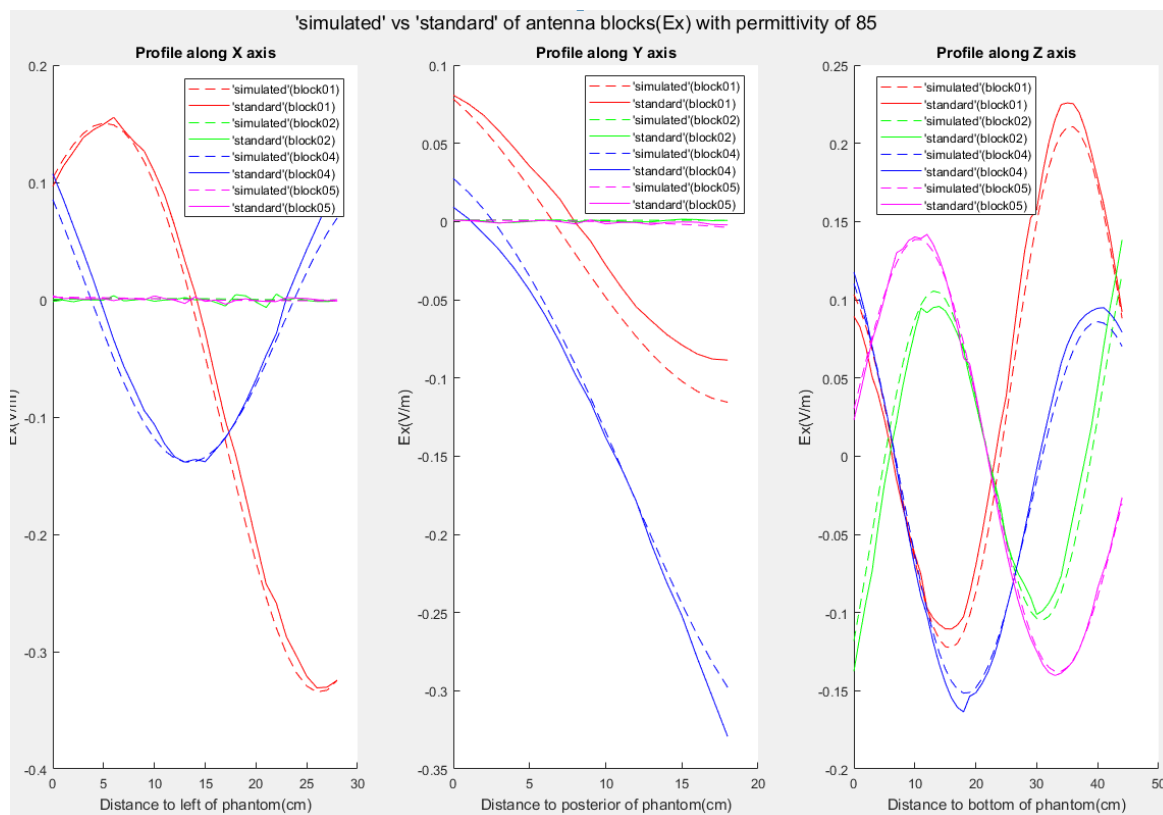


Fig-Appendix.32: Electric field E_x profiles of the four typical blocks under the 'real' relative permittivity of water bolus of 85 respectively from 'simulated' and 'standard' electric field based on the 'measured' permittivity of 78

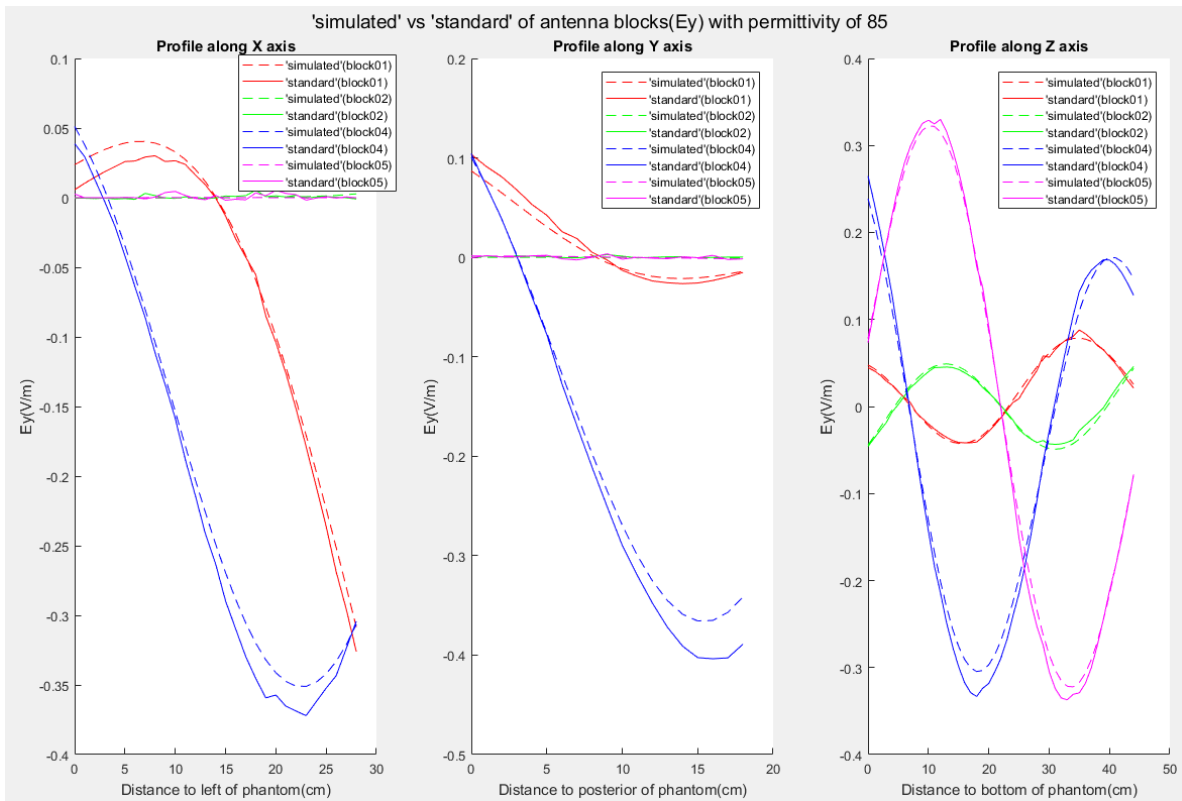


Fig-Appendix.33: Electric field E_y profiles of the four typical blocks under the 'real' relative permittivity of water bolus of 85 respectively from 'simulated' and 'standard' electric field based on the 'measured' permittivity of 78

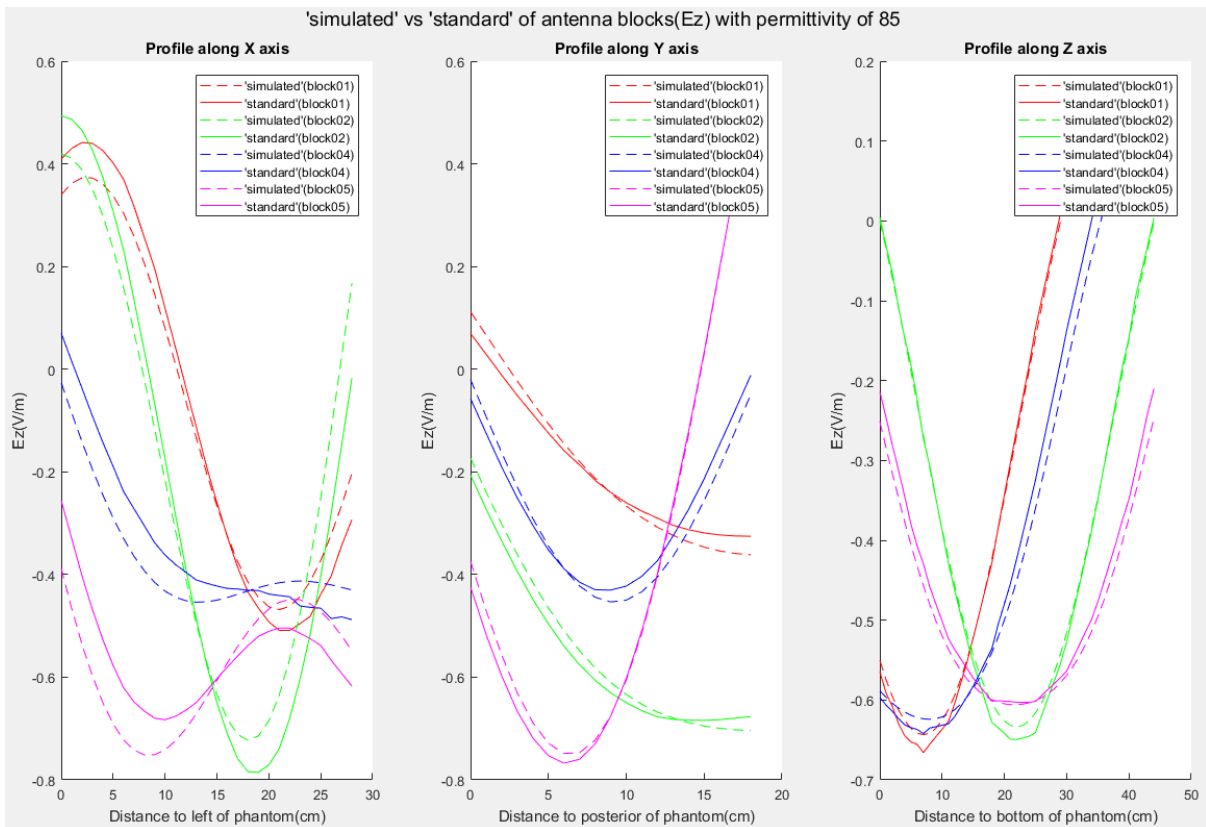


Fig-Appendix.34: Electric field E_z profiles of the four typical blocks under the 'real' relative permittivity of water bolus of 85 respectively from 'simulated' and 'standard' electric field based on the 'measured' permittivity of 78

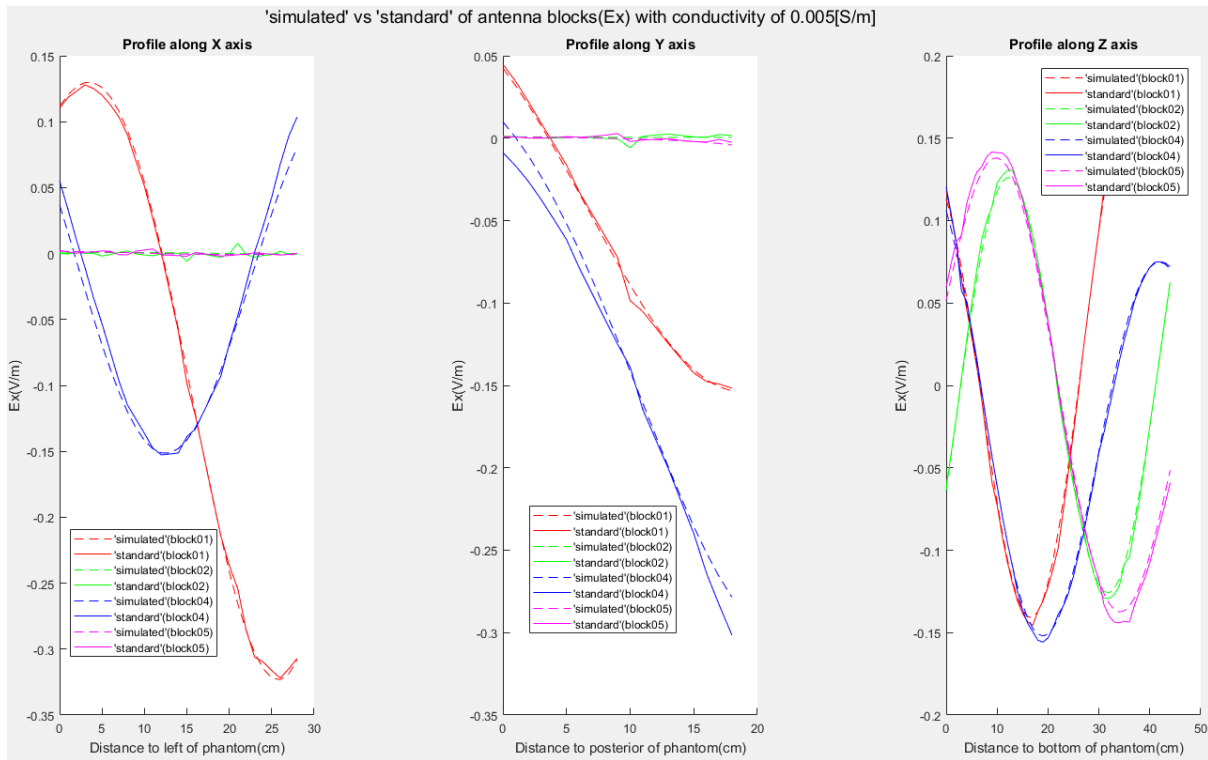


Fig-Appendix.35: Electric field E_x profiles of the four typical blocks under the 'real' conductivity of water bolus of 0.005 S/m respectively from 'simulated' and 'standard' electric field based on the 'measured' conductivity of 0 S/m

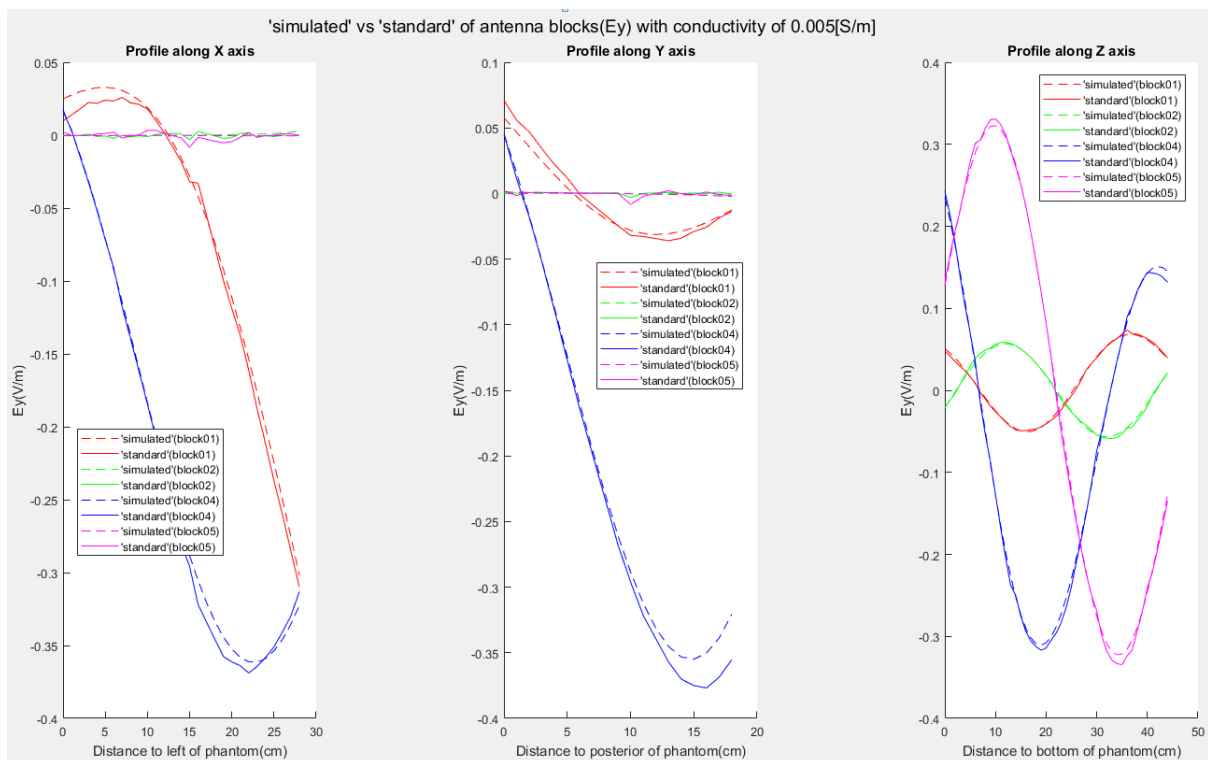


Fig-Appendix.36: Electric field E_y profiles of the four typical blocks under the 'real' conductivity of water bolus of 0.005 S/m respectively from 'simulated' and 'standard' electric field based on the 'measured' conductivity of 0 S/m

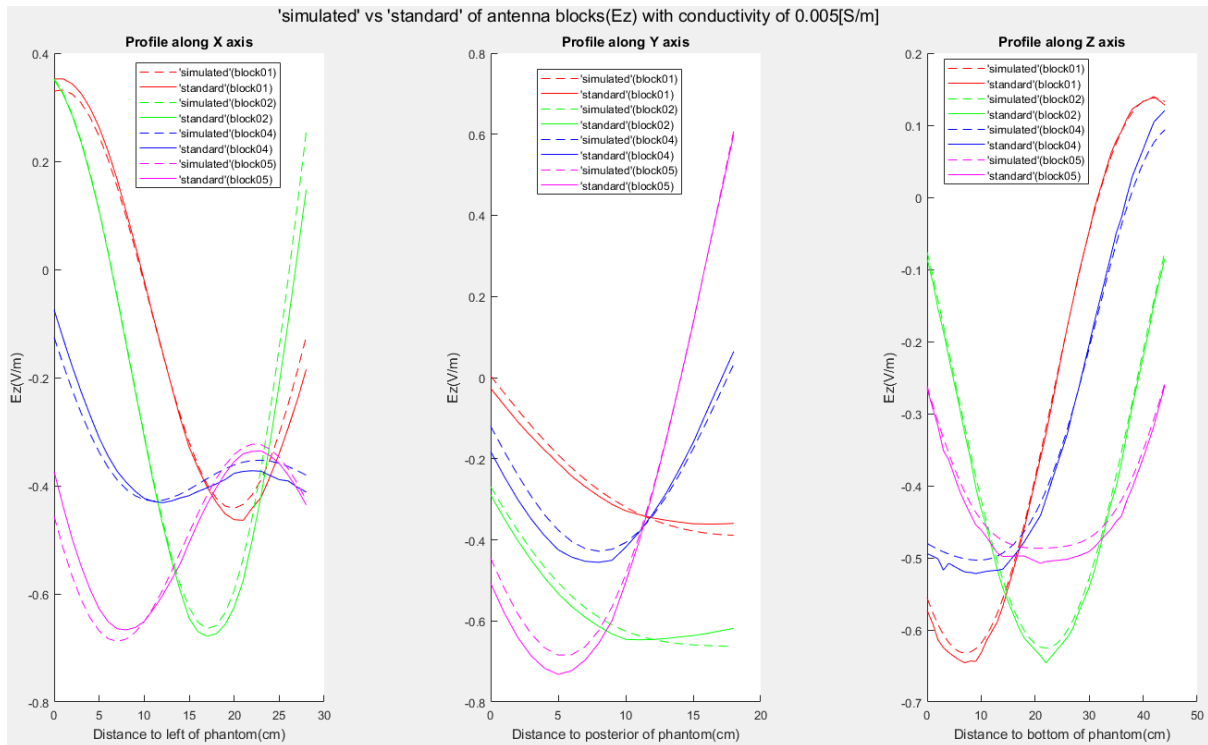


Fig-Appendix.37: Electric field E_z profiles of the four typical blocks under the 'real' conductivity of water bolus of 0.005 S/m respectively from 'simulated' and 'standard' electric field based on the 'measured' conductivity of 0 S/m

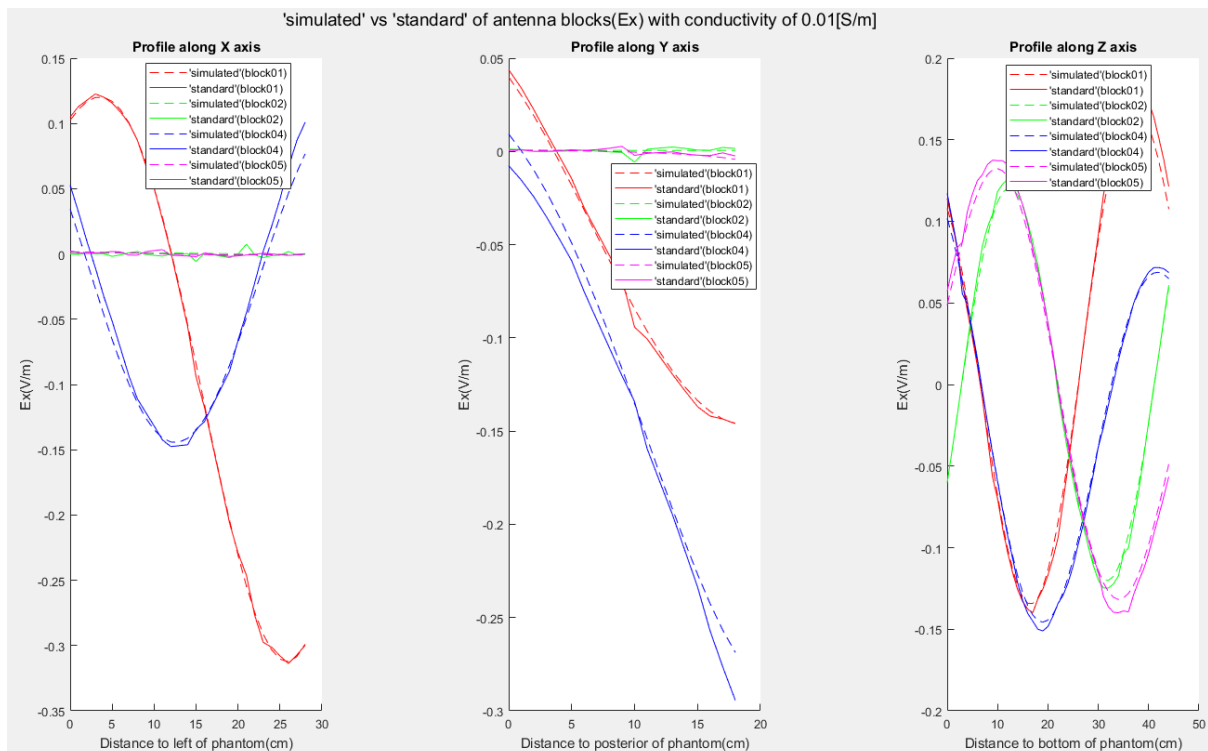


Fig-Appendix.38: Electric field E_x profiles of the four typical blocks under the 'real' conductivity of water bolus of 0.01 S/m respectively from 'simulated' and 'standard' electric field based on the 'measured' conductivity of 0 S/m

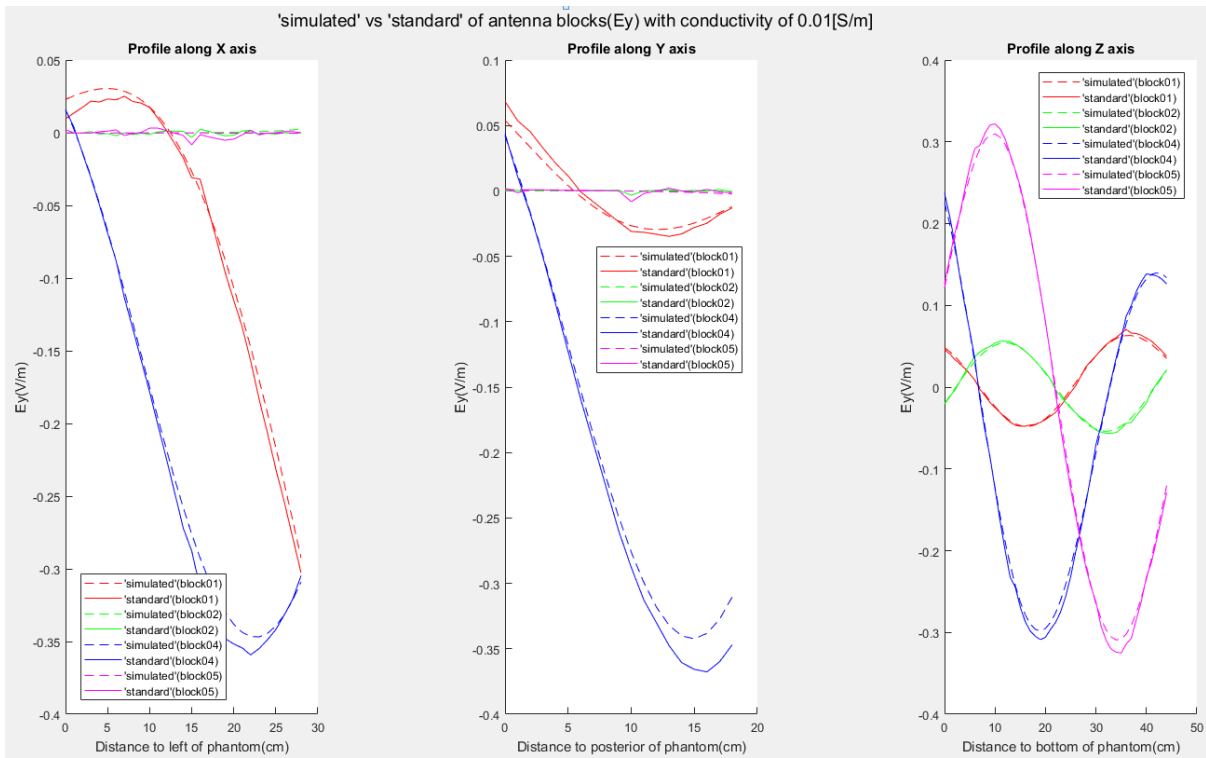


Fig-Appendix.39: Electric field E_y profiles of the four typical blocks under the 'real' conductivity of water bolus of 0.01 S/m respectively from 'simulated' and 'standard' electric field based on the 'measured' conductivity of 0 S/m

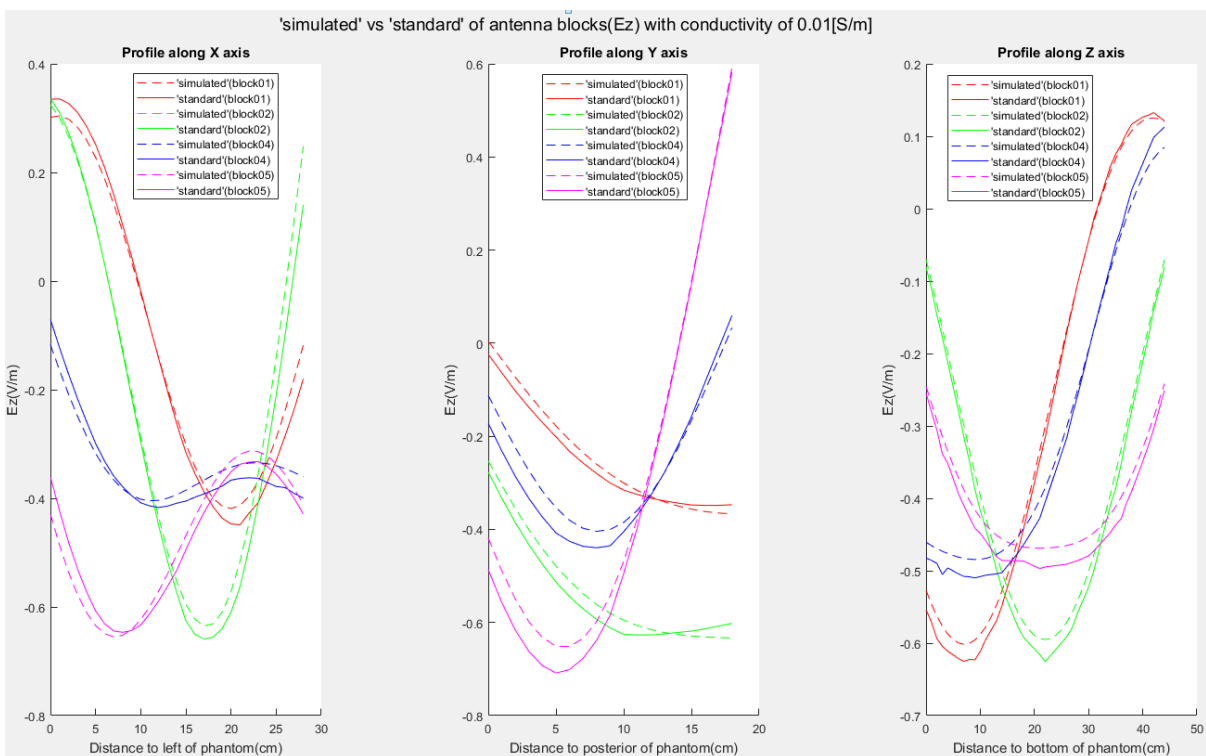


Fig-Appendix.40: Electric field E_z profiles of the four typical blocks under the 'real' conductivity of water bolus of 0.01 S/m respectively from 'simulated' and 'standard' electric field based on the 'measured' conductivity of 0 S/m

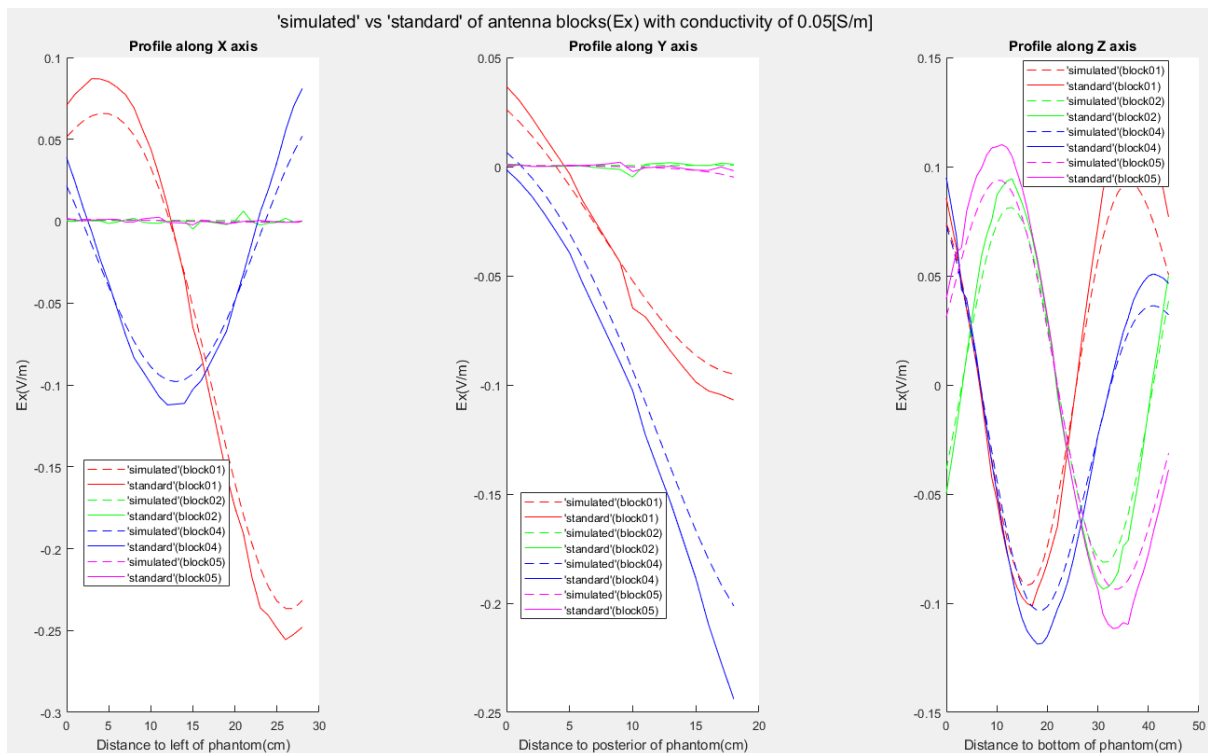


Fig-Appendix.41: Electric field E_x profiles of the four typical blocks under the 'real' conductivity of water bolus of 0.05 S/m respectively from 'simulated' and 'standard' electric field based on the 'measured' conductivity of 0 S/m

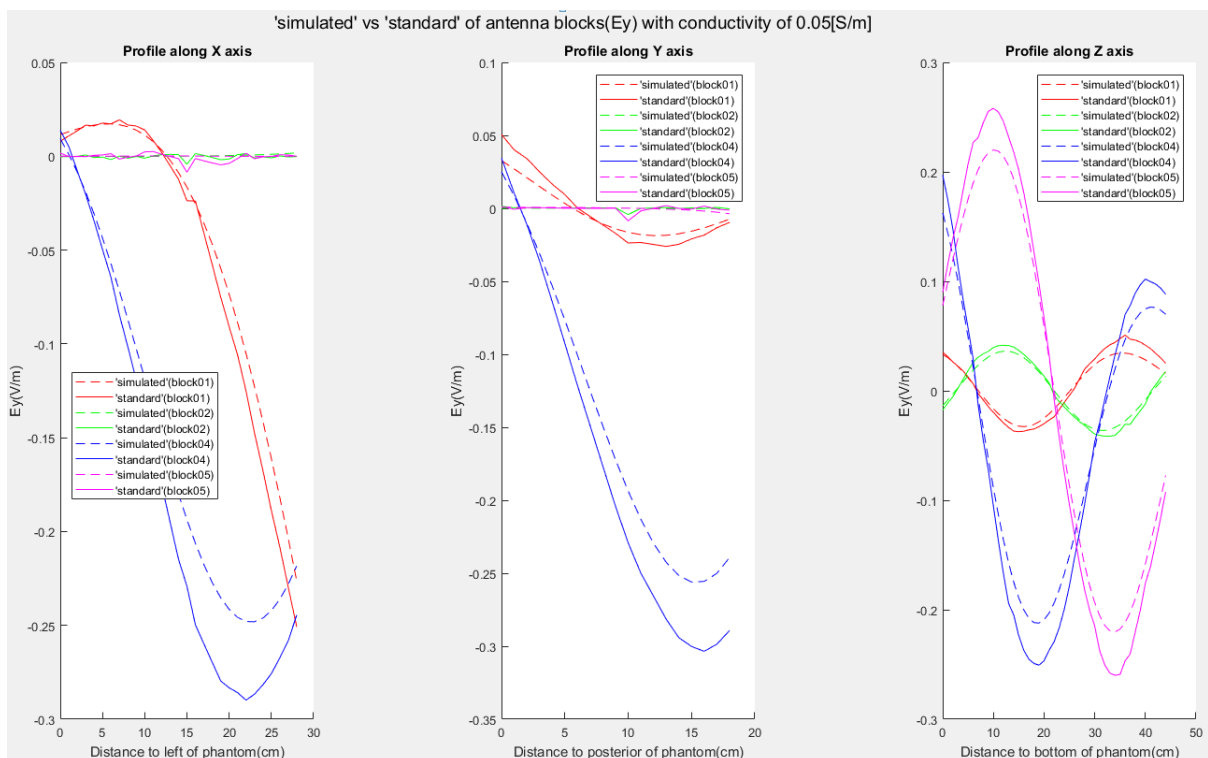


Fig-Appendix.42: Electric field E_y profiles of the four typical blocks under the 'real' conductivity of water bolus of 0.05 S/m respectively from 'simulated' and 'standard' electric field based on the 'measured' conductivity of 0 S/m

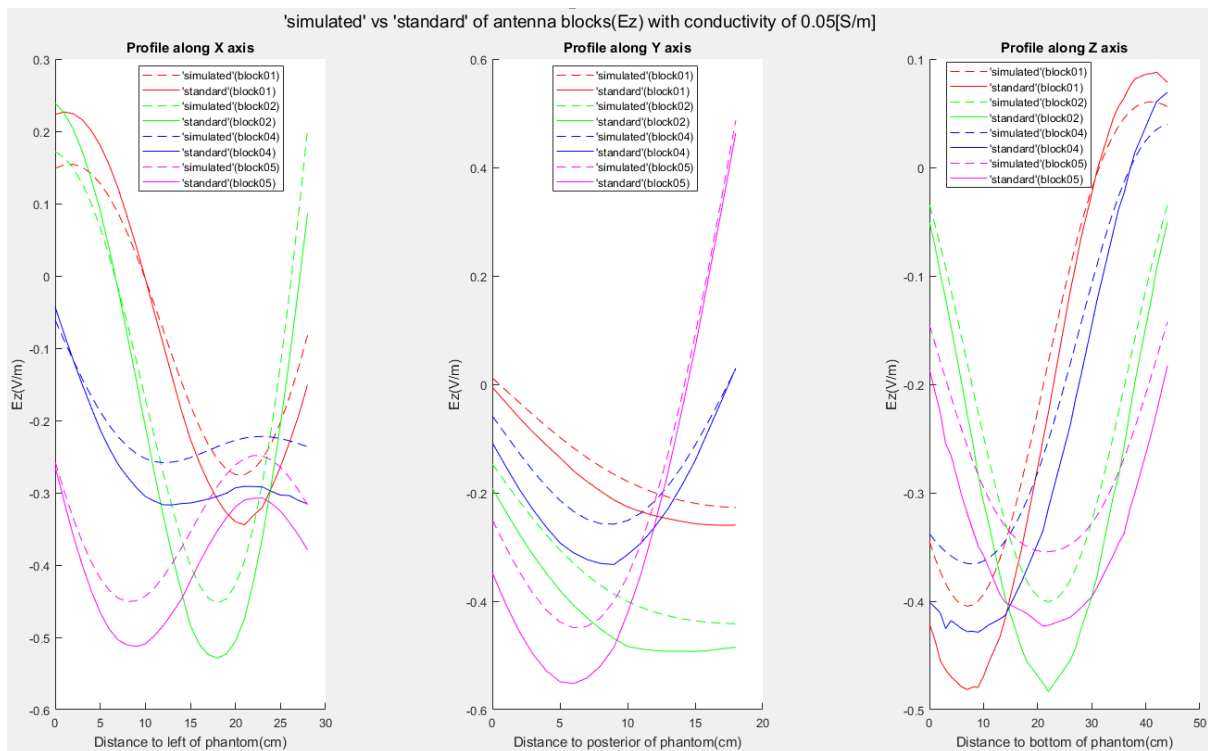


Fig-Appendix.43: Electric field E_z profiles of the four typical blocks under the 'real' conductivity of water bolus of 0.05 S/m respectively from 'simulated' and 'standard' electric field based on the 'measured' conductivity of 0 S/m

8 CV

PERSONALIEN

Name und Vorname: He, Wanji.....
Geburtsdatum: 06.02.1991.....
Geburtsort: Hubei,China.....
Familienstand: Single.....
Vater: He,Shaolong.....
Mutter: Liu,ZhengQiong.....

SCHULISCHER WERDEGANG

Sept.2005 – Juli.2008 Jingzhou High School, China

UNIVERSITÄRER WERDEGANG

Sept.2008 – Juli.2012 Bachelor of Biomedical Engineering
Huazhong University of Science and Technology
Sept.2012 – Aug.2013 Master of Biomedical Engineering
Shanghai Jiaotong University
Sep.2013 – Aug.2015 Master of Biomedical Engineering
Heidelberg University
May.2016 – present Doctoral student (Dr.sc.hum)
Medical Faculty Mannheim
Heidelberg University

9 ACKNOWLEDGEMENT

The author would like to give sincere thanks to the cooperation partners Prof. Christoph Bert and Bassim Aklan from Erlangen University and Sennewald Medizintechnik GmbH for providing technical support. In addition, sincere gratitude is given to Mr. Paul F. Turner from Pyrexar Medical, who provided E-field measurement data to support the comparisons in this work. This project was founded by German Central Innovation Program for SMEs (ZIM), project number: KF2769326TS4.